An investigation of surf-zone vorticity using phase-resolved numerical modeling and eddy tracking

Emma Shie Nuss

A dissertation
submitted in partial fulfillment of the
requirements for the degree of

Doctor of Philosophy

University of Washington

2024

Reading Committee:
Melissa Moulton, Chair
Sutara Suanda
Morteza Derakhti

Program Authorized to Offer Degree:
Civil and Environmental Engineering

University of Washington

Abstract

An investigation of surf-zone vorticity using phase-resolved numerical modeling and eddy tracking

Emma Shie Nuss

Chair of the Supervisory Committee:
Melissa Moulton
Civil and Environmental Engineering and Applied Physics Laboratory

In the surf zone, waves steepen and break, driving nearshore currents and impacting transport of nutrients, larvae, sediment, and other particulate matter. One type of nearshore current that is important to the cross-shore transport of surf-zone tracers is a transient rip current. Transient rip currents are strong offshore directed flows driven by short-crested wave breaking. Short-crested waves form in the surf zone when the wave field is directionally spread (i.e. wave energy is spread across many directions), forming an irregular sea surface that leads to wave breaking over finite regions of the wave field. As these short-crested waves break, they generate small-scale vertical vorticity (i.e. horizontal rotational motion). Energy from this small-scale vorticity can be transferred to larger-scale coherent rotational motions, or eddies, that interact and enhance cross-shore exchange of surf-zone tracers. Open questions remain about vorticity generation, evolution, and resulting cross-shore transport associated with surf-zone eddies. We use phase-resolved numerical simulations to quantify surf-zone vorticity evolution and exchange for varying wave conditions. Additionally, we couple this Eulerian perspective of surf-zone vorticity with a semi-Lagranian eddy-focused perspective by tracking individual eddies, similar to tracking of mesoscale ocean eddies. The combination of these two approaches provides a new perspective of how surf-zone vorticity evolves and implications for cross-shore

transport of surf-zone tracers.

Part 1 quantifies how wave field characteristics (i.e. crest length, number of crest ends) vary for a range of wave directional spreads and peak periods using a suite of phase-resolved numerical simulations. Additionally, we relate wave field characteristics to the generation of small-scale vorticity, low frequency rotational power associated with large-scale vorticity, and cross-shore exchange velocities. We find that while crest lengths decrease and the number of crest ends increases for increasing directional spread, small-scale vorticity generation and cross-shore exchange velocities exhibit a peak at intermediate directional spread. A weaker relationship is observed for peak period, with shorter crest lengths and a greater number of crest ends observed for decreasing peak period, while vorticity generation and exchange velocities are similar for intermediate and longer peak period, but decrease for shorter peak period.

Part 2 investigates how large-scale coherent vorticity, or eddies, vary across the surf zone and offshore for varying wave directional spreads through application of a modified mesoscale ocean eddy identification algorithm. This modified algorithm identified individual eddies in the surf zone and offshore for low, intermediate, and high directional spread simulations. Eddy characteristics, such as size, shape, and circulation strength were quantified for all identified eddies. We find that while eddy characteristics vary minimally between directional spreads in the surf zone, the total number of eddies in the surf zone increases with increasing directional spread. However, we also find that a greater number of eddies, with a higher median nonlinearity, are found offshore at intermediate directional spread, consistent with a peak in cross-shore exchange velocities at intermediate directional spread (finding from Part 1).

Part 3 applies a tracking algorithm to explore how large-scale eddies (identified in Part 2) vary over their life cycle. Individual eddies are tracked spatially recording their characteristics (i.e. size, circulation, etc.) and translation information (i.e. translation

speed, direction, etc.). Additionally, a clustering algorithm is applied to classify types of eddy trajectories observed throughout the model simulation. We find that eddy trajectories fall into three categories, eddy tracks that tend to: 1) start and stay within the surf zone, 2) start and stay offshore, and 3) start offshore and persist for a long duration. While these trajectory types exhibit distinct behavior, eddy characteristics exhibit similar responses to bathymetric changes within the surf zone and generally conserve potential vorticity. Findings also highlight several tracer transport pathways, including eddy pairs, nonlinear eddies, and offshore jet features, but suggest that further work is needed to understand when and why specific transport mechanisms may dominate.

TABLE OF CONTENTS

LIST OF FIGURES

LIST OF TABLES

ACKNOWLEDGMENTS

While the work in this dissertation is the culmination of many years of my own effort, this work would not be possible without immense support from mentors, colleagues, friends, family, and funding.

This research expands upon work that has come before me and laid the foundations for me to build upon. Specifically, the National Science Foundation (NSF) funded transient rip current laboratory experiment and modeling project has been instrumental to framing my research. Additionally, I would also like to thank Katherine Brodie, Margaret Palmsten, and the staff of the O.H. Hinsdale Wave Research Laboratory at Oregon State University for helping to run experimental trials and obtain, collect, and quality-control in situ measurements.

I cannot acknowledge the prior work and the NSF project without thanking Nirnimesh (Nirni) Kumar (1984 - 2020) for his many contributions. Nirni not only directly laid the foundation for my PhD research, but was also one of the biggest reasons for choosing to attend the University of Washington (UW) and join the UW Environmental Fluid Mechanics (EFM) group. His enthusiasm for science and passion for mentorship are missed by me and many others.

I am incredibly thankful for my advisor, Melissa Moulton. Melissa provides excellent science advice and feedback, while also continually being thoughtful, caring, and incredibly supportive. Melissa has a remarkable skill in providing constructive feedback to achieve high scientific rigor and progress, while also making the process fun, bolstering student confidence, and maintaining a positive work-life balance. Melissa's support, mentorship,

and confidence in my scientific ability has been instrumental to my own confidence and growth as an independent scientist. Melissa is a model of what I aspire to be as a scientist and mentor.

I would also like to thank Ata Suanda for stepping into an unofficial co-advisor and co-mentor role after Nirni's passing. Ata's enthusiasm and scientific insights always provide for fun and exciting discussion. Ata has a unique ability to bring joy and curiosity to scientific exploration. Ata's support and excitement for each step and new result throughout my PhD journey have aided my growth as a scientist and made the process enjoyable along the way.

In addition to two excellent mentors, I am grateful for Christine Baker, who has been a peer mentor and friend through this journey. From paper discussions, sharing code, and talking about our research, it has been such a joy to work alongside Christine and have her a few steps ahead to help guide my way.

My time at UW has been marked by immense support from the broader UW science community. Specifically, I would like to thank Morteza Derakhti, Nathan Kutz, and Michelle DiBenedetto for serving on my PhD committee. Morteza has always been excited and eager to hear about my research and his expertise and suggestions have strengthened my work. Despite shifting interests and a different science background, Nathan has continued to be engaged and supportive of my research and has provided helpful insights into data driven methods, as well as some excellent coffee. I would like to thank Michelle for serving as the Graduate School Representative for my committee and always being supportive of my growth as a scientist. Beyond my committee, I would like to thank the UW EFM community. This community has been incredibly supportive and the interest in my research and career development from many of the EFM faculty has been instrumental in my growth as a scientist and my future career success. In particular,

I'd like to thank Alex Horner-Devine for being a mentor throughout my PhD, providing both practical guidance on the PhD process and broader career advice. Additionally, I'd like to thank the EFM students, postdocs, and partners. You all have become my science family and I cannot imagine going through this PhD journey without you all.

Beyond UW, I would like to thank the many friends who have cheered me on despite little understanding of what my research is or what a PhD entails. In particular, I would like to thank my Coalescence Dance Company family. Dancing with you all has been so much fun over the past few years, but has helped keep me balanced and sane through the stress of completing my PhD.

Next, I would like to thank my family, Mom, Dad, Katie and Caille, for their continual support and encouragement. I would not be the curious life-long learner without my parents motivating me to always ask questions and be interested in the world around me. From early morning tide pooling with my dad and trips to the aquarium with my mom, it is not a coincidence that I've developed a love for studying the coastal ocean.

I cannot thank Seth Travis enough for his support through this PhD journey. Seth's unwavering confidence in my scientific abilities bolstered my own confidence in times of self doubt, his cooking nourished me when I didn't have time to feed myself, and his love comforted me and reminded me of what was actually important when I was too stressed to see beyond a minor bump in the road. There is no one else that I would rather go through life (and a PhD) with than Seth.

Lastly, the research in this dissertation has been funded by NSF, Office of Naval Research, the University of Washington Dean's Fellowship, and the Department of Civil and Environmental Engineering.

Chapter 1
INTRODUCTION

1.1 Motivation

The nearshore is the region of the ocean that extends from the coastline to the inner shelf, which is the transition from the surf zone to the deeper waters ($O(100\ \mathrm{m})$) of the mid-continental shelf (*Kumar et al.*, 2021). This region is subject to dynamic and multifaceted oceanic and environmental conditions. Wind and waves drive coastal currents, impacting the transport of nutrients and larvae, important to marine ecosystems, and also the movement of sediment, pollutants, and pathogens that can impact coastal infrastructure, nearshore water quality, and marine ecosystem health. As humans increasingly live in coastal urban environments and climate change intensifies coastal hazards *Intergovernmental Panel on Climate Change (IPCC)* (2022), understanding these nearshore processes is crucial to supporting marine ecosystem health as well as mitigating coastal hazards.

The inshore region of the nearshore, known as the surf zone, encompasses the waters from the shoreline to the seaward extent of depth-limited wave breaking. Waves propagating towards the coast transport energy from far away storms and this energy is dissipated through wave breaking in the surf zone. Wave breaking can drive surf-zone currents, which are crucial to the transport of tracers such as larvae, nutrients, sediment, pollutants, and pathogens both along the coast through longshore currents (*Longuet-Higgins*, 1970; *Feddersen et al.*, 1998) and away from the shore through bathymetric and transient rip currents (*Castelle et al.*, 2016). Proximity to the land introduces runoff, which can impact nearshore water quality through the introduction of sediment, pathogens, pollutants, and nutrients that can support harmful algal blooms. Cross-shore exchange, the transport of material from the surf zone to the inner shelf, is an important control on nearshore

water quality (*Halpern et al.*, 2008; *Boehm et al.*, 2017) and impacts larval transport and recruitment (*Morgan et al.*, 2017; *Moulton et al.*, 2023). Therefore, predicting cross-shore exchange is important for making management decisions that impact coastal ecosystems and water quality, such as beach and fisheries closures.

Rip currents, fast moving offshore directed flows, are a dominant driver of cross-shore exchange. There are several different types of rip currents that are driven by bathymetric, hydrodynamic, and boundary controls that set up alongshore variability in wave breaking (*Castelle et al.*, 2016). In a multi-directional wave field, waves constructively and destructively interfere, forming an irregular sea surface leading to wave breaking along finite crest lengths along the highest amplitude regions of the sea surface. As these waves break, they inject vertical vorticity (i.e. horizontal eddies) into the surf zone. These eddies are hypothesized to interact and lead to the development of intermittent offshore flows in random locations known as transient rip currents (*Peregrine*, 1998; *Clark et al.*, 2012; *Feddersen*, 2014). Cross-shore exchange driven by transient rip currents has been parameterized (*Suanda and Feddersen*, 2015), but the underlying mechanisms that drive the development of offshore flow from wave breaking induced eddy injection is still unknown.

The following sections in this chapter outline background and theoretical material relevant to the work in this dissertation, ending with a brief outline of the dissertation.

1.2 Surface gravity waves

1.2.1 Wave theory

A wave is a disturbance that propagates energy through space and can be mathematically described in one spatial dimension (x) as:

$$\eta(x,t) = a\cos(kx - \omega t) \tag{1.1}$$

where η is the free surface, a is the wave amplitude, k is the wavenumber, ω is the frequency, and x is distance in the direction of wave propagation. A wave propagates at

speed, c, where:

$$c = \frac{\omega}{k} = \frac{L}{T} \tag{1.2}$$

where L is the wavelength (equivalent to $2\pi/k$) and T is the wave period (equivalent to $2\pi/\omega$. In the ocean, waves observed at the surface of the ocean, the interface between ocean and atmosphere, are known as surface gravity waves. Waves in the ocean have a specific relationship between their wavelength (or wavenumber) and period (or frequency) and this relationship is known as the dispersion relationship:

$$\omega^2 = gk \tanh kh \tag{1.3}$$

where g is gravitational acceleration and h is the water depth. This relationship simplifies for deep water (very large kh, $kh > \pi/2$), and shallow water (very small kh, $kh < \pi/10$):

$$\begin{aligned} \text{deep water}: &\quad \omega^2 = gk \\ \text{shallow water}: &\quad \omega^2 = ghk^2 \end{aligned} \tag{1.4}$$

which results in the phase speed of deep water waves being proportional the wavelength, with longer waves traveling faster. For shallow water waves, phase speed is independent of wavelength and solely dependent on the water depth. This fundamental relationship between wavelength, period, and water depth influences a multitude of ocean wave dynamics. Importantly for coastal processes, in intermediate to shallow water depths, the wave propagation speed and wavelength change in differing water depths. The transformation of wave shape and behavior as waves propagate into shallower coastal waters is known as shoaling. Shoaling is crucial to how, why, and when waves break in the surf zone.

1.2.2 Wave shoaling and depth-limited wave breaking

Wave frequency is a fundamental characteristic of a wave and therefore does not change as a wave propagates across the ocean and encounters bathymetric changes. Additionally, wave energy flux, which is related to the wave height and propagation of a packet of

waves (group speed), is conserved until wave breaking. Conservation of wave energy flux and changes in wavelength and speed due to the dispersion relationship (Eq. 1.3) results in dramatic changes in waves as they propagate into shallow water, such that their wavelength decreases and wave crests steepen, this process is known as wave shoaling. Additionally, if waves propagate into shallow water at an angle they begin to turn towards shallower regions through a process called wave refraction, leading to wave propagation to become less oblique as waves propagate towards shore. As these waves turn towards shore due to wave refraction and steepen due to wave shoaling wave breaking can occur. According to *Miche* (1944), once the wave height exceeds a steepness criterion the wave will break. As a wave breaks it dissipates energy into the surf zone. Further background on wave breaking in the context of surf-zone eddy generation will be provided in Section 1.3.1.

1.2.3 Wave statistics

The wave theory presented above describes wave characteristics for a single wave; however, the ocean is made up of many waves with varying wave characteristics. This section will outline how various wave statistics are defined and computed for an irregular wave field.

Peak period

In an irregular wave field, wave energy is distributed over a range of wave frequencies and are therefore characterized in spectral space. A time record of sea surface elevation or bottom pressure measurements allows for describing the energy in the wave record as a function of frequency, i.e. $S(f)$. The peak period, T_p, of a wave record is defined as the wave period $(1/f)$ associated with the largest energy.

Significant wave height

In addition to T_p, we can also characterize the significant wave height, H_s, associated with an irregular wave field using the energy-frequency spectrum, $S(f)$. The significant wave height is defined as the average wave height of the highest third of the waves and can be estimated by:

$$H_s = 4\sqrt{\int S(f)\, df} \tag{1.5}$$

Directional spread

In addition to characterizing the wave field as a function of frequency, a directional spectrum ($S(f,\theta)$), which characterizes wave energy vs. direction, is used to determine the directionality of the waves. The directional spectrum, $S(f,\theta)$, is made up of:

$$S(f,\theta) = S(f)D(\theta,f) \tag{1.6}$$

where $S(f)$ is the wave energy spectrum as a function of frequency (f) and $D(\theta,f)$ is the wave directional spectrum as a function of f and direction (θ). A common form of $D(\theta,f)$ is (*Mitsuyasu, Hisashi et al.*, 1975):

$$D(\theta,f) = \frac{1}{\pi}2^{2s-1}\frac{\Gamma^2(s+1)}{\Gamma(2s+1)}\cos^{2s}\left(\frac{\theta-\theta_0}{2}\right) \tag{1.7}$$

where θ_0 is the mean wave direction and s is a parameter that provides a quantification for a model of the wave directional spectrum. The directional spread (σ_θ) of a wave field can be estimated from s by:

$$\sigma_\theta = \left(\frac{2}{1+s}\right)^{1/2} \tag{1.8}$$

From co-located measurements of pressure and velocity, a buoy, or an array of pressure sensors, σ_θ can be estimated from the directional moments (*Kuik et al.*, 1988).

1.3 Surf-zone currents and eddy processes

1.3.1 Short-crested wave breaking and eddy evolution

Wave-group forcing (*Haller et al.*, 1999; *Long and Özkan Haller*, 2009), shear instabilities in alongshore currents (*Bowen and Holman*, 1989; *Oltman-Shay et al.*, 1989), and short-crested wave breaking (*Peregrine*, 1998; *Johnson and Pattiaratchi*, 2006; *Clark et al.*, 2012) are all hypothesized to generate low frequency (frequency, $f < 0.04$ Hz) currents and horizontal rotational motions (i.e. eddies) in the surf zone. In wave-resolved numerical studies, short-crested wave breaking has been found to be the dominant driver in surf-zone eddy variability (*Feddersen*, 2014). Short-crested wave breaking can occur during directionally spread wave conditions on alongshore uniform beaches.

As these multi-directional waves shoal and refract, their mean wavelength, direction, and amplitude change (*Longuet-Higgins*, 1956). As depth limited wave breaking occurs, breaking occurs along a finite region, introducing alongshore variability in wave breaking and injection of vorticity at wave crest ends. The length and number of crest ends in the surf zone may be important to the magnitude of vorticity injection and the resulting transient rip current driven cross-shore exchange. The expected crest lengths (l_{crest}) observed when two monochromatic wave trains intersect can be shown using linear wave theory to be:

$$l_{crest} = \frac{L}{4 \sin \theta} \tag{1.9}$$

where L is the cross-shore wavelength of the wave and θ is the wave angle (*Dalrymple and Lanan*, 1976; *Dalrymple*, 1989; *Postacchini et al.*, 2014; *Wei et al.*, 2017; *Choi and Roh*, 2021). This expected crest length in a simplified wave field is similar to *Longuet-Higgins* (1956)'s derivation of expected mean crest lengths in an irregular wave field:

$$\overline{l_{crest}} = \frac{1}{2} \frac{\overline{L}}{\gamma} \tag{1.10}$$

where $\overline{L}$ is the mean cross-shore wavelength and γ is the root mean squared angular deviation of the waves from their mean direction, which is equivalent to the directional

spread of the wave field for linear wave theory. The factor of $1/2$ relates the alongshore wavelength to crest length, i.e. excluding the wave trough. Thus, along-crest length scales of breaking waves are expected to decrease as directional spread increases. While larger directional spread is associated with greater vorticity variance and surf-zone dispersion (*Spydell and Feddersen*, 2009; *Clark et al.*, 2010; *Feddersen*, 2014; *Spydell et al.*, 2009; *Spydell*, 2016; *Wei et al.*, 2017; *Dooley et al.*, 2024), the relationship between directional spread, breaker crest lengths, and vorticity injection is still unknown.

Numerical modeling (*Bühler and Jacobson*, 2001; *Johnson and Pattiaratchi*, 2006; *Bruneau et al.*, 2011) and observational studies (*Clark et al.*, 2012) suggest that vertical vorticity is generated via short-crested wave breaking due to the alongshore variation in wave breaking force. On alongshore uniform beaches with normally incident waves, the time-rate of vorticity generation is:

$$\frac{\partial \omega}{\partial t} \approx \nabla \times \mathbf{F_{br}} \tag{1.11}$$

where ω is vertical vorticity, t is time, and $\mathbf{F_{br}}$ is the wave breaking force (*Peregrine*, 1998; *Bühler and Jacobson*, 2001; *Bonneton et al.*, 2010). As a short-crested wave breaks, positive and negative vorticity is generated on the the left and right ends of the wave respectively. The vorticity injection creates high frequency (f = 0.1 Hz) and small scale eddies ($\mathcal{O}$(10 m)) (*Peregrine*, 1998; *Bühler and Jacobson*, 2001; *Bonneton et al.*, 2010).

Once waves break and vorticity is injected into the surf zone, these small scale eddies are hypothesized to interact and develop into larger scale horizontal rotational motions. These large scale eddies can interact leading to the formation of coherent vortex pairs, which can intensify and develop offshore flow as they propagate towards deeper water (*Johnson and Pattiaratchi*, 2006). The dynamics that form these large scale eddies are thought to be similar to a forced two-dimensional turbulence system (*Peregrine*, 1998; *Spydell and Feddersen*, 2009; *Feddersen*, 2014; *Elgar and Raubenheimer*, 2020; *Marchesiello et al.*, 2021; *Elgar et al.*, 2019). For a two-dimensional incompressible flow field, the vertical

vorticity evolution is described by *Salmon* (1998); *Boffetta and Ecke* (2011):

$$\frac{\partial \omega}{\partial t} + \mathbf{u} \cdot \nabla \omega = \nu \nabla^2 \omega - \alpha \omega + f \tag{1.12}$$

where $\frac{\partial \omega}{\partial t}$ is the time evolution of vorticity (ω), $\mathbf{u} \cdot \nabla \omega$ is the vorticity flux divergence, $\nu \nabla^2 \omega$ is the viscosity term, $\alpha \omega$ is a linear frictional term, and f is the forcing or source term. For short-crested wave breaking driven eddy generation, this forcing term is hypothesized to be the curl of the wave breaking force ($f = \nabla \times \mathbf{F_{br}}$). While 2D turbulence is a useful framework for these dynamics, further work is needed to fully understand the eddy forcing, the evolution of larger scale rotational motions, and the development of transient rip currents to determine if the dynamics are consistent with theory.

1.3.2 Eddy driven cross-shore exchange

Transient rip currents can drive cross-shore exchange of sediment, pollutants, larvae, and other particulate material up to two to four surf-zone widths from the shoreline in observations (*MacMahan et al.*, 2010a; *Hally-Rosendahl et al.*, 2014) and models (*Reniers et al.*, 2009; *Suanda and Feddersen*, 2015; *Kumar and Feddersen*, 2017a). Cross-shore exchange can be estimated as the cross-shore component of the alongshore-averaged and depth-averaged offshore directed Lagrangian velocity:

$$U_{ex}(x) = \frac{1}{L_y} \left\langle \int_0^{L_y} u_L^-(x, y, t) \, \mathrm{dy} \right\rangle \tag{1.13}$$

where $u_L^-(x, y, t)$ is just the offshore directed component of the Lagrangian velocity, L_y is the alongshore length over which cross-shore exchange is being calculated, and $\langle \cdot \rangle$ indicate wave averaging (*Suanda and Feddersen*, 2015; *Grimes et al.*, 2019, 2020). This estimate of cross-shore exchange captures the total magnitude of cross-shore exchange. To quantify the transient rip current driven cross-shore exchange, we first decompose the velocity field into rotational and irrotational components (*Spydell and Feddersen*, 2009):

$$\mathbf{u} = \nabla \phi + \nabla \times \psi \tag{1.14}$$

where the irrotational velocity ($\nabla\phi$) is the divergent component of the flow, associated with wave propagation and mean flow, and the rotational velocity ($\nabla \times \psi$) is the part of the flow associated with eddies and transient rip currents. Substituting the rotational component of the cross-shore velocity into Eq. 1.13 for the Lagrangian velocity provides an estimate of cross-shore exchange resulting from rotational flows such as transient rip currents, because the velocity decomposition removes the contributions to cross-shore exchange from irrotational flows, such as the alongshore uniform component of Stokes drift and undertow (*Suanda and Feddersen*, 2015). Cross-shore exchange specific to transient rip currents can be estimated with Eq. 1.13 using the offshore directed component of the time varying component of the velocity field ($u_L^- = u - \bar{u}$) allowing persistent rip current structures to be removed (*O'Dea et al.*, 2021). Additionally, a scaling for the maximum transient rip current driven cross-shore exchange was developed based on idealized modeling studies on a planar beach (*Suanda and Feddersen*, 2015):

$$\frac{U_{ex}^r}{\sqrt{gh_b}} = 0.029\sigma_{\theta b}(1 + 70S_b) \tag{1.15}$$

where h_b is the water depth, $\sigma_{\theta b}$ is the directional spread, and S_b is the wave steepness at the breakpoint, b.

Cross-shore exchange and surf-zone dispersion have been explored through modeling and observational dye studies. Model simulations have been shown to agree well with observational dye studies (*Clark et al.*, 2011; *Hally-Rosendahl and Feddersen*, 2016), suggesting that findings from model studies investigating transient rip current exchange can be applied to field settings. Modeling studies have explored how cross-shore exchange changes with varying wave conditions, its magnitude compared to other exchange processes, as well as the cross-shore extent of transient rip currents influence and their impact on inner shelf dynamics.

In numerical modeling studies, cross-shore exchange has been found to increase with increasing directional spread *Suanda and Feddersen* (2015); *Spydell and Feddersen* (2009); *O'Dea et al.* (2021) and be stronger than wave-induced Stokes-drift-driven exchange

extending to the inner shelf *Suanda and Feddersen* (2015). Additional work has investigated the influence of transient rip current exchange on inner shelf dynamics. In one-way coupled wave-resolved-circulation model simulations, *Kumar and Feddersen* (2017a) found that with an unstratified inner shelf, transient rip currents can transport properties up to 4 surf-zone widths from the shoreline, which can modify mean currents, vertical eddy viscosity, and cross-shore momentum balances. With stratification present on the inner shelf, transient rip currents contribute to irreversible mixing and increase the background potential energy (*Kumar and Feddersen*, 2017b). Additionally, transient rip current influence on the inner shelf has been shown to be more important that thermally driven exchange (*Grimes et al.*, 2020) and minimally impacted by offshore bathymetry (*O'Dea et al.*, 2021).

While it has clearly been shown that transient rip currents are an important mechanism for exchange of materials from the surf zone and influence larger scale dynamics on the inner shelf, there are still gaps in knowledge linking the vorticity injection to these larger scale impacts. The magnitude of cross-shore exchange has been linked to wave conditions, such as directional spread, but a full understanding of how eddy injection in the surf zone leads to influences offshore is still not known.

1.4 Phase-resolved numerical models

Transient rip currents are ephemeral and do not rely on bathymetric features to form, therefore, field measurements are difficult to obtain and study these processes. In laboratory studies, instruments and wave conditions can be set to provide a controlled environment to study the formation of transient rip currents. Despite this control, these studies can be limited by the closed geometry of laboratory basins, as well as the resolution and coverage of data needed to explore transient rip current dynamics. Numerical simulations can be used to complement laboratory studies, providing further control and high resolution information. Phase-resolved numerical models simulate individual wave generation, propagation, and breaking in high temporal and spatial resolution, which is necessary to explore transient rip current dynamics (*Feddersen et al.*, 2011; *Suanda and*

Feddersen, 2015; *Shi et al.*, 2012). These models provide a tool to understand surf-zone eddy dynamics and transient rip current formation through the ability to link wave field characteristics, eddy injection, and transient rip current activity.

Transient rip current dynamics and other surf zone processes have been extensively studied with numerical simulations (*Johnson and Pattiaratchi*, 2006; *Feddersen et al.*, 2011; *Suanda and Feddersen*, 2015; *Spydell*, 2016; *Grimes et al.*, 2020; *O'Dea et al.*, 2021). These studies utilize phase-resolving numerical models that are able to simulate individual wave generation, propagation, and wave breaking (*Shi et al.*, 2012; *Feddersen et al.*, 2011; *Kirby*, 2016). Many of these studies use Boussinesq type models, which are models that allow for weak dispersion in the nonlinear shallow water equations by retaining higher order terms. Shallow water wave theory simplifies the dispersion relationship to $\omega^2 = gk^2h$, by neglecting higher order terms in a Taylor series expansion of the full dispersion relation about $kh = 0$; whereas the Boussinesq equations retain a higher order term to include weak dispersion with a relationship (*Kirby*, 2016):

$$\omega^2 = gk^2h\left(1 - \frac{1}{3}(kh)^2\right). \tag{1.16}$$

The inclusion of higher order terms allows for more accurate representation of shallow water wave dynamics, improving on first order approximations in the shallow water wave limit. Optimization of the Boussinesq equations to minimize error of phase speed restricts the accuracy of this model to waves in which $kh \leq 3$ (*Nwogu*, 1997).

In addition to higher order accuracy of wave propagation, wave-resolved numerical models require accurate generation of waves through numerical wavemakers. In Boussinesq type models, waves are generated by adding mass along a thin source region (wavemaker) using a source function (*Wei et al.*, 1999). Numerical wavemakers can generate irregular wave fields according to common wave spectra, such as Jonswap, TMA, etc., or through 2D frequency-directional spectrum, which allows for the simulation of realistic complex wave fields.

When waves shoal in shallow water and steepen, a numerical representation of wave

breaking is used to parameterize dissipation of wave energy. The wave breaking force, F_{br}, has been used to parameterize wave breaking in wave-resolved numerical models as a Newtonian damping (*Kennedy et al.*, 2000):

$$\mathbf{F_{br}} = (h+\eta)^{-1}\nabla \cdot [\nu_{br}(h+\eta)\nabla \mathbf{u}] \tag{1.17}$$

where h is the water depth, η is sea surface elevation, u is the velocity vector, and ν_{br} is a parameterization of the breaking wave induced eddy viscosity (*Lynett*, 2006). This parameterization simulates wave breaking by damping the momentum through the introduction of viscosity as a wave steepens above its breaking threshold. This type of wave breaking paramterization is used in Boussinesq type models including FUNWAVE-TVD and funwaveC (*Shi et al.*, 2012; *Feddersen et al.*, 2011). The ability to simulate complex sea surface elevation patterns through time and the inclusion of parameterized wave breaking means that highly spatially and temporally resolved wave propagation and breaking can be simulated in the surf zone.

Boussinesq type models have been used extensively in shallow water wave applications, in particular for studies on transient rip current dynamics and cross-shore exchange (*Johnson and Pattiaratchi*, 2006; *Suanda and Feddersen*, 2015; *Feddersen et al.*, 2011; *Grimes et al.*, 2020; *O'Dea et al.*, 2021). These models are limited to nearshore application, such as surf zone processes, as model equations have increased error in phase speed when waves are either very small or when the water depth is too deep (i.e. $kh > 3$) (*Nwogu*, 1997). This restricts numerical simulations to shallow or intermediate water depths near the coast, excluding deeper offshore features. Additionally, wave-resolved numerical simulations require a small grid resolution and time-step to allow for proper numerical stability and minimization of error.

Due to these restrictions, model applications where science or management is focused on regional scale questions, wave-averaged and coupled wave-averaged-circulation models are generally used. Wave-averaged models, like SWAN, are spectral models that simulate the wavefield in frequency, direction and wavenumber space (*Ris et al.*, 1995).

While spectral models are relatively fast to run, these models only provide bulk wave information, such as significant wave height, peak period, mean direction, etc. These spectral models can be coupled with regional circulation models, like ROMS, to allow for inclusion of waves into circulation estimates. These models are used frequently for investigating regional scale oceanographic dynamics, such as coastal circulation patterns, upwelling, internal tides, etc. as well as exploring bio-physical and tracer dynamics, such as water quality, larval transport, and ecosystem dynamics.

Both wave-resolved and phase-averaged models provide tools to study coastal processes; however, phase-averaged models do not have the capability to simulate transient rip current generation via short-crested wave breaking. To explore short-crested wave breaking driven cross-shore exchange and its interaction with the inner shelf, *Kumar and Feddersen* (2017a,b) developed a coupled modeling approach between funwaveC and COAWST. This coupling took the wave breaking force (Eq. 1.17) from a previously run setup of funwaveC and computed the rotational wave forcing:

$$\mathbf{F_{br}^{(rot)}} = \nabla \times \psi_F(x, y, t)\hat{\mathbf{k}} \tag{1.18}$$

where ψ_F is the streamfunction, where $\nabla \times \mathbf{F_{br}} = \nabla^2 \psi_F$. Eq. 1.18 was input to COAWST as a depth-uniform body force every second in the simulation (*Kumar and Feddersen*, 2017a,b). This coupling successfully allowed for one-way coupling of wave-resolved short-crested wave breaking to impact the surf zone circulation and dispersion. The inclusion of short-crested wave breaking increased cross-shore transport, suggesting that transient rip currents are important for simulation and prediction of surf zone tracer dispersion. While this coupling was successful, the computational expense for running funwaveC to provide wave-breaking force output was high. Further work to understand how short-crested wave breaking generated vorticity and resulting cross-shore exchange related to wave conditions will allow for work to parameterizing these processes for a variety of coastal modeling applications.

1.5 Outline

This dissertation describes the results of investigations of surf-zone vorticity generation, eddy evolution and transport, and the development of cross-shore flows associated with transient rip currents using a phase-resolved numerical model. In particular we explore these surf-zone vorticity dynamics by taking an individual wave and eddy focused perspective. To explore surf-zone vorticity dynamics from this perspective, we characterize individual wave breaking and vorticity generation, identify individual surf-zone eddies, and follow these eddies over their life cycles. Each chapter of this dissertation describes the background, methods, and analysis used to tackle specific science questions about the nature of surf-zone vorticity generation and evolution.

Chapter 2 focuses on the question: *How do wave conditions influence breaking waves, generation of vorticity, and development of cross-shore exchange?* In Chapter 2, we describe the setup of a set of phase-resolved numerical simulations of directionally spread waves on an alongshore uniform laboratory-scale barred beach. This chapter presents a comparison of the numerical simulations with complementary laboratory experiments and an investigation of vorticity generation, evolution, and cross-shore exchange under varying directional spread and peak periods.

Chapter 3 focuses on the question: *How do coherent eddies vary in the cross-shore and for varying wave conditions?*. In Chapter 3, we describe the application of a modified mesoscale eddy identification algorithm applied to the surf zone to characterize surf-zone eddies in three numerical simulations. This chapter presents the eddy characteristics across the surf zone and inner shelf under varying directional spread.

Chapter 4 focuses on the question: *How do coherent eddies vary over their life cycle?* In Chapter 4, we describe application of an eddy tracking algorithm in the surf zone to identified surf-zone eddies in intermediate directional spread conditions to track eddy translation and transformation over its lifetime. Additionally, eddy trajectories are classified into trajectory types using a clustering algorithm to characterize patterns in

eddy trajectories.

Chapter 5 describes the implications and areas for future work from the results in this dissertation.

Chapter 6 provides a brief summary of our findings in Chapters 2, 3, and 4.

Chapter 2

MODELED SURF-ZONE EDDIES ON A LABORATORY SCALE BARRED BEACH WITH VARYING WAVE CONDITIONS

How do wave conditions influence breaking waves, generation of vorticity, and development of cross-shore exchange?

2.1 *Introduction*

Cross-shore transport and exchange of material from the surf zone to the inner shelf influences larval dispersal, sediment transport, and nearshore water quality (*Moulton et al.*, 2023). An important mechanism that drives exchange between the surf zone and inner shelf are rip currents, which are fast moving, offshore directed flows. Rip currents can be caused by varying bathymetry, coastal infrastructure, and wave field hydrodynamics (*Castelle et al.*, 2016). Hydrodynamically controlled transient rip currents have been shown to drive cross-shore exchange up to two to four surf-zone widths from the shoreline in observations (*MacMahan et al.*, 2010a; *Hally-Rosendahl et al.*, 2014) and models (*Suanda and Feddersen*, 2015; *Grimes et al.*, 2020), but the link between transient rip current forcing to cross-shore exchange is still being understood.

Transient rip currents occur during directionally spread wave conditions, when wave breaking patterns lead to the generation of small scale horizontal rotational motions (eddies). Eddy motion is quantified by the surf zone vertical vorticity, with an evolution time scale that is long relative to the surface waves (*Spydell and Feddersen*, 2009; *Clark et al.*, 2012). The directional spread of a wave field quantifies the distribution of wave energy

about the mean wave direction. When a wave field has a large directional spread, waves from a range of directions interfere creating finite regions with larger wave amplitude. As depth-limited breaking begins, the regions where the waves have a larger amplitude break farther offshore, leading to wave breaking over finite lengths. This type of wave breaking is known as short-crested wave breaking (*Peregrine*, 1999).

As these short-crested waves break, vertical vorticity may be generated, particularly at the ends of the breaking waves (*Peregrine*, 1998; *Bühler and Jacobson*, 2001; *Johnson and Pattiaratchi*, 2006; *Sullivan et al.*, 2007; *Bonneton et al.*, 2010; *Bruneau et al.*, 2011; *Clark et al.*, 2012; *Wei et al.*, 2017; *Kirby and Derakhti*, 2019). The vorticity generated by short-crested wave breaking can be quantified by the along-crest gradient in wave breaking. For example, vertical vorticity injection has been hypothesized to be largest near the crest ends, where there is a transition from a broken to unbroken water surface (*Clark et al.*, 2012). However, laboratory estimates of vertical vorticity generation suggests that while vorticity can be generated at the wave crest ends, vorticity may also be generated along the crest (*Baker*, 2023). Wave driven vorticity forcing derived from a wave-resolved Boussinesq model, used to force a wave-averaged and circulation model, also show variability along individual wave crests (*Kumar and Feddersen*, 2017a), but directly quantifying the vorticity forcing associated with individual breaking crests and linking it to resulting surf-zone eddies and cross-shore exchange has not been done. Additionally, in three-dimensional large eddy simulations, small-scale variations of vorticity are present across the breaking wave and with depth (*Kirby and Derakhti*, 2019).

Small-scale eddies generated by short-crested wave breaking vorticity forcing can transfer energy to larger scales via eddy-eddy interaction, resulting in large-scale surf-zone eddies. These large-scale eddies can interact and form coherent vortex pairs that propagate offshore with intensified offshore flow between the eddy pairs. This eddy-driven cross-shore flow is known as a transient rip current (*Johnson and Pattiaratchi*, 2006). The cascade of energy from small scales to large scales that drive cross-shore exchange has been studied in a modeling, field, and laboratory framework. Modeling investigation

of the distribution of energy across scales in an alongshore current suggests that transfer of energy from small to large scales does occur in the surf zone, but is not entirely consistent with forced two-dimensional turbulence (*Feddersen*, 2014). Conversely, further work has shown that there is evidence to suggest that this inverse energy cascade may be consistent with forced two-dimensional turbulence in modeling, field, and laboratory settings (*Spydell and Feddersen*, 2009; *Elgar and Raubenheimer*, 2020; *Elgar et al.*, 2023; *Baker et al.*, 2023a). Larger directional spread is associated with greater vorticity variance and surf-zone dispersion (*Spydell and Feddersen*, 2009; *Clark et al.*, 2010; *Feddersen*, 2014; *Spydell et al.*, 2009; *O'Dea et al.*, 2021; *Baker et al.*, 2021), which, if consistent with forced two-dimensional turbulence, would suggest that vorticity forcing may scale with directional spread. Parameterizations of cross-shore exchange from numerical simulations on planar beaches suggests that exchange increases with increasing directional spread (*Suanda and Feddersen*, 2015), while other numerical studies do not find clear trends of exchange with directional spread for a smaller range of intermediate spreads (*O'Dea et al.*, 2021).

While relationships between wave conditions, vorticity variance, and cross-shore exchange have been studied, an investigation of the generation of eddies by individual breaking waves, wave-field characteristics, and the resulting large-scale eddies and cross-shore exchange is new. Large-scale laboratory experiments with barred bathymetry have quantified the relationship between wave conditions and the length of short-crested breaking waves to better understand the forcing mechanisms of eddy generation (*Baker et al.*, 2023b). Remote sensing observations of the wave field found that the mean breaking crest length decreases and the number of crest ends increases with increasing directional spread (*Baker et al.*, 2023b). This observed relationship is consistent and expected from linear wave theory (*Longuet-Higgins*, 1956; *Baker et al.*, 2023b). For a directionally spread wave field *Longuet-Higgins* (1956) has shown that the alongshore wavelength is expected to be related to the cross-shore surface gravity wavelength, L_x, and the angular deviation of the wave field from the mean direction. Assuming that that the angular deviation of the wave field can be approximated by the directional spread, σ_θ, and that the actively

breaking part of a crest is length of the wave above the mean water level, i.e. not the trough, or half of the alongshore wavelength then the expected breaking crest length, λ_c *Baker et al.* (2023b) has shown that λ_c can be estimated by:

$$\lambda_c = \frac{1}{2}\frac{L_x}{\sigma_\theta} \tag{2.1}$$

Thus, expected crest length varies with σ_θ, as well as with wave period through changes in L_x; however the link between breaking crest characteristics, the relationship of the crest length or number of crest ends with eddy generation and exchange is not well understood.

Estimates of vorticity generation in the field (*Clark et al.*, 2012), simulated vorticity variance (*Spydell and Feddersen*, 2009), and remotely sensed vorticity generation in a laboratory environment (*Baker*, 2023) have begun to relate eddy forcing mechanisms with wave conditions and resulting transient rip current activity. However, linking vorticity forcing directly with varying wave conditions, breaking wave characteristics, and resulting eddy variability and cross-shore exchange has not been quantified in a modeling framework. Prior work estimating fluctuating circulation generated during directionally spread wave conditions has suggested scaling relationships between wave directional spread and peak period and resulting surf-zone vorticity and exchange velocity on planar beaches (*Kennedy*, 2005; *Suanda and Feddersen*, 2015). Here, we examine how directional spread and peak period affect the generation of surf-zone vorticity at small scales through to the resulting largest scale and exchange velocity.

Phase-resolving numerical models can simulate the individual wave generation, propagation, and wave breaking that is necessary to simulate vorticity injection by individually breaking waves (*Shi et al.*, 2012; *Feddersen et al.*, 2011; *Kirby*, 2016). Phase-resolved Boussinesq type wave models have been used frequently to study nearshore processes including transient rip current dynamics (*Kumar and Feddersen*, 2017a,b; *O'Dea et al.*, 2021), cross-shore exchange (*Suanda and Feddersen*, 2015; *O'Dea et al.*, 2021), and tracer dispersion (*Spydell and Feddersen*, 2009; *Clark et al.*, 2011; *Feddersen et al.*, 2011; *Feddersen*, 2014; *Kumar*

and Feddersen, 2017c) because they can simulate directionally spread irregular wave fields, wave propagation and transformation, nonlinear wave-wave and wave current interaction, and wave breaking with runup and overtopping (*Shi et al.*, 2012). Depth-averaged simulations do not include depth-variation in vorticity forcing that may alter low-frequency rotational energy transfers (*Kirby and Derakhti*, 2019; *Marchesiello et al.*, 2021) and exchange processes in the presence of inner-shelf stratification (*Kumar and Feddersen*, 2017b; *Grimes et al.*, 2019), but are more extensively tested with previous observations of surf-zone low-frequency eddy activity and less computationally expensive than three-dimensional models. In addition, eddy dynamics are expected to be largely two-dimensional in the surf zone (*Baker et al.*, 2021). Therefore, we use FUNWAVE-TVD to resolve how wave conditions influence surf-zone vorticity generation and evolution across the surf zone. Model simulations were configured to simulate conditions observed during large-scale laboratory experiments (*Baker et al.*, 2023b) for a range of wave directional spreads and peak periods.

In this study, we use FUNWAVE-TVD to simulate wave conditions for varying directional spread and peak period on a laboratory-scale barred beach. In situ and high-resolution remotely sensed observations from *Baker et al.* (2023b) are used to evaluate model performance and the cross-shore evolution of the wave field. Breaking wave crest characteristics, including mean crest length and crest end density, are quantified for varying wave conditions and compared with remote sensing observations and wave theory. Vorticity forcing is estimated from simulations and examined as a function of wave condition across the surf zone, as well as the variation along and between individual breaking crests. Additionally, low frequency eddy activity and cross-shore exchange are quantified to link the wave field forcing to resulting eddy dynamics. These metrics are used to understand the evolution of surf-zone eddies, from wave-breaking driven vorticity forcing to cross-shore exchange for varying wave conditions on a laboratory-scale barred beach.

2.2 *Methods*

2.2.1 *Laboratory Experiments*

Large-scale laboratory experiments were performed in the Directional Wave Basin at the Oregon State University O.H. Hinsdale Wave Research Laboratory (`https://wave.oregonstate.edu/`). The basin is 48.8 m long (alongshore, y), 26.5 m wide (cross-shore, x), and up to 2 m deep (bathymetry, z with $z = 0$ at mean water surface) with a 29-board piston type wavemaker used to simulate directionally spread irregular waves (*Schäffer and Steenberg*, 2003). These irregular wave conditions spanned varying directional spreads (σ_θ), significant wave heights (H_s), peak periods (T_p), and still water levels. High-resolution water surface elevation maps were estimated from a three-dimensional scanning lidar and stereo image techniques. Post-processed 8-Hz stereo reconstruction from three ceiling-mounted cameras yielded 5-cm resolution elevation maps of the surf zone (x=27.5–35 m) spanning the width of the tank (region onshore of dotted white line in Fig. 2.1c). Additionally, a three-dimensional scanning multibeam lidar measured the water surface elevation at 10 Hz across the tank width with a spatial footprint extending farther offshore ($x = 22 - 34$ m) but with lower resolution ($dx = 0.5$ m,$dy = 0.25$ m) than stereo methods (highlighted region shown in Fig. 2.1c). Pressure and velocity were measured with colocated near-bed pressure gauges and acoustic Doppler Velocimeters (ADVs, Vectrino Profiler) sampling at 100 Hz. In situ sensors were initially deployed in a 'surf-zone array' (x = 28.4, 30.7 m), and then repeated trials wave conditions were performed with in situ sensors in an 'inner-shelf array' (x = 26.6 m) nearly spanning the tank width (circles and squares in Fig. 2.1c). Additionally, an 'offshore array' of 15 surface-piercing wire resistance gauges (sampling at 100 Hz) provided sea surface elevation estimates offshore of the beach slope (triangles in Figure 2.1c). A full description of laboratory experimental setup, instrumentation, and wave conditions can be found in *Baker et al.* (2023b).

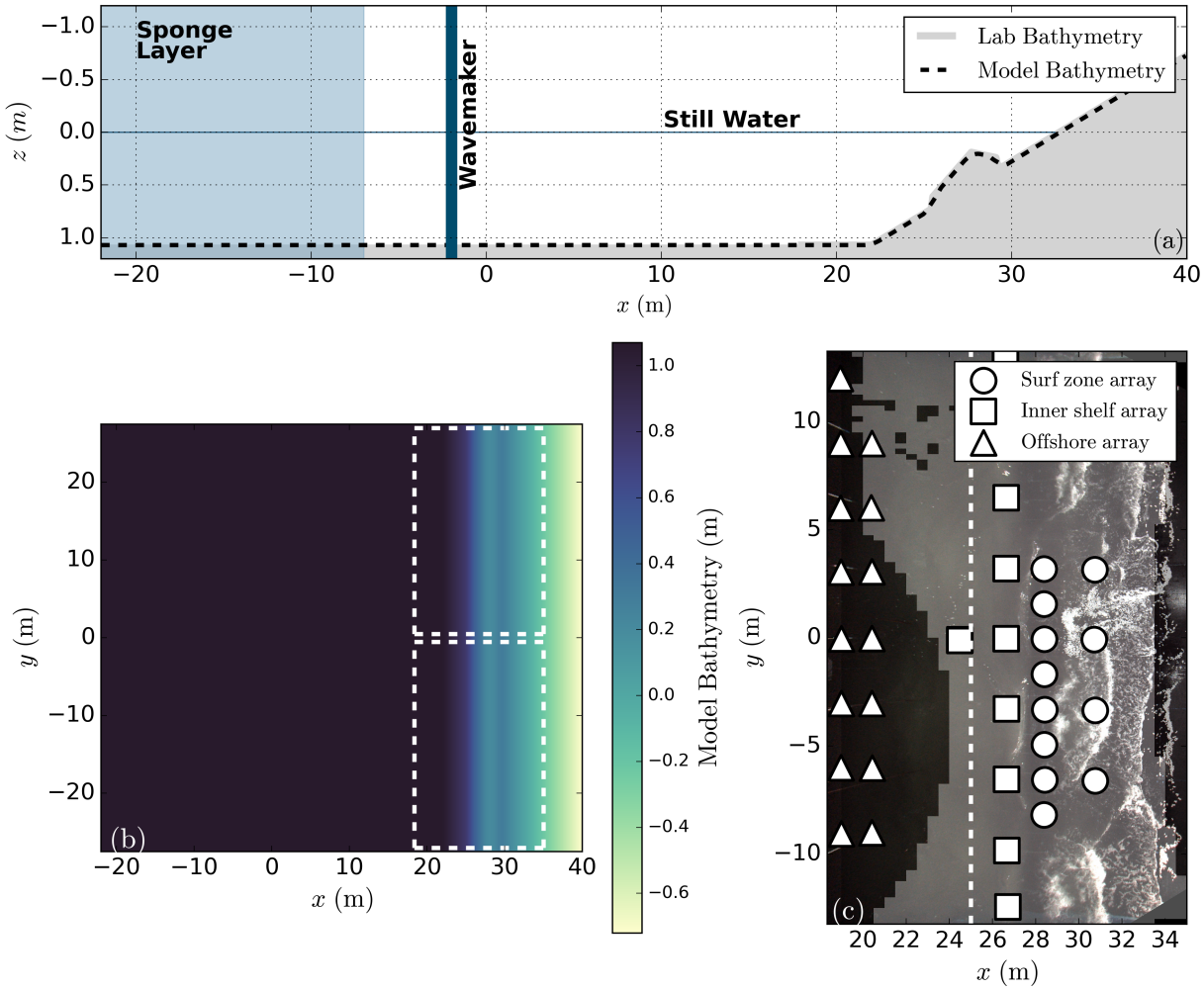

Figure 2.1: (a) Cross-shore profile of laboratory (grey) and model (dashed) beach slope with location of sponge layer (shaded blue) and wavemaker (dark blue vertical line). (b) Planar view of model bathymetry (color contours) with the lab extent (shown in c) used for analysis (dashed white boxes). (c) Planar view of waves during trial *G2d* in the laboratory basin with co-located in situ pressure sensors and ADVs in the surf zone (circles) and inner shelf (squares), wire resistance gauges (triangles), with lidar footprint highlighted (image darker outside of the lidar footprint), and offshore extent of stereo reconstructions (dashed white).

2.2.2 *Numerical Model Setup*

Directionally spread irregular wave conditions were simulated with FUNWAVE-TVD (*Shi et al.*, 2012), a wave-resolving model that solves the fully nonlinear depth-averaged Boussinesq equations (*Chen et al.*, 2000) and parameterizes wave breaking with an induced eddy viscosity similar to *Kennedy et al.* (2000) (see Section 2.2.3 for details).

The laboratory cross-shore bathymetry is smoothed by a running mean with a 1-m window to remove sharp features that can lead to numerical instability, while preserving the shape of the slope and bar (Fig. 2.1a). The model bathymetry is alongshore uniform to exclude depth-induced alongshore variability in wave breaking and resulting rip currents (Fig. 2.1b). FUNWAVE-TVD was configured to simulate wave conditions observed during the laboratory experiments with an extended cross- and alongshore extent ($D_x = 55$ m, $D_y = 62$ m). This grid size allows for simulation of two non-overlapping laboratory sized sub-regions (white dotted regions in Fig. 2.1b), which are used in some analysis to provide a more direct comparison with *Baker et al.* (2023b) and assess the influence of domain size. Cross-shore grid spacing (dx) is 0.05 m and alongshore grid spacing (dy) is 0.1 m, which are sufficiently small to resolve length scales associated with laboratory scale surface gravity wavelengths and surfzone eddies.

Periodic boundary conditions are applied at the $y = -27.5$ and $y = 27.5$ boundaries of the grid to minimize reflections off of the boundary. In FUNWAVE-TVD, the finite wavemaker length and periodic boundary conditions restrict the alongshore wavelengths that can be represented by the wavemaker and resolved in the wave field (*Shi et al.*, 2016). Small alongshore model length (D_y) can result in poor representation of the wave field and lead to alongshore variations in significant wave height (H_s) that persist in the same locations through time. Wave coherence also contributes to these persistent alongshore H_s patterns (*Salatin et al.*, 2021). To minimize persistent alongshore H_s patterns, we chose D_y = 55 m and 0% wave coherence. At 0% wave coherence H_s produces no stationary alongshore patterns, while 50% and 100% wave coherence produce increasingly strong

alongshore patterns in H_s (*Salatin et al.*, 2021). While H_s does vary in time at any given alongshore location due to natural variation of random irregular waves (shaded range in Fig. 2.3a), computed over the entire 25 minute model run, H_s varies minimally by 1.8 cm on average in the alongshore.

To provide sufficient space for an offshore sponge layer and $\sim 3-4$ wavelengths between the wavemaker and the toe of the beach slope, the flat offshore portion of the laboratory bathymetry is extended (Fig. 2.1a). The numerical wavemaker is 20 m shoreward of the offshore boundary (2 m offshore of the laboratory wavemaker), allowing for a 15-m wide sponge layer to absorb offshore directed wave energy. The depth of the offshore region of the model, encompassing the sponge layer and wavemaker, is 1.07 m (identical to laboratory experiments). Waves were generated using a TMA spectra with $\gamma = 3.3$, equivalent to the Jonswap spectra implemented for the laboratory wavemaker. The frequency range of the spectrum is 0.33 - 2.5 Hz and 0° - 360°, which is discretized into a number of frequency bins, N_{freq}, and directional bins, N_{theta}. The *Salatin et al.* (2021) wavemaker discretization with 0% coherence has no repeated frequencies, thus the total number of distinct frequencies is $N_{tot} = N_{freq} \cdot N_{theta}$. For all model runs $N_{freq} = 100$, but N_{theta} varied for low directional spread runs and larger directional spread runs, thus N_{tot} varied between runs (Table 2.1).

The selection for N_θ influences the representation of the wave field by setting the resolution of the directional spectrum. For small directional spreads, large N_θ leads to an increase in persistent alongshore H_s patterns, but very small N_θ leads to under representation of the directional spread. Thus, N_θ was chosen to minimize persistent alongshore patterns and maximizing accuracy of simulated directional spread. In addition to N_θ, the alongshore length of the model domain limits the alongshore wavenumbers that can be generated by the numerical wavemaker (*Wei et al.*, 1999), which can bias simulated spreads low compared to input values at high spreads (*Suanda et al.*, 2016). Wavemaker parameters were chosen to maximize simulated directional spread, but simulating two laboratory regions sets the alongshore length and limits simulated directional spread at

large spreads. Input wavemaker parameters, including directional spread and estimated directional spread from model output are provided in Table 2.1 for reference, but actual simulated values are used for analyses. Lastly, the wavemaker width parameter, δ, was set to 2.5 for numerical stability and wave field representation accuracy (*Wei et al.*, 1999; *Suanda et al.*, 2016) and the wavemaker generation had a time ramp of 20 s.

Model simulations were run for 25 minutes with a cfl condition of 0.1, resulting in each simulation requiring ∼11,000 core-hours to complete. The 25-minute model run length was chosen to allow for a 5 minute spin up period and two 10 minute analysis windows. The length of the analysis window was set to be consistent with laboratory analysis (*Baker et al.*, 2023b; *Baker*, 2023). Shore-normal wave conditions were simulated with a 0.25 m significant wave height (H_s) and varying input directional spreads (σ_θ = 0°-40°) and peak periods ($T_p = 1.5, 2.0,$ &2.5 s, kh = 0.9 - 2). Wave height was not varied for this study, as the laboratory study found that results were similar for $0.2 < H_s < 0.3$, likely because waves were depth-limited onshore of the bar crest (*Baker et al.*, 2023b). See Table 2.1 for all model input and estimated wave parameters.

2.2.3 *Quantifying Wave Conditions and Eddy Dynamics Forcing*

Wave Statistics

In situ sea surface elevation and velocity measurements are used to compare wave statistics and spectra to simulated dynamics for our model base case (*M2d*, Table 2.1). Pressure gauge measurements are converted to sea surface elevation estimates using the hydrostatic approximation, and then adjusted with a depth-attenuation correction according to linear wave theory to account for the diminished pressure signal of high frequency waves (*Guza and Thornton*, 1980; *Bishop and Donelan*, 1987). From simulated sea surface elevation and corrected pressure gauge data, H_s is computed as:

$$H_s = 4\sqrt{\int_{f_1}^{f_2} S_{\eta\eta}(f)\mathrm{df}} \tag{2.2}$$

where f_1 = 0.25 and f_2 = 1.2 Hz. Alongshore averaged H_s and T_p are reported offshore ($x = 15$ m) and at the surf zone edge for each model simulation (Table 2.1). The offshore edge of the surf zone is defined as the cross-shore position where the energy flux is 90% of its offshore magnitude. On average, across all wave conditions the cross-shore position of the surf-zone edge is $x \simeq 23.2$ m (Table 2.1 for all model simulations). The minimum extent of rundown, as defined as the most offshore "dry" grid point, is $x \simeq 32.5$ across all model simulations, but we choose the onshore edge of the surf zone to be $x = 31.5$ m because the average water depth onshore of $x = 31.5$ m is less than 1 cm. Thus our surf zone width (W_{sz}) is approximately 8.3 m. For analyses that use surf zone area scaling or are computed at the surf zone edge location, an average x_{sz} = 23.2 m and W_{sz} = 8.3 m are used for all model simulations. While the surf zone edge location does vary slightly between simulations (<0.8 m, Table 2.1), this variation is within the average standard deviation surf zone edge location (∼1 m) when computed over 1-minute time windows within each simulation.

Sea surface elevation, $S_{\eta\eta}$, and velocity spectra, $S_{uu} + S_{vv}$, are computed from model output and in situ data using a Hanning window period of 102.4 s and an overlap window of 51.2 s over the full laboratory trial and the entire model run, excluding the initial 5 minutes. The in situ data is also averaged across in situ gauges in the alongshore, while all model grid points are averaged in the alongshore (in situ DOF = 144, Model DOF = 644) (Figure 2.3b-e). Sea surface elevation spectral density is converted to equivalent velocity units assuming linear wave theory by multiplying by $\left(\omega \frac{\cosh(k(z+h)}{\sinh(kh)}\right)^2$, where k are the wavenumbers associated with the spectral frequencies $f = \omega/(2\pi)$ given the water depth (h) and sensor elevation (z).

Additionally, simulated sea surface elevation and velocity are used to estimate the wave directional moments (a_2, b_2) using a single point PUV approach (*Kuik et al.*, 1988). The directional moments are used to compute the mean direction ($\theta(f)$) and directional spread ($\sigma_\theta(f)$) as a function of frequency and then are energy weighted to estimate representative bulk θ and σ_θ (*Suanda et al.*, 2016; *Baker et al.*, 2023b). Both θ and σ_θ are

Table 2.1: Significant wave height (H_s), peak period (T_p), wave direction (θ), and directional spread (σ_θ) input to numerical wavemaker, measured offshore between wavemaker and toe of the beach slope (x = 15 m), and at the offshore surf zone edge (x_{sz}). Additionally, the mean water level (x_{sl}) and lowest extent of rundown (x_r) are reported for determining surf zone box area (A_{sz})

Location	Statistic	*M2a*	*M2b*	*M2c*	*M2d*	*M2e*	*M2f*	*M15d*	*M25d*
Input	H_s (m)	0.25	0.25	0.25	0.25	0.25	0.25	0.25	0.25
	T_p (s)	2	2	2	2	2	2	1.5	2.5
	$\theta(^\circ)$	0	0	0	0	0	0	0	0
	σ_θ $(^\circ)$	1.0	5.0	10.0	20.0	30.0	40.0	20.0	20.0
Wavemaker	N_{theta}	5	15	25	25	25	25	25	25
Inputs	N_{freq}	500	1500	2500	2500	2500	2500	2500	2500
Offshore (x = 15m)	H_s (m)	0.24	0.24	0.24	0.23	0.22	0.22	0.25	0.22
	T_p (s)	2.0	2.0	2.0	2.0	2.0	2.0	1.5	2.3
	θ $(^\circ)$	0.0	0.0	0.0	0.0	0.0	0.0	0.2	0.0
	σ_θ $(^\circ)$	0.2	3.4	9.7	16.4	22.1	25.6	17.5	16.2
Surf zone edge	x_{sz} (m)	22.8	23.6	23.4	23.3	23.2	23.2	22.8	23.4
Surf zone edge ($x = x_{sz}$)	H_s (m)	0.23	0.23	0.23	0.23	0.22	0.21	0.24	0.21
	T_p (s)	2.0	2.0	1.8	2.0	2.0	2.0	1.5	2.3
	θ $(^\circ)$	0.0	0.0	-0.1	0.0	-0.1	0.0	0.0	0.0
	σ_θ $(^\circ)$	0.3	3.8	11.2	16.5	21.6	24.9	17.8	15.6

estimated offshore ($x = 15$ m) and at the surf zone edge (x = 23.2 m) and then alongshore averaged and reported for each model simulation (Table 2.1).

Model simulations were setup to encompass the range of wave conditions observed during laboratory trials (*Baker et al.*, 2023b) and explore similar relationships between directional spread, breaking wave properties, and eddy dynamics to complement laboratory data analysis, rather than perfectly simulate the exact laboratory conditions. For example, the model domain is more than two times the laboratory basin length and used

periodic boundary conditions. The longer domain and periodic boundary conditions allows for eliminating limitations of reflective side walls that are present in the laboratory basin. Additionally, the increasing alongshore length allows for simulation of increased alongshore uniformity of H_s across the model domain by increasing the number of alongshore wavenumbers that can be generated by the wavemaker. By increasing alongshore H_s uniformity, we can focus on breaking wave crest and vorticity forcing in statistically uniform conditions. Despite these differences in configuration, laboratory data and model simulation comparison is still valuable for model performance and complementary analysis. To provide comparison of the range of wave conditions encompassed by the simulations and laboratory trials, Table 2.1 can be compared to Table 1 in *Baker et al.* (2023b). A detailed model evaluation of the performance of our model configuration compared to observed laboratory dynamics is focused on comparing *M2d*, our model base case, with laboratory trial *G2c* (*Baker et al.*, 2023b) (Section 2.3.1).

Crest Identification

Actively breaking waves are identified from the model simulations to compute crest statistics. Crest identification and estimation of crest statistics from the model follows a similar method as the Remote Breaker Identification Scheme (RBIS) (*Baker et al.*, 2023b), which identifies breaking waves with remote sensing observations of sea surface elevation and foam brightness. In the model, breaking waves can be identified by wave breaking parameters used to simulate wave breaking. Wave breaking is parameterized in FUNWAVE-TVD by adding a damping term to the momentum equation that includes a parameterized viscosity:

$$\nu_{br} = B\delta^2(h+\eta)\eta_t \tag{2.3}$$

where ν_{br} is a breaking-induced eddy viscosity that dissipates energy proportional to the strength of wave breaking (*Shi et al.*, 2012; *Kennedy et al.*, 2000), $B = 0$ when waves are not breaking, then $B = 1$ when the sea surface exceeds an initial threshold steepness

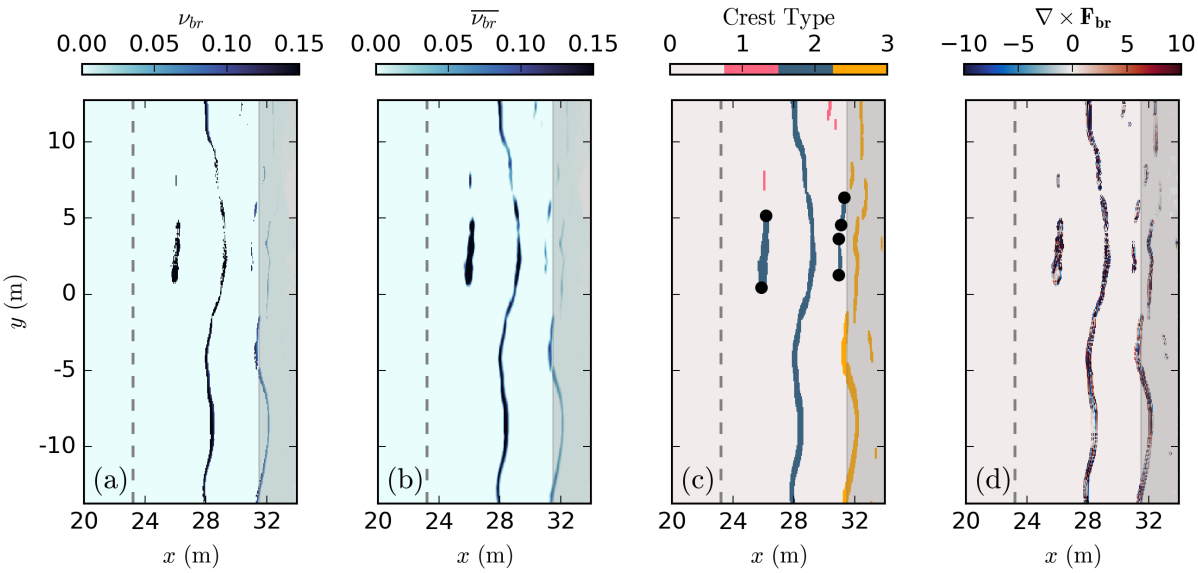

Figure 2.2: Planar view of crest identification and vorticity forcing processing over one lab region with dashed grey line denoting the surf-zone edge. (a) Raw wave breaking induced viscosity (ν_{br}, kg m^{-1} s^{-1}) and (b) 0.5-m spatially averaged wave breaking induced viscosity ($\overline{\nu_{br}}$) are used to identify actively breaking waves. (c) Identified waves are excluded from crest statistics if their area is below area limit (1- pink) or if they are within the swash zone (x>31.5 m, 3 - yellow), all other breaking wave crests within the surf zone are retained (2 - blue). Black dots denote crest ends used in crest end density calculation. (d) The x and y component of the wave breaking force are estimated from the smoothed ν_{br} and then the vorticity forcing ($\nabla \times \mathbf{F_{br}}$, s^{-2}) is computed.

($\eta_t \geq 0.45 \times 2\sqrt{gh}$), η is the sea surface elevation, and η_t is the time derivative of the sea surface elevation (or wave steepness). Wave breaking continues (B = 1) until η_t drops below another threshold ($\eta_t < 0.15\sqrt{gh}$), after which B = 0 to simulate the cessation of breaking (*Choi et al.*, 2018a).

Actively breaking waves are identified by the region associated with non-zero $\overline{\nu_{br}}$ (darker blue in Fig. 2.2b). Across an individual actively breaking crest, ν_{br} exhibits small-scale variability. This small-scale variability can lead to small gaps within an individual crest. Filtering of ν_{br} smooths small-scale variability and helps to clearly identify a

connected set of breaking points attributed to one breaking wave. Therefore, the raw ν_{br} (Fig. 2.2a) is spatially filtered at each time step with a first-order 2D Lanczos filter with filter half-widths of 0.5 m in the x and y directions (Fig. 2.2b) to identify connected grid points associated with an individual actively breaking wave (Fig. 2.2c). Following *Baker et al.* (2023b), individual wave crests that have a total area of less than 0.375 m^2 were removed from crest statistics (Fig. 2.2c, pink crest) as they do not represent significant coherent crest features. Breaking crests were identified across $x = 15 - 35$ m, but crests identified in the swash zone ($x > 31.5$ m) were removed and excluded from crest statistics (Fig. 2.2c, yellow crests).

Crest statistics, including the length and number of ends across the surf zone, are estimated for each model run from the identified breaking crests. The length of each breaking wave (λ_c) is measured as the distance along an along-crest transect through the identified region. The crest length is the length of a line transecting a wave crest, where the transect is determined by taking the distance along the center of the breaker in the cross-shore at every alongshore position (0.1 m spacing) along the wave. In addition to comparing estimated λ_c to laboratory estimates of crest length (*Baker et al.*, 2023b), λ_c is also compared to theoretical crest lengths. Following *Longuet-Higgins* (1956); *Baker et al.* (2023b), a theoretical expected breaking crest length is estimated using Eq. 2.1. The cross-shore wavelength (L_x) is estimated by using the dispersion relationship and peak period at the surf zone edge, then L_x and σ_θ at the surf zone edge are substituted into Eq. 2.1. The total number of crest ends (N_{ce}) at a given time step was also estimated. Similar to *Baker et al.* (2023b), a crest end(s) was excluded if it was near the swash zone ($x > 31.5$ m) or if the crest end was within 0.2 m of the domain edges. Additionally, to compare the number of crest ends observed in the model simulations with the laboratory estimates, which have differing surf-zone areas, we estimate the crest end density (d_{ce}). Crest end density is defined as:

$$d_{ce} = \frac{N_{ce}}{W_{sz} D_y} \tag{2.4}$$

where N_{ce} is the number of crest ends at a given time step and $W_{sz} D_y$ is the model surf

zone area.

Quantifying Wave Breaking Vorticity Forcing

The breaking force ($\mathbf{F}_{\mathrm{br}}$) was computed from the wave breaking induced eddy viscosity, ν_{br} (Equation 2.3), as:

$$F_{br,x} = \frac{\partial}{\partial x}\left(\nu_{br}\frac{\partial Hu}{\partial x}\right) + \frac{\partial}{\partial y}\left(\nu_{br}\frac{\partial Hu}{\partial y}\right) \tag{2.5}$$

$$F_{br,y} = \frac{\partial}{\partial y}\left(\nu_{br}\frac{\partial Hv}{\partial y}\right) + \frac{\partial}{\partial x}\left(\nu_{br}\frac{\partial Hv}{\partial x}\right) \tag{2.6}$$

where u and v are cross and alongshore velocity and $H = h + \eta$, where h is local water depth (*Shi et al.*, 2016). Equations 2.5 and 2.6 are similar to *Kennedy et al.* (2000) wave breaking parameterization, but are modified in FUNWAVE-TVD to use transport velocities (hu), rather than only velocity (*Shi et al.*, 2016).

In a depth integrated Boussinesq model, the momentum equation is described by (*Spydell and Feddersen*, 2009; *Feddersen et al.*, 2011; *Kirby and Derakhti*, 2019):

$$\frac{\partial \overline{\mathbf{u}}}{\partial t} + \overline{\mathbf{u}} \cdot \nabla_h \overline{\mathbf{u}} + g\nabla_h \eta = \mathbf{F_{br}} \tag{2.7}$$

where $\overline{\mathbf{u}}$ is depth-averaged velocity and ∇_h is a horizontal operator. In the surf zone it is hypothesized that at small spatial scales, the time evolution of vertical vorticity is approximately equal to the rotational component of the wave-breaking force(*Feddersen et al.*, 2011; *Spydell and Feddersen*, 2009), $\mathbf{F_{br}}$, such that:

$$\frac{\partial \omega}{\partial t} \simeq \nabla \times \mathbf{F_{br}} \tag{2.8}$$

Thus, $\nabla \times \mathbf{F_{br}}$, later referred to as 'vorticity forcing', provides the approximate input of vorticity into the water column.

We estimate the total vorticity forcing input per wave crest (Ω_c) by integrating the magnitude of $|\nabla \times \mathbf{F_{br}}|$ over each identified crest such that:

$$\Omega_c = \int_{A_{c,i}} |\nabla \times \mathbf{F_{br}}| \, \mathrm{d}A_{c,i} \tag{2.9}$$

where Ω_c is the vorticity forcing associated with an individual crest and $A_{c,i}$ is the area of the individual crest. The total vorticity forcing input across the surf zone (Ω_{sz}) at a given time was estimated as:

$$\Omega_{sz} = \sum_{i=0}^{N_c} \int_{A_{c,i}} |\nabla \times \mathbf{F_{br}}| \, \mathrm{d}A_{c,i} = \sum_{i=0}^{N_c} \Omega_{c,i} \tag{2.10}$$

where Ω_{sz} is the vorticity forcing across the surf zone, N_c is the number of crests in the surf zone at a given time, and $A_{c,i}$ is the area of a given crest. Similarly to estimating the crest end density, we compute the vorticity forcing per unit area:

$$d_\Omega = \frac{\Omega_{sz}}{W_s z D_y} \tag{2.11}$$

.

2.2.4 *Quantifying Eddy Dynamics*

Velocity Decomposition

To quantify flows associated with rotational eddy motions, we decompose the two-dimensional velocity field into an irrotational component that can be described with the gradient of a velocity potential, ϕ, and a rotational component that is the curl of the streamfunction, ψ, such that:

$$\mathbf{u} = \mathbf{u}_\phi + \mathbf{u}_\psi = \nabla\phi + \nabla \times \psi \tag{2.12}$$

where the $\mathbf{u}_\phi = \nabla\phi$ is the irrotational velocity and $\mathbf{u}_\psi = \nabla \times \psi$ is the rotational velocity. Following *Spydell and Feddersen* (2009), to decompose the velocity field we use periodic boundary conditions in the alongshore for both ϕ and ψ, $\psi = 0$ and $\partial_x \phi = 0$ at the onshore boundary, and apply $\psi = \int \langle v \rangle \mathrm{dx}$ and $\phi = \int \langle u \rangle \mathrm{dx}$ at the offshore boundary, where $\langle\rangle$ denotes an alongshore average. To quantify accuracy in the velocity decomposition, the time and space averaged root-mean-square (rms) error is computed between the modeled velocity, $\mathbf{u}$, and reconstructed velocity field ($\mathbf{u}_\phi$+$\mathbf{u}_\psi$). The time and spatially averaged rms error is less than 0.01 m s^{-1} for all model simulations.

Quantifying Low Frequency Rotational Motion

Power of low frequency rotational motions associated with surf-zone eddies in model simulations is quantified spectrally as:

$$V^{\psi} = \int_{f_1}^{f_2} S_{u_\psi u_\psi}(f) + S_{v_\psi v_\psi}(f) \mathrm{d}f \tag{2.13}$$

where f is frequency, f_1 and f_2 are the respective minimum and maximum frequencies, and u_ψ and v_ψ are the respective x and y components of the rotational velocity. The rotational velocities are demeaned and detrended prior to computing spectra. Spectra are estimated using a Hanning window period of 102.4 s and an overlap window of 51.2 s over the last 20 minutes of each model run, which is the duration of the model run excluding the spin up period. Spectra are then averaged across all model grid points in the alongshore (DOF = 644). Estimates of V^{ψ}_{vlf} and V^{ψ}_{lf} are then averaged across the surf zone (x = 23.2 - 31.5 m) to provide an overall metric of rotational motion within the surf zone for each model simulation. We estimate low-frequency eddy power (V^{ψ}_{lf}) from rotational velocities across all low-frequency bands ($f_1 = 0.003$ Hz and $f_2 = 0.2$ Hz). The upper end of this frequency band was chosen to correspond with the transition from infragravity to surface gravity waves (Fig. 2.3b-e).

To compare eddy activity in the model simulations with in situ data we estimate power associated with very low frequency motions (V^{ψ}_{vlf}), corresponding to f_1 = 0.003 Hz and f_2 = 0.02 Hz ($\sim T_p \times 25$) consistent with prior literature to avoid inclusion of infragravity waves (*Baker et al.*, 2023b; *MacMahan et al.*, 2010b; *Elgar et al.*, 2019). Very low frequency power estimated from model simulations are compared with estimates of V^{ψ}_{vlf} from in situ velocity measurements, described in *Baker* (2023). The very low frequency band used here overlaps with the lowest frequencies used for estimating V^{ψ}_{lf}, but as the laboratory in situ velocity data is not decomposed into rotational and irrotational components, we only present lab observations in this band, where velocities are primarily due to rotational motions *Baker* (2023).

Estimating Exchange Velocities

To quantify the cross-shore exchange velocities associated with eddy activity and transient rip currents, we follow *Suanda and Feddersen* (2015) and compute:

$$U_{ex}(x) = \left\langle \frac{1}{D_y} \int_0^{D_y} |u_\psi^-(x,y,t)| \, \mathrm{dy} \right\rangle \tag{2.14}$$

where u_ψ^- is set to zero for any onshore directed rotational velocities such that only the offshore directed rotational velocities are included in the average, and $\langle\rangle$ denote time averaging. Cross-shore exchange velocities are estimated at each time step and averaged over the last 20 minutes, the entire model run excluding the 5 min spinup period.

Alongshore wavenumber spectra

Alongshore wavenumber spectra are computed on alongshore transects of vorticity at each time step from 5 - 25 minutes of model simulations to quantify vorticity variance across scales. Spectra are computed over the entire alongshore transect (55 m) for every cross-shore position from 31.5 - 20 m ($0.2W_{sz} - 1.5W_{sz}$). Spectra are then averaged across cross-shore zones, consistent with (*Baker et al.*, 2021), following low frequency motion cross-shore zones above; the inner-surf (x = 31.5 - 27.4 m), the outer-surf (x = 27.4 - 23.2 m), and the surf-zone edge and offshore (x = 23.2 - 19.1 m).

2.3 Results

2.3.1 Model evaluation with laboratory observations

Cross-shore significant wave height (H_s) is consistent between modeled and in situ estimates for trial *G2c* forcing (Figure 2.3a). Model consistency of cross-shore H_s with in situ data is similar to model performance of three-dimensional phase-resolved simulations of laboratory experiments (*Treillou et al.*, 2024). Remote sensing estimates of H_s are also similar to modeled and in situ values, except near the bar crest ($x \sim 27$ m), where the presence of plunging waves with air pockets leads the remotely sensed sea surface to

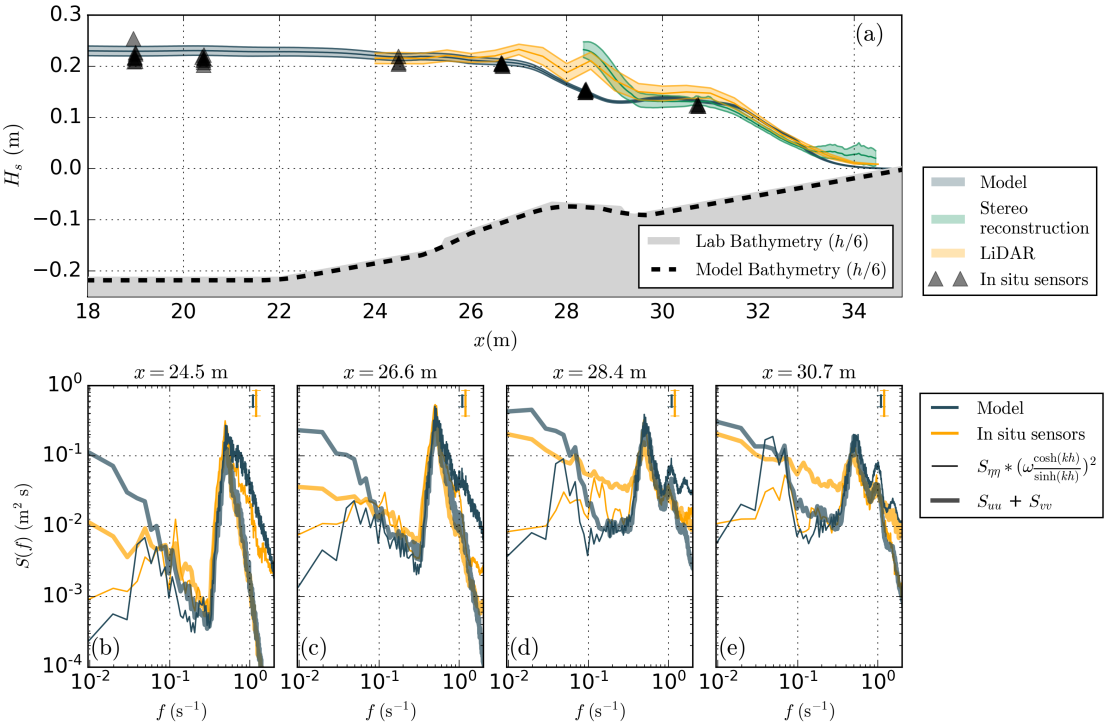

Figure 2.3: Comparison of model base case (*M*2*d*) with laboratory trial *G*2*c*. (a) Cross-shore profile of the alongshore averaged significant wave height (H_s) from model output (blue), LiDAR (yellow), and stereo reconstructions (green) with shaded region denoting +/- 1 standard deviation. Black triangles denote H_s estimates from in situ sensors. The lab (grey) and modeled (dashed black) beach slope are shown as $h/6$. (b-e) Sea surface elevation spectral density converted to equivalent velocity (thin lines) and the sum of the cross and alongshore spectral densities (thick lines) from the model (blue) and in situ gauges (yellow). 95% confidence intervals for model and in situ spectra noted in upper right corner.

be higher than estimated from subsurface pressure gauges or in the model (*Baker et al.*, 2023b). Additionally, remote sensing estimates may underestimate the water surface during small waves sets with little surface foam (*Baker et al.*, 2023b). As FUNWAVE-TVD parameterizes wave breaking by dissipating wave energy through eddy viscosity, model simulations cannot capture the double-valued sea surface associated with plunging waves, only their dissipation, so modeled H_s are expected to match *in situ* pressure observations more closely in this region.

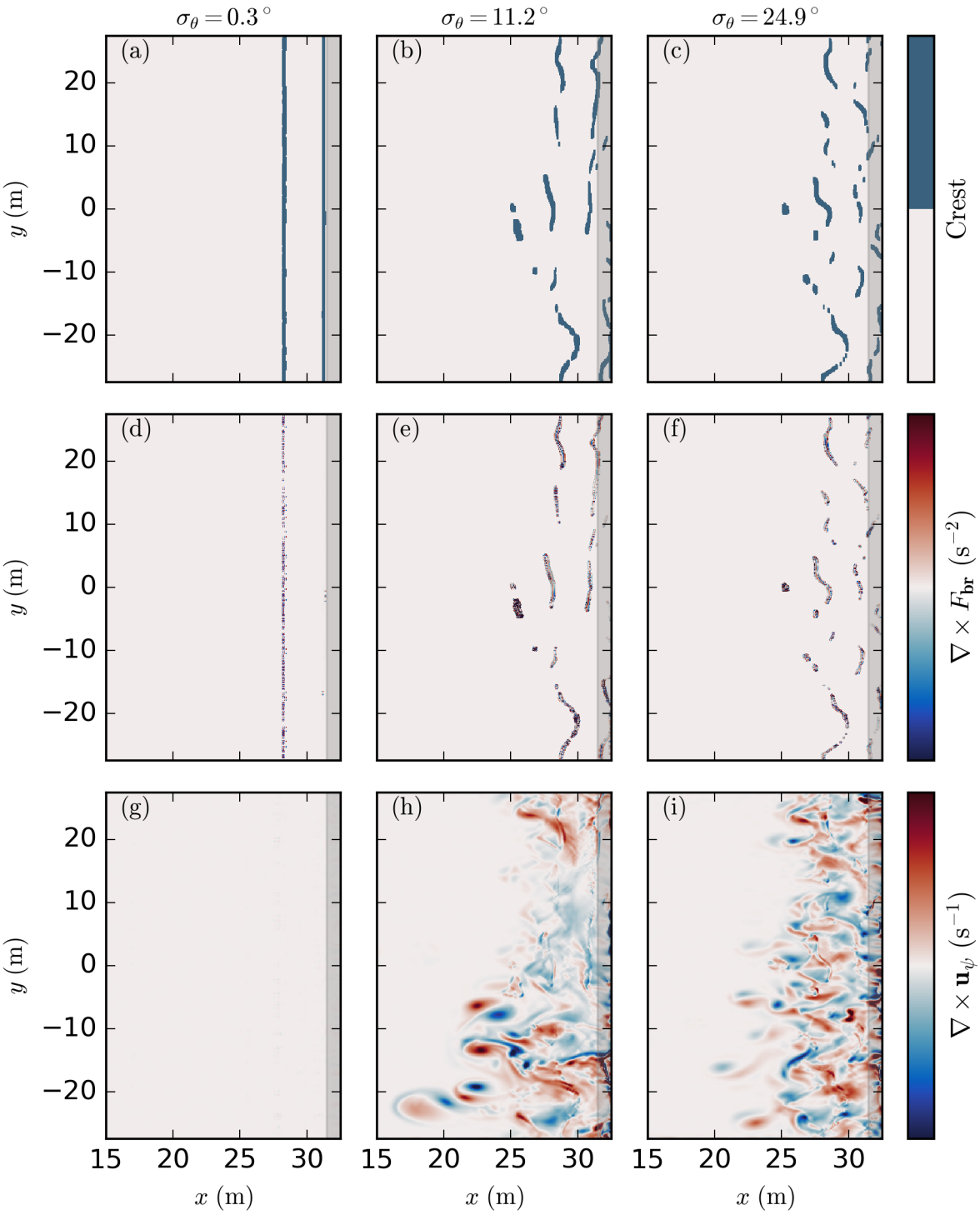

Figure 2.4: Snapshots of identified breaking crests (a-c), vorticity forcing ($\nabla \times \mathbf{F_{br}}$) (d-f), and vorticity ($\nabla \times \mathbf{u}_\psi$) (g-i) for low, $\sigma_\theta = 0.3^\circ$ (a,d,g), mid, $\sigma_\theta = 11.2^\circ$ (b,e,h), and high, $\sigma_\theta = 24.9^\circ$ (c,f,i) directional spreads as a function of their cross- (x) and alongshore (y) position.

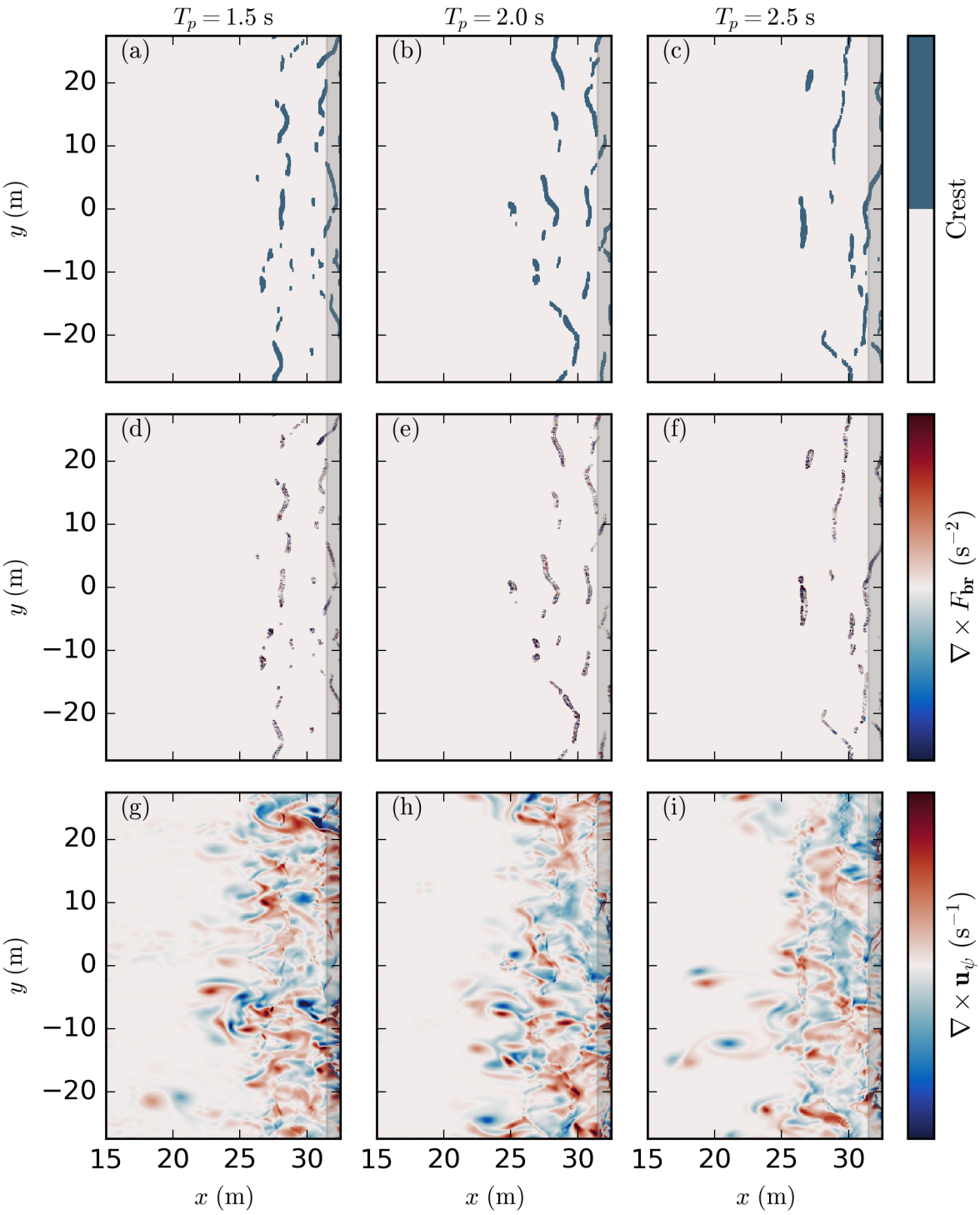

Figure 2.5: Snapshots of identified breaking crests (a-c), vorticity forcing ($\nabla \times \mathbf{F_{br}}$) (d-f), and vorticity ($\nabla \times \mathbf{u}_\psi$) (g-i) for varying peak period, T_p = 1.5 s (a,d,g), T_p = 2.0 (b,e,h), and T_p = 2.5 (c,f,i) as a function of their cross- (x) and alongshore (y) position.

Modeled and observed sea surface elevation ($S_{\eta\eta}$) and velocity spectra ($S_{uu} + S_{vv}$) are similar over surface gravity frequencies ($f > 0.2$ Hz) at locations spanning the outer to inner surf zone, within the 95% confidence interval (Figure 2.3c-e). Below surface gravity frequencies (infragravity and low frequencies, $f < 0.2$ Hz), $S_{\eta\eta}$ also is similar in the model and observations. Modeled and observed velocity variance S_{uu}, S_{vv} in the outer surf zone are similar in the gravity and infragravity bands, and modeled spectra are nearly an order of magnitude larger energy than the laboratory spectra at very low frequencies ($0.003 < f < 0.02$ Hz) (Figure 2.3b,c), which is consistent with prior depth-averaged (*Newberger and Allen*, 2007; *Feddersen et al.*, 2011; *Marchesiello et al.*, 2021) and three-dimensional model performance (*Treillou et al.*, 2024). In the inner surf zone, simulated velocity has significantly less variance than laboratory observations in the infragravity band (Figure 2.3d,e). In the surface gravity wave and infragravity bands, modeled and observed velocities are largely explained by sea-surface elevation fluctuations, as evidenced by the similarity of velocity spectra to the sea-surface elevation spectra transformed to velocity assuming linear wave theory (see Section 2.2.3). In contrast, at very low frequencies, modeled and observed velocities have more energy than explained by sea-surface fluctuations, suggesting the presence of rotational motions (Figure 2.3b,c,d,e) (*Lippmann et al.*, 1999; *MacMahan et al.*, 2010a; *Feddersen et al.*, 2011; *Elgar et al.*, 2019).

2.3.2 *Directional spread and wave period dependence of modeled waves, vorticity forcing, and eddy activity*

At low directional spread (*M*2*a*), breaking crests are long, spanning the model domain, whereas at intermediate and high directional spreads (*M*2*c*, *M*2*f*), breaking along-crest length decreases on average as the directional spread increases (Fig. 2.4a-c). Breaking crests are generally associated with positive and negative vorticity forcing ($\nabla \times \mathbf{F_{br}}$) along the identified breaking crest, rather than vorticity forcing being restricted to crest ends

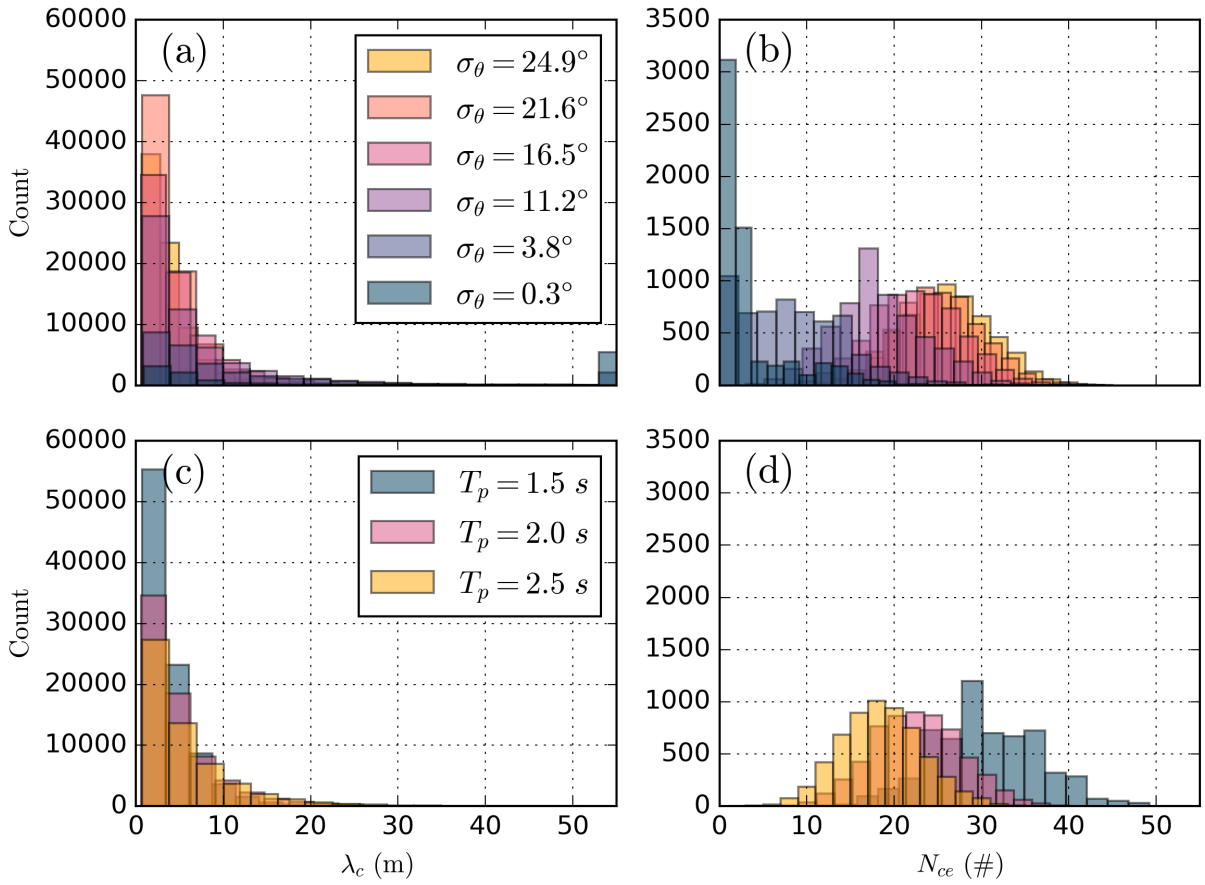

Figure 2.6: Distribution of (a,c) crest length (λ_c) and (b,d) number of crest ends (N_{ce}) for varying directional spreads (σ_θ, colors, legend in a) and peak periods (T_p, colors, legend in c).

(Fig. 2.4d-f). For low directional spread, while some breaking crests are associated with negligible vorticity forcing, other long breaking crests are associated with small-scale variation in $\nabla \times \mathbf{F_{br}}$ along the entire crest (Fig. 2.4d). Snapshots of vorticity show that at low directional spread, eddy activity is minimal, but is increased at intermediate and high directional spread, with intermediate directional spread cases exhibiting larger eddies and stronger eddy pairs (paired red/blue circles in Fig. 2.4h) extending further offshore (Fig. 2.4g-f).

As the peak period increases, the breaking crests in the surf zone lengthen and the

total number of crests decreases at longer periods (Fig. 2.5a-c). While H_s is consistent between runs, breaking crests begin further offshore for shorter peak period as waves steepen, consistent with a small decrease in W_{sz} (Table 2.1). The magnitude of the vorticity forcing across individual crests does vary minimally by peak period with a slight increase with longer peak period (Fig. 2.5d-f). Within the surf zone, the resulting eddy activity is broadly similar for varying peak period (Fig. 2.5g-i).

2.3.3 *Breaking crest statistics*

Individual breaking along-crest length varies within a single model run. At low directional spreads, the distribution of breaking crest lengths is bi-modal, where the majority of waves are short ($\lambda_c < 2.1$ m) or equivalent to the model alongshore domain length (Fig. 2.6a). At higher directional spreads, the distribution of breaking crest lengths is right skewed with the highest frequency at very short lengths and decreasing frequency at longer lengths (Fig. 2.6a). The average modeled crest length decreases with increasing directional spread, ranging from 27.5 m for nearly unidirectional waves to 3.8 m for the largest spreads (Fig. 2.7a). The median modeled crest length also decreases with a similar trend from 13 m for nearly unidirectional waves to 2.8 m at the largest spread.

Modeled mean crest length was nearly stationary through time with a 5% average difference between the first and second 10-minute windows analyzed over all wave conditions. The overall relationship between mean crest length and directional spread is similar between the laboratory (*Baker et al.*, 2023b) and model estimates (Fig. 2.7a). For wave conditions with large directional spreads, the mean crest length estimated from the model are 0.4 m lower than laboratory observations, whereas for the lowest directional spreads, the modeled mean crest length is nearly 27.5 m, nearly 13 m longer than laboratory observations (Fig. 2.7a). At low directional spreads, the maximum crest length is restricted by the model domain and laboratory basin alongshore length. To assess the impact of the finite laboratory width on crest length estimates the statistics were also

computed within sub-regions of equal alongshore length to the laboratory basin (dotted white regions in Fig. 2.1b). The mean crest length observed within these laboratory sub-regions is consistent with mean crest length across the entire model domain at high directional spreads (within $\sim$ 0.6 m), but at the lowest directional spread, mean crest length decreases to 3.6 m, to within $\sim$2 m of laboratory estimates (blue triangles in Fig. 2.7a).

For varying peak period (T_p), the distribution of breaking crest length is right skewed with the highest frequency at very short lengths ($\lambda_c < 2.6$ m) and decreasing frequency at longer lengths for all periods (Fig. 2.6c). As T_p increases, the frequency of short crests also decreases, resulting in the mean crest length to increase slightly from 3.8 to 5.8 for $T_p = 1.5$ s to 2.5 s (Fig. 2.7d). Mean crest length estimated from $M15d$ ($T_p = 1.5$s) is 3.8 m, while $M2d$ ($T_p = 2$s) has a mean crest length of 5.0 m, and $M25d$ ($T_p = 2.5$s) has a mean length of 5.8 m. Median crest length is similar with 2.8 m, 3.5 m, and 3.9 m for T_p = 1.5 s, 2 s, and 2.5 s respectively. Mean crest length estimated from model simulations with varying wave period also are consist with theory (Fig. 2.7d) (*Longuet-Higgins*, 1956). This is meant to be an approximate comparison, as the theory assumes a single wavelength, whereas in the model, the wavelength is varying across the different frequencies present in the spectrum. In addition, in the model, wavelengths are transforming across a complex bathymetry.

The distribution of the number of crest ends within the surf zone at low directional spreads is right skewed, with a large occurrence of small numbers of crest ends (Fig. 2.6b). As the directional spread increases, the mean of the distribution increases and the shape of the distribution becomes more normally distributed (Fig. 2.6b). Estimating crest end density across both 10-minute time windows shows that crest end density is reasonably stationary through the model runs, with 7% average difference between the two time windows and all wave conditions. We find that, the crest end density increases with increasing directional spread (Fig. 2.7b). At low directional spread, where crests typically span the alongshore domain, the density of crest ends is 0.007 m^{-2} and monotonically

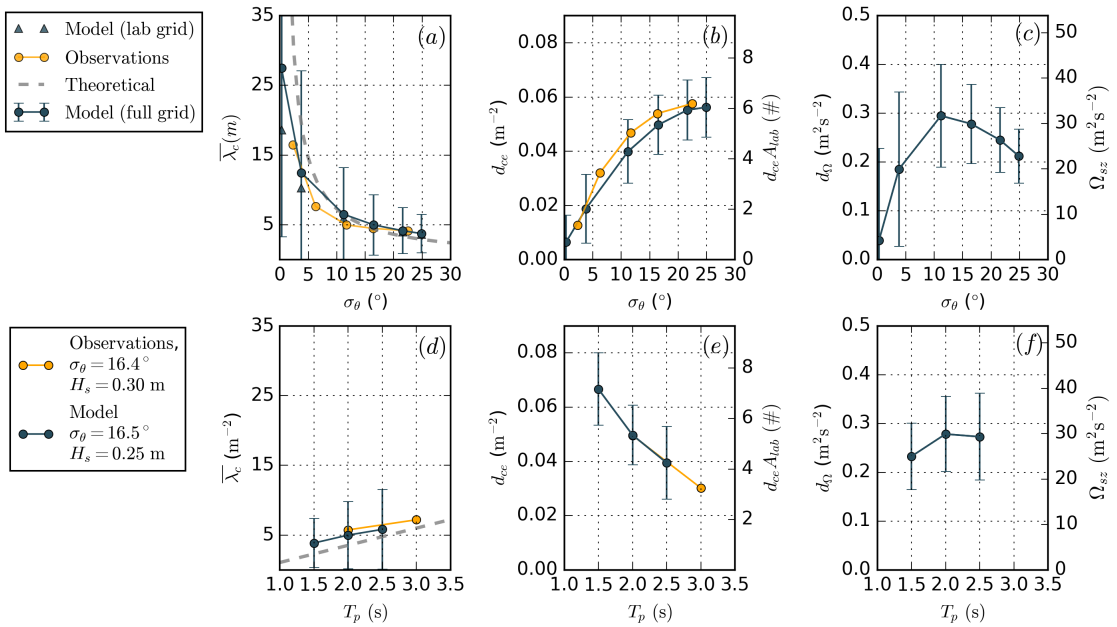

Figure 2.7: The relationship of the (a) mean crest length ($\overline{\lambda_c}$), (b) crest end density ($\overline{d_{ce}}$) and crest ends per laboratory surf zone ($\overline{d_{ce}}A_{lab}$), and (c) vorticity forcing per unit area ($\overline{d_\Omega}$) and vorticity forcing per laboratory surf zone ($\overline{\Omega_{sz}}$) with surf zone directional spread (σ_θ). Quantities estimated from laboratory remote sensing (yellow) and from model simulations (blue) computed over the entire model domain (circles) and over subset laboratory area (triangles). The grey dashed line in (a,d) denotes the theoretical breaking crest length estimated using Eq. 2.1. The influence of peak period (T_p) on (d) mean crest length ($\overline{\lambda_c}$), (e) crest end density ($\overline{d_{ce}}$) and crest ends per laboratory surf zone ($\overline{d_{ce}}A_{lab}$), and (f) vorticity forcing per unit area ($\overline{d_\Omega}$) and vorticity forcing per laboratory surf zone ($\overline{\Omega_{sz}}$). For varying peak period, quantities are estimated from model simulations (blue) and from laboratory remote sensing (yellow). Note that laboratory trials used for comparison to varying peak period are for H_s = 0.3 m waves. Error bars denote the standard deviation.

increases to near 0.06 m^{-2} at the highest directional spread (Fig. 2.7b). These crest end densities are scaled up to the laboratory surf zone area to provide direct comparison with laboratory estimates. The relationship between crest end density and directional spread is consistent between model and laboratory estimates, with nearly 1 crest end in the laboratory surf zone at the lowest spread ($\sigma_\theta = 0.2°$) on average and just above 6 crest ends in the laboratory surf zone at the highest spread (σ_θ = 25.7°) on average.

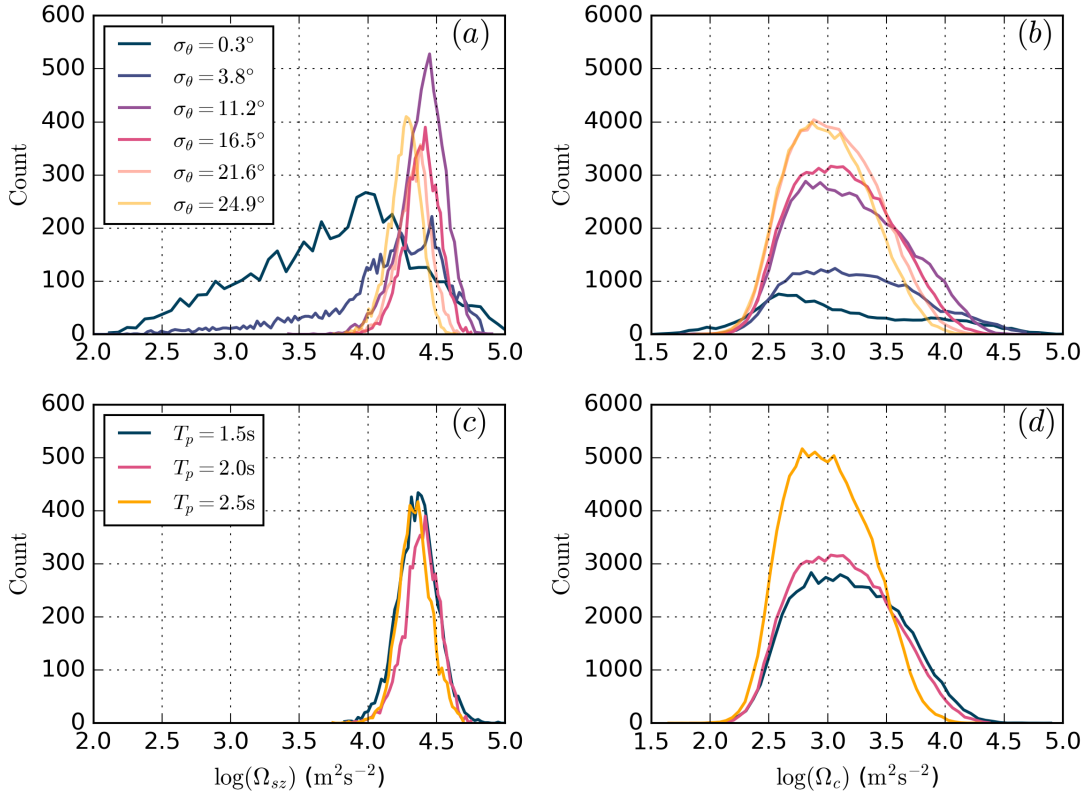

Figure 2.8: (a,c) The log distribution of the vorticity forcing over the surf zone (Ω_{sz}, Eq. 2.10) computed for all model timesteps (dt = 0.2 s over 20 minutes), (b,d) the distribution of total vorticity forcing per crest (Ω_c, Equation 2.9) computed for all crests identified within the model run for varying directional spread (σ_θ, colors, legend in a) and peak period (T_p, colors, legend in c).

As the peak period varies, the distribution of the number of crest ends in the surf zone is similar with a centered normally shaped distribution. The mean number of crest ends increases as the peak period decreases, shifting the distribution but not changing the shape (Fig. 2.6d). Consistent with laboratory results for larger waves ($H_s = 0.3$ m vs. 0.25 m), crest end density is inversely related to peak period (Fig. 2.7e), with crest end density higher for shorter period waves (smaller L_x) and decreased crest end density for longer period waves (larger L_x), which with theory (*Longuet-Higgins*, 1956; *Baker et al.*, 2023b)

2.3.4 *Vorticity forcing*

The modeled vorticity forcing (Eq. 2.8) has a non-monotonic relationship with directional spread, with median vorticity forcing increasing at low directional spreads, peaking at mid-directional spread ($\sim 10^{\circ}$) and decreasing at high directional spreads (Fig. 2.7c). The median vorticity forcing is relatively stationary between the first and second time windows, with an 6% average difference.

As observed visually (Fig. 2.4d-e), the strength of vorticity forcing ($\nabla \times \mathbf{F_{br}}$) varies between individual crests within the surf zone at any given snapshot in time. Therefore, the distribution of the strength of the vorticity forcing over the surf zone at a given time (Ω_{sz}) (Fig. 2.8a) and per individual breaking crest (Ω_c) (Fig. 2.8b) can provide insight into the variation in the generation of vorticity with directional spread. At low directional spreads, despite the occurrence of times when vorticity forcing in the surf zone (Ω_{sz}, Eq. 2.10) is largest across all model runs (upper tail of blue curve in Fig. 2.8a), Ω_{sz} is frequently very small, leading to a small median vorticity forcing (Fig. 2.8a). At larger directional spreads, on average Ω_{sz} is significantly larger than small spreads, with a smaller range of magnitudes in Ω_{sz} than at small directional spreads (Fig. 2.8a). At mid-directional spread, the range in magnitude of Ω_{sz} is smaller than at low directional spreads and similar to large directional spreads. The upper end of the mid-directional spread distribution is greater than the larger directional spreads (upper tail of purple curve in Fig. 2.8a), leading to a larger median vorticity forcing than all other model simulations (Fig. 2.7c).

For Ω_c, low directional spreads also exhibit a larger range in strength of vorticity forcing between all crests, but have a much smaller number of total crests. At high directional spreads, there is a much larger number of total crests, but the range of the strength of vorticity forcing is smaller than lower directional spreads (Fig. 2.8b). For mid-directional spread, the range of the upper tail of the distribution is greater than for higher directional spreads and the upper tail has a greater number of crests, creating a

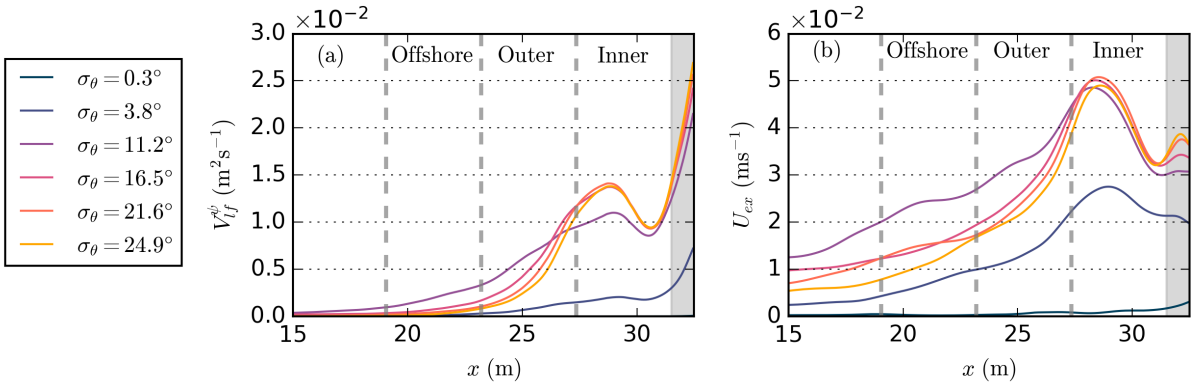

Figure 2.9: Alongshore averaged (a) low frequency rotational power (V_{lf}^{ψ}) and (f) cross-shore exchange velocities (U_{ex}) shown as a function of cross-shore position (x) for varying directional spread (σ_θ colors, legend in a) with shaded region denoting the swash zone excluded from crest identification and analysis. Grey vertical dashed lines denote delineations between the inner surf zone, outer surf zone, and inner shelf regions used in alongshore wavenumber spectra (Fig. 2.12), labeled on figures as inner, outer, and offshore respectively.

skewed distribution (upper tail of purple curve in Fig. 2.8b). The larger upper tail and overall moderate total number of breaking crests also contributes to the largest median vorticity forcing (Fig. 2.7c).

In contrast to directional spread, median Ω_{sz} does not exhibit a strong relationship with peak period. Median Ω_{sz} is smallest at T_p = 1.5 s, but is similar for T_p = 2 s and 2.5 s (Fig. 2.7f). The standard deviation of Ω_{sz} through time (error bars in Fig. 2.7f) are larger for each model run than the variation in median Ω between model runs, suggesting a weak or non-existent relationship between peak period and vorticity forcing. While the distribution of Ω_{sz} is similar between peak periods (Fig. 2.8c), Ω_c varies between peak periods with a greater total number of crests at shorter peak period and a smaller total number of crests at longer peak period (Fig. 2.8d). Despite having a smaller total number of crests, the upper tail of the distribution for T_p = 2 and 2.5 s is larger than for T_p = 1.5 s.

2.3.5 *Surf-zone eddies and cross-shore exchange*

Low frequency rotational power (V_{lf}^{ψ}) and cross-shore exchange velocities (U_{ex}) vary across the surf zone and inner shelf (Fig. 2.9). As a function of cross-shore position, V_{lf}^{ψ} is maximum near the edge of the swash zone, decreases rapidly to onshore edge of the bar, locally peaks at the bar crest, and then decreases to zero offshore for all directional spreads (Fig. 2.9a). Near the bar crest U_{ex} is maximum, but exhibits a local peak within the swash zone, this area is not considered for exchange values and excluded in our crest identification because the swash regions is shallow and intermittently submerged (Fig. 2.9b). While magnitude varies between model simulations, U_{ex} decreases moving offshore from the surf zone edge for all directional spreads.

While the general relationship of V_{lf}^{ψ} and U_{ex} with cross-shore position is similar for different directional spreads, the magnitude varies. Within the inner surf zone, V_{lf}^{ψ} increases from low to mid-directional spreads (σ_θ 0.3 to 16.5°), but higher directional spreads ($\sigma_\theta > 16.5°$) are indistinguishable (Fig. 2.9a). In the outer surf zone, the strength of V_{lf}^{ψ} with directional spread shifts, with mid to high directional spreads beginning to sort backwards with $\sigma_\theta = 11.2°$ having the largest V_{lf}^{ψ} across most of the outer surf (Fig. 2.9a). Directly offshore of the surf, this relationship strengthens and V_{lf}^{ψ} at low and high directional spreads are lower than at mid-directional spread throughout the rest of the model domain (Fig. 2.9a, purple curves greater than other curves). Throughout the cross-shore, U_{ex} exhibits a similar relationship, but with U_{ex} similar at directional spreads above 11.2° in the inner surf and U_{ex} at mid-directional spread dominating all other directional spreads by the edge of the inner surf (Fig. 2.9b).

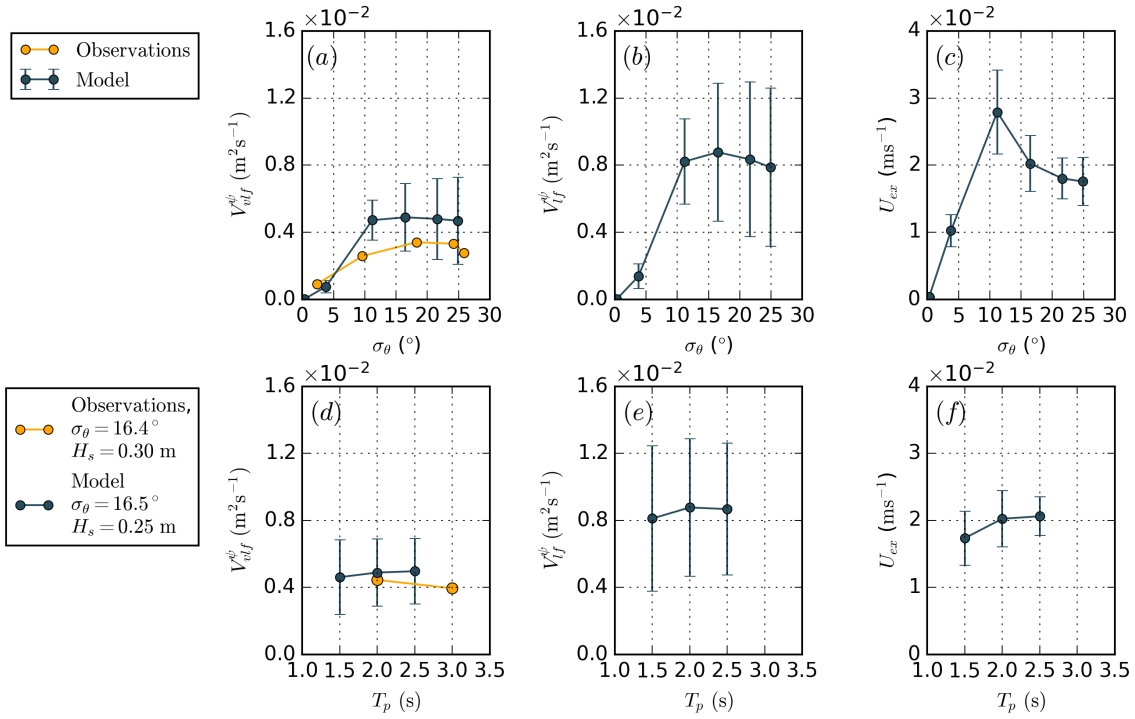

Figure 2.10: The relationship of (a,d) very low frequency rotational power (V^{ψ}_{vlf}) estimated from the model (blue) and laboratory (yellow), (b,e) low frequency rotational power (V^{ψ}_{lf}), and (c,f) cross-shore exchange velocities with (a-c) directional spread and (d-f) peak period. Model estimates of V^{ψ}_{vlf} and V^{ψ}_{lf} are averaged in the along and cross-shore over the surf zone (x = 31.5 - 24.2 m). Laboratory estimates of V^{ψ}_{vlf} are averaged in the alongshore over all instruments at equivalent cross-shore positions and then averaged between cross-shore positions within the surf zone (x = 28.4, 30.7 m). Error bars denote (a,b,d,e) time-averaged alongshore standard deviation of the rotational power and (c,f) standard deviation of time varying cross-shore exchange velocities.

Cross-shore averaged V^{ψ}_{vlf} and V^{ψ}_{lf} increase at low directional spreads and plateau at higher spreads (Fig. 2.10a,b). Laboratory estimates of V^{ψ}_{vlf} are provided for comparison with model estimates. Rotational velocity for the laboratory is estimated from in situ velocity spectra (*Lippmann et al.*, 1999; *Feddersen et al.*, 2011) and so is estimated only for very low frequencies to exclude irrotational infragravity wave energy and minimize contributions from seiche patterns, particularly for the unidirectional waves (*Baker*, 2023).

Though the magnitude of laboratory estimates are ∼50% lower than model estimates of V^{ψ}_{vlf}, laboratory very low frequency motion exhibits a similar plateau at high directional spreads (yellow curve in Fig. 2.10a). Consistent with cross-shore profiles of V^{ψ}_{lf} and U_{ex}, U_{ex} increases at low directional spreads, peaks at mid-directional spreads, and decreases at large directional spreads (Fig. 2.10c). While surf-zone eddy activity and exchange velocities exhibit a clear relationship with directional spread, V^{ψ}_{vlf}, V^{ψ}_{lf}, and U_{ex} do not have a strong relationship with peak period. Both V^{ψ}_{vlf} and V^{ψ}_{lf} increase slightly, ∼7%, with increasing peak period (Fig. 2.10d,e). Additionally, U_{ex} also increases, ∼50% with increasing peak period (Fig. 2.10f).

2.4 Discussion

2.4.1 Influence of directional spread

Crest length and crest end density

As directional spread increases, mean crest length decreases and the crest end density increases. While this trend is consistent with laboratory observations of crest length, as well as linear wave theory, some differences are apparent at lower directional spreads (Fig. 2.7a). As noted before, the finite length of the wave basin and model domain limit the longest crests observed and can account in part for model and laboratory estimates falling below the theory curve. Additionally, nonlinear dynamics, such as wave-current and triad interactions (*Wei et al.*, 2017; *Kirby and Derakhti*, 2019), not accounted for in *Longuet-Higgins* (1956)'s derivation for mean crest length of non-breaking waves may alter the observed dynamics and shift observations away from linear wave theory. Despite some differences, simulated, observed, and theoretical mean crest length is consistent and exhibits a clear inverse relationship with directional spread, with crest end density increasing with increasing directional spread.

Peak in vorticity forcing at mid-directional spread

Although breaking crest length and ends exhibit a monotonic relationship with directional spread, the median vorticity forcing instead peaks at mid-directional spread (Fig. 2.7c). Prior work has shown that the variance of vorticity forcing, $S_{\nabla \times \mathbf{F_{br}}}$, across all alongshore scales increases with increasing directional spread (*O'Dea et al.*, 2021), meaning that integrated across all wavenumbers the total variance of vorticity forcing ($\nabla \times \mathbf{F_{br}}$) increases with increasing directional spread. This estimate of vorticity forcing is not equivalent to Ω_{sz}, but integrated $S_{\nabla \times \mathbf{F_{br}}}(k)$ over all wavenumbers from our simulations (not shown) gives the same relationship with directional spread and peak period where this total variance of vorticity forcing peaks at mid-directional spread and mid-peak period (i.e. the same shapes as Fig. 2.7c,f). This peak at mid-directional spread differs from *O'Dea et al.* (2021) despite encompassing a similar range of directional spread (0-25° vs. 0-20°), a similar offshore wave regime ($kh \sim 1.1$ vs. $kh \sim 0.8$), and wave linearity ($Ur \sim 7$ vs. 11). The bathymetry in our simulations differ from previous studies on planar (*Johnson and Pattiaratchi*, 2006; *Kennedy*, 2003; *Suanda and Feddersen*, 2015) and terraced beaches (*Spydell and Feddersen*, 2009; *Feddersen*, 2014) with no apparent bar or trough feature in the cross-shore and a significantly shallower beach slope (mean slope ∼0.02 (*Spydell and Feddersen*, 2009; *O'Dea et al.*, 2021)). The combination of a steeper beach and presence of a bar/trough profile likely lead to these differences in vorticity generation; however, further investigation of vorticity generation of individual crests and across the surf zone over a range of beach slopes and different bar/trough geometries is needed to fully understand why the relationship of vorticity forcing and directional spread differs for a shallow planar and a steep barred beach.

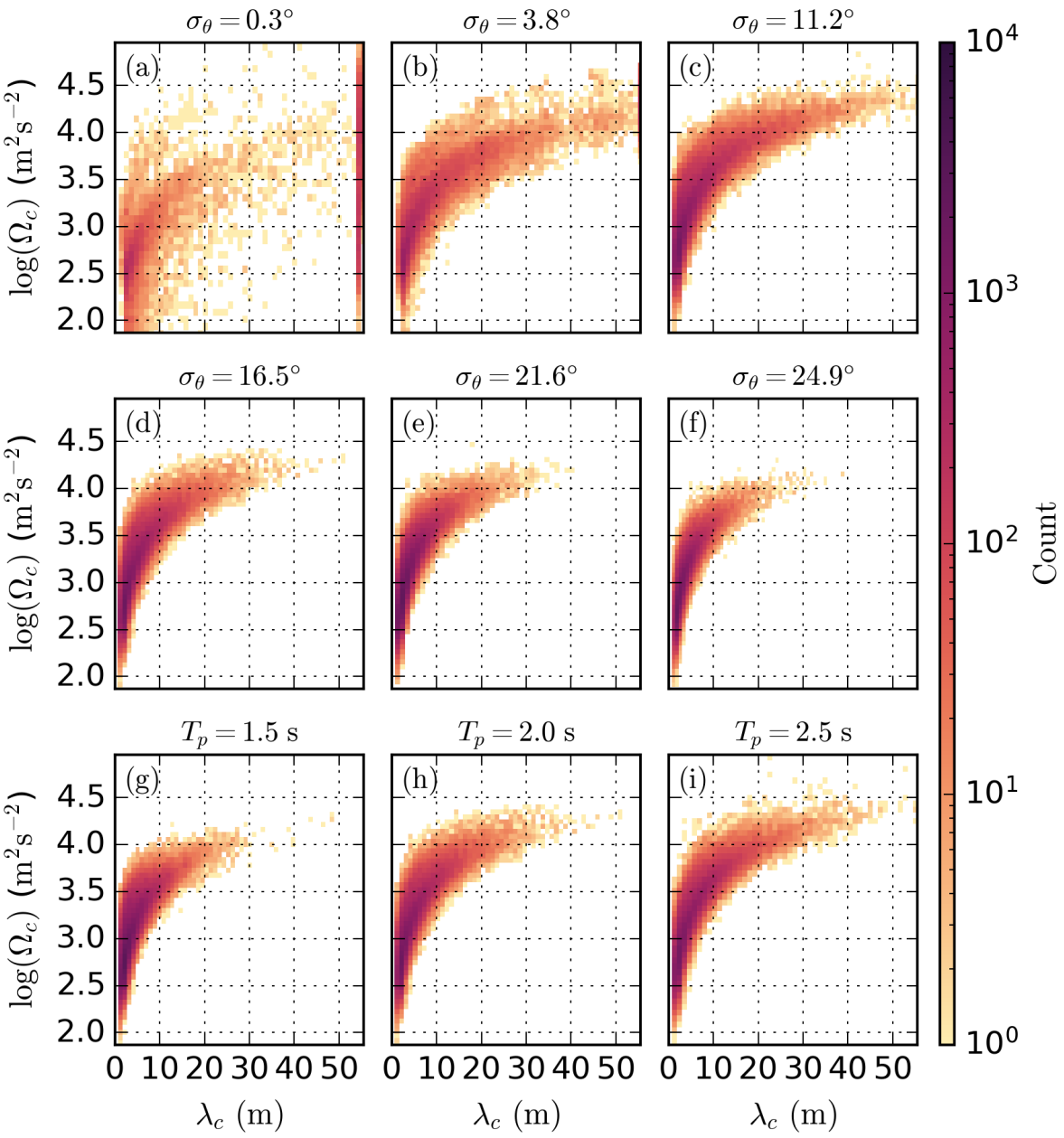

Figure 2.11: Two-dimensional frequency distribution of crest length (λ_c) vs log vorticity forcing per crest ($\log(\Omega_c)$) for (a-f) varying directional spread (σ_θ) and (g-i) peak period (T_p). Note high count of 55 m length crests in (a).

Vorticity forcing varies between crests and so we investigate the differences in Ω_c, vorticity forcing per crest, to understand why our simulations show a peak in vorticity forcing at mid-directional spreads. The combination of a non-monotonic relationship between Ω_{sz} and directional spread and a monotonic relationship between crest end density and directional spread suggests that Ω_c may exhibit a nonlinear relationship with breaker length. This means that more breaking crests does not necessarily imply greater vorticity forcing. The distribution of Ω_c shows that the magnitude of the vorticity generation per crest by individual breaking crests can vary nearly 4 orders of magnitude at the lowest directional spreads with decreasing range at higher directional spreads (Fig. 2.8b, values range from order 10 to 10^5). Additionally, the shape of the Ω_c distribution varies with directional spread (Fig. 2.8b). In particular, the upper tail of the distribution is larger for mid-directional spread than higher directional spreads (purple curve in Fig. 2.8b). The larger tail in the distribution of Ω_c can be better understood through exploring the relationship between crest length, λ_c, and vorticity forcing per crest, Ω_c.

We see a positive relationship between Ω_c and λ_c (Fig. 2.11), as well as a shift in the distribution of λ_c with directional spread (Fig. 2.6b). The combination of these two relationships leads to larger median vorticity forcing across the surf zone (Ω_{sz}) at mid-directional spread ($\sigma_\theta = 11.2^\circ$) and decreasing Ω_{sz} at higher spreads (Fig. 2.7c). From mid to larger directional spreads ($\sigma_\theta > 16.5^\circ$), a strong positive relationship between λ_c and Ω_c is observed meaning that for longer crests the generation of vorticity (Ω_c) is generally greater (Fig. 2.11c-f). However, as directional spread increases the expected λ_c decreases (Fig. 2.7a) and thus the upper distribution of Ω_c is decreased since the maximum length of breaking crests, as well as the frequency of long breaking crests decreases at high spreads. This decrease in frequency of longer breaking crests leads to a reduction in the range of Ω_c for a given λ_c for increasing directional spread, leading to smaller maximum Ω_c at higher spreads (compare vertical extent of distributions in Fig. 2.11c-f). In contrast, for unidirectional waves ($\sigma_\theta = 0.2^\circ$), the relationship between λ_c and Ω_c is weak, with the magnitude of Ω_c encompassing a wide range across all crest lengths (Fig. 2.11a), showing

that both small and large crests contribute a large range of vorticity forcing.

The relationship between crest length and vorticity forcing, while informative for understanding these model simulations, requires further investigation for generalizability across lab to field scale and simulations to observations of field wave conditions. Here, we compute $\mathbf{F_{br}}$ (Eq. 2.5, 2.6) consistent with prior modeling studies (*Feddersen*, 2014; *O'Dea et al.*, 2021; *Kumar and Feddersen*, 2017a,b). Our approaches for estimating Ω_{sz} and Ω_c were chosen to minimize extraneous postprocessing of model fields that could introduce biases. For example, small-scale variations in the strength of $\mathbf{F_{br}}$ and $\nabla \times \mathbf{F_{sz}}$ exist across individual crests in our simulations (Fig. 2.4d-f, 2.5d-f). The importance of this small-scale spatial variability is still unknown, as sufficiently small scale forcing may be subject to a direct energy cascade or dissipated through numerical diffusion rather than contribute to an inverse energy cascade. However, we chose not to spatially filter or alter $\nabla \times \mathbf{F_{br}}$ fields since initial tests showed that spatial filtering lowered the magnitude of Ω_{sz} and Ω_c. Still, with filtering, their relationship with directional spread remained the same.

Various choices exist for estimating or simulating energy dissipation from wave breaking. In addition to using a breaking induced eddy viscosity following *Kennedy et al.* (2000), phase-resolved models also allow for simulating wave breaking through shock capturing (*Choi et al.*, 2018b) and hydraulic jump (*Smit et al.*, 2013) methods. Additionally, smooth particle hydrodynamic models allow for simulation of wave breaking through wave overturning and creation of vortex loops (*Kirby and Derakhti*, 2019). From observations, a wave roller dissipation model (*Duncan, J H*, 1981) has been used to estimate wave dissipation from observations (*Clark et al.*, 2012; *Carini et al.*, 2015). Comparison of $\nabla \times \mathbf{F_{br}}$ across individual crests using these different wave breaking dissipation models is needed to better characterize vorticity forcing. In particular, comparison of $\nabla \times \mathbf{F_{br}}$ from model simulations and observations would provide valuable context for characterizing the important physical wave breaking dynamics that contribute to coherent surf zone vorticity, as opposed to impacts of parameterization choices.

Low frequency eddies and cross-shore exchange

The peak in vorticity forcing at intermediate directional spread is consistent with a peak in U_{ex}, which may suggest that the resulting surf zone exchange is a direct result of the trend in forcing. However, within the surf zone, low frequency rotational motion does not peak at mid-directional spread as the vorticity forcing does (Fig. 2.10a,b). This mismatch between forcing and large scale eddy motions in the surf zone suggest that vorticity generated from breaking waves is not transformed uniformly from forcing to resulting eddy motion for all directional spreads. Mismatch between forcing and low frequency motions may indicate that the small-scale variability of $\nabla \times \mathbf{F_{br}}$ over individual crests that contributes to a larger Ω_{sz} at mid-directional spread is not transferring momentum to rotational flows, allowing for high spreads to have a similar V_{lf}^{ψ} despite smaller Ω_{sz}. From the laboratory data, *Baker et al.* (2023a) found evidence for an inverse energy cascade at high directional spreads, but not at intermediate and lower directional spreads. Laboratory results suggest that model simulations may also exhibit a variation in consistency with an inverse energy cascade, which may lead to more energetic large-scale eddies in the surf zone for larger spreads. Alongshore wavenumber spectra of rotational motions provide insight into the transfer of energy across scales and the development of large scale eddies and ejections driving cross-shore exchange.

Alongshore wavenumber spectra of vorticity show similar relationships of energy across scales and with directional spread as prior findings. Within the inner surf zone, energy at small scales (large k_y) sorts by directional spread, consistent with prior field-scale modeling (*Spydell and Feddersen*, 2009; *Baker et al.*, 2021; *O'Dea et al.*, 2021); however, the drop in variance at small scales between large and small directional spreads is larger than prior findings (i.e. $\sim$3 order magnitude drop between large σ_θ and unidirectional waves at k_y larger than grey dashed line in Fig. 2.12a). Additionally, consistent with *Baker et al.* (2021, 2023a), vorticity variance decreases across all scales moving offshore (compare magnitude across Fig. 2.12a-c); however, our model simulations show a greater

drop in vorticity variance across scales for large directional spreads. In prior modeling studies (*Spydell and Feddersen*, 2009; *Baker et al.*, 2021; *O'Dea et al.*, 2021), large directional spreads have the greatest vorticity variance at small scales (large k_y) across the surf zone and offshore. Vorticity variance for the highest directional spreads ($\sigma_\theta = 21.6, 24.9^\circ$) drops below mid-directional spreads ($\sigma_\theta = 11.2, 16.5^\circ$) offshore (Fig. 2.12c). While the directional spreads simulated here are greater than the directional spreads in some simulations (*Spydell and Feddersen*, 2009; *O'Dea et al.*, 2021), simulations in *Baker et al.* (2021) extend past the highest spreads here, suggesting directional spread range does not explain differences in transformation of vorticity variance across the surf zone at high spreads. As large-scale eddies have been shown to be limited by surf-zone width and large-scale mean circulation (*Elgar et al.*, 2023), differences in bathymetry from prior studies (e.g. bar/trough system) may impact the development of large-scale eddies. In particular, bar/trough geometry is constant between model simulations, but scales of breaking crests vary with directional spread which may be important to differences in the inverse energy cascade and development of large-scale eddies seen in the laboratory data (*Baker et al.*, 2023a). Analysis of third order structure functions from laboratory data show that evidence of an inverse energy cascade varies with directional spread (*Baker et al.*, 2023a), but further investigation of these dynamics in model simulations is needed.

In addition to possible differences in energy transfers between scales, the scales of the vorticity forcing itself may also contribute to the fact that V_{lf}^{ψ} plateaus whereas Ω_{sz} peaks at mid-directional spread. Vorticity forcing ($\nabla \times \mathbf{F_{br}}$) within individual crests has strong small-scale spatial variability (Fig. 2.4d-f, 2.5d-f). As we have defined Ω_c, all scales of variability of $\nabla \times \mathbf{F_{br}}$ contribute to estimating the vorticity forcing; however, it is unknown what scale of vorticity forcing is the most important to the development of large scale eddies. Very small scale variations in $\nabla \times \mathbf{F_{br}}$ are likely dissipated via a forward turbulence cascade or numerical diffusion, but some variations in $\nabla \times \mathbf{F_{br}}$ that are small in a given crest may be persistent through time as a breaking crest propagates through the surf zone leading to the development of larger scale vorticity that is subject to an inverse

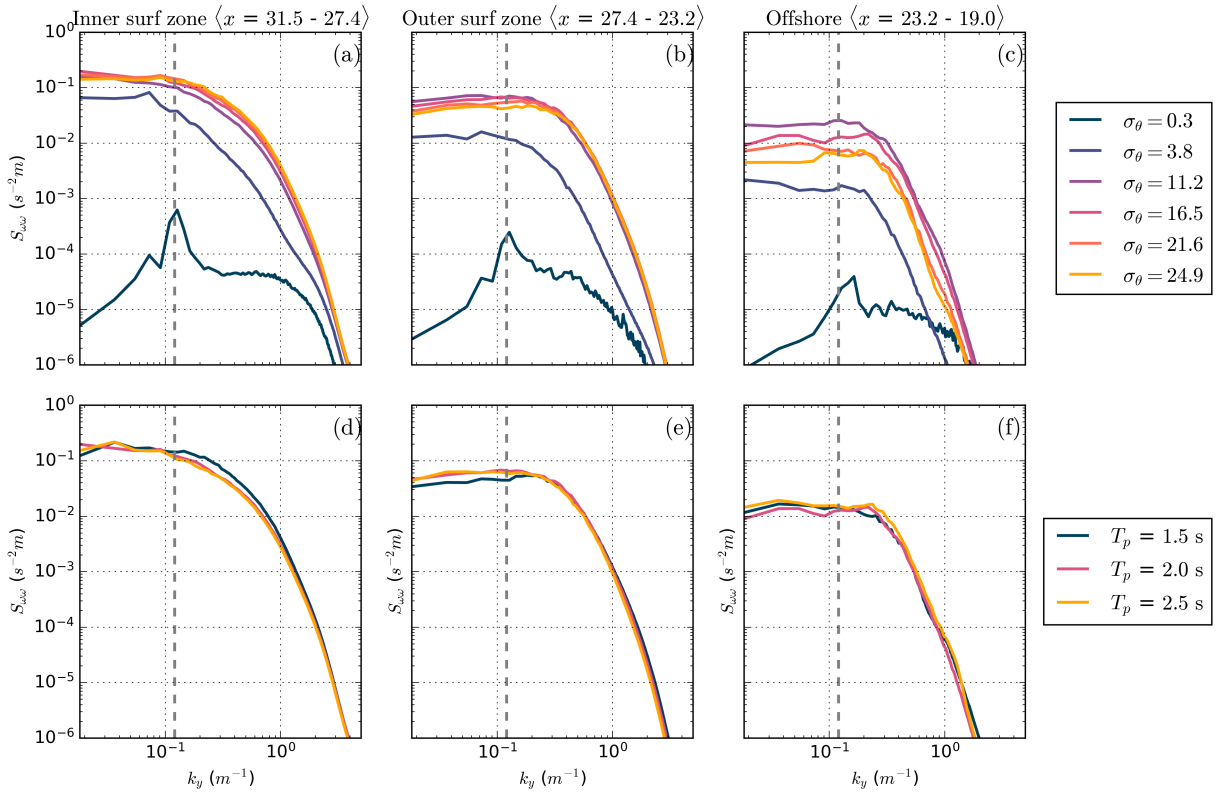

Figure 2.12: Cross-shore and time averaged alongshore wavenumber spectra of vorticity ($\nabla \times \mathbf{u_{rot}}$) in the (a,d) inner surf zone, (b,e) outer surf zone, and just offshore of the surf zone (c,f) for varying (a-c) directional spread (σ_θ colors, legend in a) and (d-f) peak period (colors, legend in d). Dashed line denotes $1/W_{sz}$.

energy cascade. At low directional spread, long breaking crests can contribute large Ω_c (Fig. 2.4d,2.8b), but these breaking crests do not appear to significantly contribute to the development of large-scale low frequency eddies, as V_{lf}^{ψ} and V_{vlf}^{ψ} are near zero for $\sigma_\theta = 0.2°$. These small scale vorticity features along the crest may not be coherent spatially or through time, and thus may be dissipated quickly rather than contribute to an inverse energy cascade, compared to theoretical coherent eddies at translating crest ends that form a vortex sheet (*Peregrine*, 1998).

2.4.2 *Influence of peak period*

In addition to directional spread, changes in other wave-field characteristics may influence the strength of vorticity forcing and the resulting eddy dynamics. Variation of both peak period and significant wave height on crest length and number of crest ends has been tested with laboratory observations (*Baker et al.*, 2023b). *Baker et al.* (2023b) found that crest length and number of crest ends depended on peak period, with longer period waves having short mean crest length and less total number of crest ends. Although wave height dependence was not investigated here, *Baker et al.* (2023b) found that increasing wave height resulted in negligible change in the crest length and a weak increase in the number of crest ends as the surf zone widens for the small range of wave heights tested. Consistent with these prior findings, we find that the mean crest length has a weak dependence on peak period, with shorter period conditions resulting in shorter crests and longer period conditions resulting in longer crests, consistent with expectations from theory (*Longuet-Higgins* (1956); *Baker et al.* (2023b), Eq. 2.1). Theoretical estimates of expected mean crest lengths for varying peak period are consistently below model estimates but are within 1.5 m exhibit the same increasing trend with increasing peak period (Fig. 2.7d).

Consistent with mean crest length increasing with longer peak periods, modeled crest end density is inversely related to peak period. This influence of peak period on crest end density is consistent with prior findings (*Baker et al.*, 2023b); however, this study examines the relationship for a different set of wave periods with a longer alongshore domain. While the relationship between crest end density and peak period is strong, the relationship with Ω_{sz} is fairly weak with a slight peak at mid-peak period exhibiting the highest Ω_{sz}. Similar to increasing directional spread, decreasing peak period results in a reduction of the maximum Ω_c and λ_c. Additionally the range in Ω_c for a given λ_c increases for increasing peak period and results in $T_p = 2.5$ s having a weaker relationship between Ω_c and λ_c, similar to low directional spreads. This results in a slight peak at

mid-peak period, similar to the peak at mid-directional spread, through the magnitude of these variations are minimal (Fig. 2.7c,f).

While the mean Ω_c increases with increasing T_p since crest length increases with period (Eq. 2.1), the decrease in the total number of crests in the surf zone for longer peak periods may also contribute to the relationship between Ω_{sz} and T_p. For longer peak period conditions, breaking crests are longer on average, which would lead to a smaller number of crests able to fit within the same area compared to shorter crests. Additionally, as the peak period increases, the wave steepness decreases, resulting in wave breaking occurring slightly further onshore relative to conditions with a shorter peak period, resulting in a narrower surf zone (Table 2.1) and limiting the number of breaking crests in the cross-shore. This narrowing of the surf zone is minimal with W_{sz} = 8.75 m for T_p = 1.5 s and W_{sz} = 8.1 for T_p = 2.5 s, which is within the average variation of surf zone width in time over the model simulations. In theory, this reduction could act to limit the total number of breaking crests that fit within the surf zone if breaking is primarily wave steepness induced, rather than simply limited by a wave height to depth ratio (*Raubenheimer et al.*, 1996). The weak relationship between vorticity forcing and peak period results in a similarly weak relationship for low frequency rotational motion and cross-shore exchange with peak period. Similarly, the magnitude of energy associated with surf-zone eddies across spatial scales is consistent between peak periods (Fig. 2.12d-f). The overall magnitude of rotational energy does decrease from the inner surf zone moving offshore, consistent with prior modeling studies (*Baker et al.*, 2021; *O'Dea et al.*, 2021) and in situ observations of laboratory data (*Baker et al.*, 2023a), but exhibits no variation between peak periods.

2.4.3 Role of barred bathymetry and other considerations for future work

While not explicitly explored in this study, the presence of barred bathymetry likely plays an important role in eddy evolution and cross-shore exchange. Most previous

studies exploring the relationship between directional spread and eddy processes were over planar (*Johnson and Pattiaratchi*, 2006; *Kennedy*, 2003; *Suanda and Feddersen*, 2015) or terraced beaches (*Spydell and Feddersen*, 2009; *Feddersen*, 2014). *Bühler and Jacobson* (2001) has shown that for an idealized vortex dipole pair in the surf zone, the separation between each vortex decreases and mutual advection intensifies moving into deeper water, making the vortex propagation up-slope more difficult as separation increases and advection slows. On a barred beach, it is hypothesized that vortex pairs would move down-slope into the through easily, but advection out of the trough would be limited (*Bühler and Jacobson*, 2001). The strength of vortex propagation not only relies on the water depth, but also the circulation of each vortex (*Bühler and Jacobson*, 2001). Circulation strength varies with the strength of vorticity over the vortex, as well as the size of the vortex. Vorticity variance across scales varies with directional spread (Fig. 2.12a-c) indicating variation in dominant eddy sizes with directional spread is expected, which would influence the circulation of individual vortices. Further investigation of eddy size, circulation strength, and bar/trough geometry for varying directional spread may help explain the plateau of low frequency rotational motion in the surf zone and peak of cross-shore exchange velocities at the surf-zone edge at mid-directional spread. Many beaches have seasonal bar/trough bathymetry, so better understanding eddy processes and exchange on these types of beaches is important. Further investigation to quantify individual vortex size and circulation strength and bar/trough geometry may provide further insight into the influence of barred bathymetry.

2.5 Summary and conclusions

This work quantified breaking crest characteristics, vorticity forcing, and resulting low frequency eddies and cross-shore exchange under varying wave conditions with a wave-resolving Boussinesq model of a laboratory-scale barred beach. Modeled wave conditions spanned the conditions in a series of previous laboratory experiments (*Baker et al.*, 2023b,a). The model simulations were evaluated with in situ and remotely sensed observations of

sea surface elevation and velocity. Model wave breaking induced eddy viscosity was used to identify actively breaking waves and estimate crest characteristics. We found that the mean crest length decreases and the crest end density (number of crest ends per unit area) increases with increasing directional spread, consistent with laboratory estimates and wave theory. For the same directional spread, longer peak period results in longer mean crest length and decreased crest end density. While the number of crest ends increases with spread, the vorticity forcing associated with breaking crests across the surf zone peaks at intermediate directional spreads. The peak in vorticity forcing at mid-directional spread is consistent with the presence of longer mean crest length than higher directional spreads and a positive relationship between crest length and vorticity forcing per crest for mid to high directional spreads. For the same directional spread, peak period has minimal influence on vorticity forcing as an increase in total number of crests may be offset by a decrease in vorticity forcing per crest.

Similar to the peak in vorticity forcing at intermediate directional spreads, there is a peak in low and very low frequency energy and cross-shore exchange at mid-directional spread at the surf zone edge. However, low frequency energy and cross-shore exchange vary as a function of cross-shore position. Consistent with laboratory observations, very low frequency energy in the surf zone increases at low directional spread and plateaus or mildly increases at large directional spreads. The increase in low frequency eddies in the surf zone with directional spread suggests differences in eddy evolution or dissipation of vorticity forcing at small scales. Future work towards better understanding the transfer of vorticity forcing to larger scales via an inverse energy cascade would contribute to diagnosing the relevant features in breaking crest variability for low frequency eddies and cross-shore exchange. Additionally, further work to directly compare barred versus planar bathymetry would improve our understanding of the role of changing bathymetric profiles on wave-breaking forcing mechanisms and cross-shore exchange exchange.

Chapter 3

AN EDDY PERSPECTIVE OF THE SURF ZONE

How do coherent eddies vary in the cross-shore and for varying wave conditions?

3.1 Introduction

Large-scale horizontal rotational motions play an important role in dispersing tracers within the surf zone (*Hally-Rosendahl et al.*, 2014) and driving cross-shore exchange of tracers (*Kumar and Feddersen*, 2017c; *Grimes et al.*, 2020), including pollutants and nutrients crucial to nearshore water quality (*Halpern et al.*, 2008; *Boehm et al.*, 2017) and larval transport and recruitment (*Morgan et al.*, 2017; *Moulton et al.*, 2023). These horizontal motions can be generated from wave breaking on irregular bathymetry (*MacMahan et al.*, 2006, 2010b), shear instabilities in alongshore currents (*Bowen and Holman*, 1989; *Oltman-Shay et al.*, 1989; *Feddersen*, 2014; *Özkan Haller and Kirby*, 1999), and directionally spread short-crested wave breaking (*Peregrine*, 1998; *Spydell and Feddersen*, 2009; *Clark et al.*, 2012; *Hally-Rosendahl and Feddersen*, 2016). On alongshore-uniform bathymetry during short-crested wave breaking, along-crest irregularities in the strength of wave breaking, particularly at the ends of breaking waves (*Peregrine*, 1998), generate small-scale vertical vorticity in the surf zone (*Clark et al.*, 2012; *Kirby and Derakhti*, 2019; *Wei et al.*, 2017). Energy associated with this small-scale vorticity can be nonlinearly transferred to larger scale rotational motions, consistent with a forced two-dimensional turbulence system (*Elgar and Raubenheimer*, 2020; *Elgar et al.*, 2023; *Baker et al.*, 2023a; *Spydell and Feddersen*, 2009; *Feddersen*, 2014). These larger rotational motions can be coherent horizontal motions that enhance cross-shore exchange through the development of offshore ejection of material

via transient rip currents (*Johnson and Pattiaratchi*, 2006; *Clark et al.*, 2010; *Feddersen et al.*, 2011; *Hally-Rosendahl and Feddersen*, 2016; *Suanda and Feddersen*, 2015; *Kumar and Feddersen*, 2017a,b; *Grimes et al.*, 2020; *Grimes and Feddersen*, 2021; *Choi and Roh*, 2021).

Surf-zone vertical vorticity generation, evolution, and cross-shore exchange under varying directional spread has been studied in laboratory observations (*Baker et al.*, 2023b,a) and through numerical simulations (*Suanda et al.*, 2016; *O'Dea et al.*, 2021; *Nuss, Emma et al.*, b). Prior work has shown that breaking crest lengths decrease and the number of crest ends within the surf zone increases with increasing directional spread of the wave field (*Baker et al.*, 2023b; *Nuss, Emma et al.*, b). However, numerical simulations have shown that a greater number of breaking waves in the surf zone is not necessarily associated with greater vorticity generation or cross-shore exchange for barred beaches (*Nuss, Emma et al.*, b), while planar beaches may exhibit a monotonic relationship (*Suanda and Feddersen*, 2015). Vorticity is generated at small scales during wave breaking, but surf-zone eddies that drive cross-shore exchange occur at larger scales and it has been found that their size may be influenced by the width of the surf zone and mean currents (*Elgar et al.*, 2023). The transfer of energy from small to large-scale eddies can be consistent with a forced two-dimensional turbulence system (*Spydell and Feddersen*, 2009; *Feddersen*, 2014; *Elgar and Raubenheimer*, 2020; *Elgar et al.*, 2023), however, this consistency is not observed across all directional spreads in laboratory experiments (*Baker et al.*, 2023a). This discrepancy highlights gaps in our understanding of the transfer of energy between scales, the nature of eddy-eddy interactions, the life cycle of surf-zone eddies, and the development of transient rip currents in the surf zone for varying wave conditions.

In the surf zone, eddy-driven transient rip current exchange has been investigated through Eulerian perspectives quantifying cross-shore exchange velocities (*Suanda and Feddersen*, 2015; *Kumar and Feddersen*, 2017a,b; *O'Dea et al.*, 2021; *Nuss, Emma et al.*, b), dye exchange (*Hally-Rosendahl et al.*, 2014; *Hally-Rosendahl and Feddersen*, 2016; *Grimes et al.*, 2019, 2020; *Grimes and Feddersen*, 2021) and drifter tracks (*Johnson and Pattiaratchi*, 2006; *Spydell et al.*, 2009). Theories for vorticity generation (*Peregrine*, 1998) and propagation of

coherent vortices on sloping barred bathymetry (*Bühler and Jacobson*, 2001) have provided insights for individual eddy dynamics. Individual vortex focused investigation has been expanded to vorticity maxima and minima identification and tracking for surf-zone currents on variable bathymetry to characterize the vortex dipole dynamics that lead to bathymetric rip current circulation (*Geiman and Kirby*, 2013). Recently, time-averaged surf-zone vortices were identified on variable bathymetry for a range of wave conditions and tidal stages and characteristics of the size and strength of the vortices were estimated assuming Rankine vortex dynamics (*Bondehagen et al.*, 2024). Identification of individual vortices for bathymetric rip currents provides a new perspective that has not been applied to transient rip currents. In this paper we take an eddy focused perspective of surf-zone vorticity and transient rip currents by characterizing distinct, coherent vortices, which we will refer to in this paper as eddies.

Identification of individual vortices or eddies has been used in geostrophic turbulence to characterize vortex interactions and energy cascade (*McWilliams et al.*, 1999) at the mesoscale. A similar vortex identification perspective of the surf zone may provide a valuable perspective of the turbulent eddy processes and the transport of material via cross-shore exchange. At much larger scales, coherent mesoscale eddies transport tracers trapped in their cores across the ocean and can influence local biogeochemistry through varying vertical fluxes of nutrients available for phytoplankton growth (*Chelton et al.*, 2011a; *Travis and Qiu*, 2020). The increasing availability of high resolution satellite altimeter data of sea surface elevation globally has allowed for the development of mesoscale eddy identification and tracking algorithms (*Schlax, Michael G and Chelton, Dudley B*, 2016; *Mason et al.*, 2014). These algorithms have allowed for quantifying eddy translation speed, direction, and non-linearity, changing our understanding of large-scale ocean dynamics and providing new perspectives of their impact on bio-geochemical ocean processes (*Chelton et al.*, 2011b; *Mason et al.*, 2017; *Pegliasco et al.*, 2015; *Travis and Qiu*, 2020; *Pegliasco et al.*, 2021).

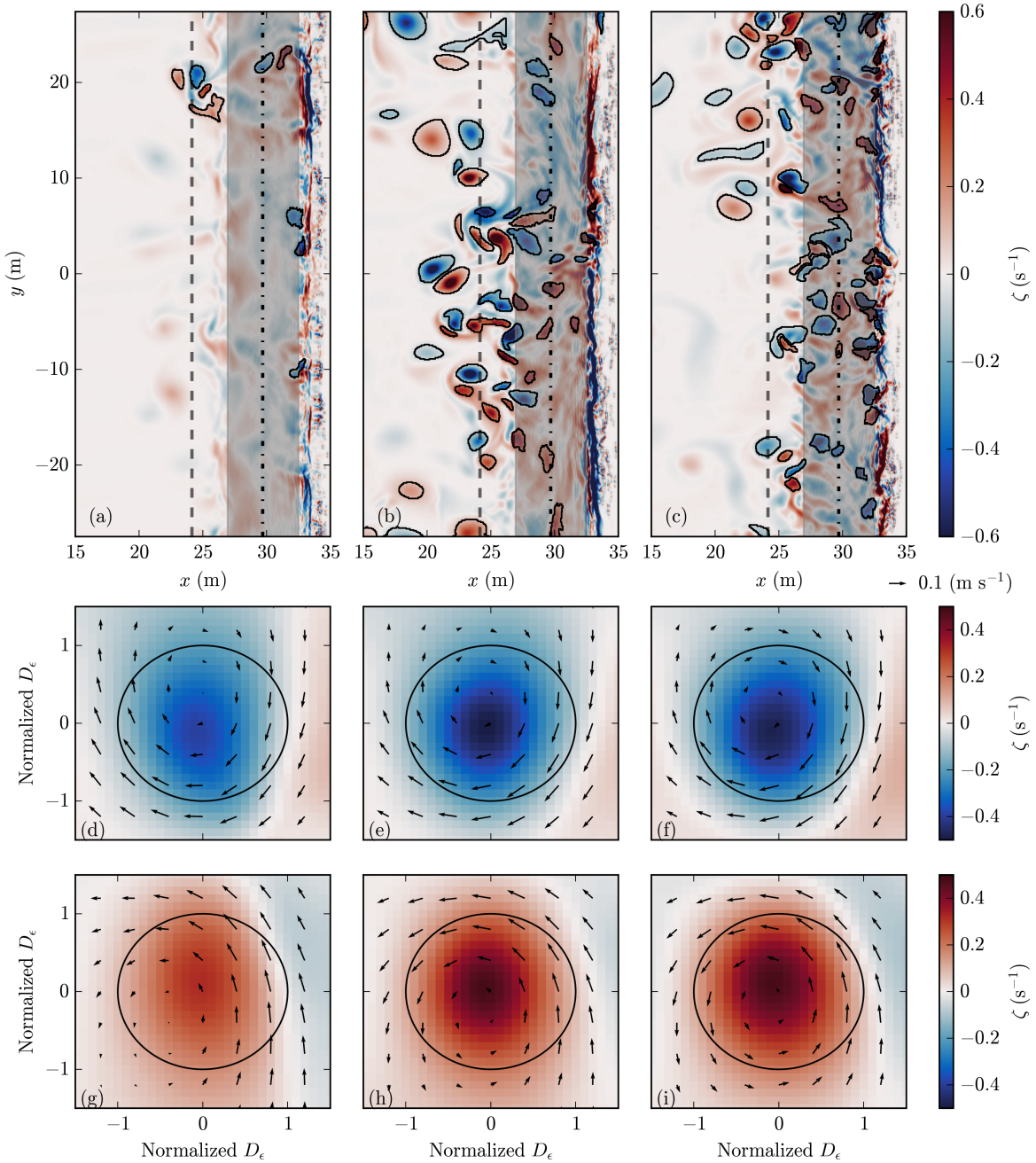

Figure 3.1: (a-c) Snapshots of simulated vorticity (ζ) and overlaid boundaries (black circles) of identified eddies and eddy composites of vorticity (colorbar) and rotational velocity (arrows) for (d-f) positively signed and (g-i) negatively signed eddies for (a,d,g) low directional spread ($\sigma_\theta = 3.8°$), (b,e,h) intermediate directional spread ($\sigma_\theta = 11.2°$), and (c,f,i) high directional spread ($\sigma_\theta = 24.9°$). Shaded regions in (a-c) denote the surf zone, dash-dotted line denotes halfway across the surf zone or the transition between in the inner and outer surf zone, and the dashed line denotes the edge of the offshore region (half a surf-zone width from the edge of the surf zone)

In this paper, we modify mesoscale eddy identification algorithms to identify surf-zone eddies from simulated vorticity (Fig. 3.1. We show that statistics from an eddy-tracking perspective have consistency with prior findings of Eulerian surf-zone vorticity, but provides a unique way of understanding these dynamics on an individual eddy and rip current event scale. The numerical simulations used and the identification and characterization method descriptions are presented (Section 3.2). Performance of eddy identification, distributions of eddy characteristics, and cross-shore variation in eddy characteristics such as eddy counts, size, circulation, and non-linearity are presented for three wave conditions with increasing directional spread (Section 3.3). These relationships and the consistency with prior results using traditional methods are discussed and this eddy-focused perspective is linked to classic Eulerian approaches through relating eddy characteristics to cross-shore velocities and exchange metrics (Section 3.4), Lastly, a summary and implications for future analysis is presented (Section 3.5).

3.2 Methods

3.2.1 Numerical modeling

We use a subset of numerical simulations from *Nuss, Emma et al.* (b), which simulate directionally spread irregular waves on a laboratory-scale barred beach using FUNWAVE-TVD, a depth-averaged wave-resolved Boussinesq model (*Shi et al.*, 2012). The FUNWAVE-TVD simulations were configured to simulate wave conditions observed during laboratory experiments (*Baker et al.*, 2023b) and model performance was evaluated with remote sensing and in situ data from laboratory experiments (*Nuss, Emma et al.*, b). The model domain is 62 m in the cross-shore (dx = 0.05 m) and 55 m in the alongshore (dy = 0.1 m). The model bathymetry is alongshore uniform, with a bar ($x \simeq 27.5$ m) and trough ($x \simeq 28$–31 m). Simulations were run for 25 minutes for waves with wave forcing of 0.25 m significant wave height (H_s) with a peak period (T_p) of 2 s and directional spreads (σ_θ) ranging from $\sim 0 - 25^\circ$. In this paper we use 3 simulations a low ($\sim 3^\circ$),

intermediate($\sim 11^\circ$), and high ($\sim 25^\circ$) directional spreads for eddy identification and characterization of eddy properties for varying directional spread. These simulations will be referred to as the low, intermediate,and high spread simulations throughout the paper.

3.2.2 *Eddy Identification*

Eddy identification is performed on simulated fields of vorticity from the low, intermediate,and high spread simulations (Table 2.1). Vorticity is computed from the rotational component of the simulated velocity field via a Helmholtz decomposition of the velocity into irrotational and rotational components to remove vorticity associated with oblique wave crests (*e.g.*, *Spydell and Feddersen*, 2009; *Nuss, Emma et al.*, b). In addition to removal of irrotational velocity, high frequency motions of propagating waves are filtered out of the vorticity field with a Butterworth filter with a frequency cutoff of 8 s; this cutoff value was chosen to average over four wave periods T_p (2 s), and is also approximately the time it takes for a wave to propagate through the laboratory-scale surf zone. To identify eddies in the vorticity field, a surf-zone eddy identification algorithm was developed by modifying an existing algorithm used to identify and track mesoscale eddies in satellite sea-surface-elevation data (*e.g.*, *Chelton et al.*, 2011b; *Mason et al.*, 2014; *Schlax, Michael G and Chelton, Dudley B*, 2016). The modifications to the algorithm account for the difference in scale, both temporal and spatial, and the fundamental dynamics between the surf-zone environment and mesoscale eddies.

The eddy identification algorithm follows *Schlax, Michael G and Chelton, Dudley B* (2016), but is applied to vorticity fields, rather than sea surface elevation. This method includes three basic steps: a) identification of local minima or maxima in vorticity, b) iteratively expanding the eddy boundary by the inclusion of points about the local extrema by adding points when specified eddy criteria are satisfied (described below), and c) ceasing the expansion of the eddy boundary when eddy expansion criteria fail. At a given time step, the eddy identification algorithm locates the x and y coordinates of all local minima

and maxima within the vorticity field. To focus on vorticity signals above background levels, extrema below location-dependent thresholds are discarded. A vorticity extrema threshold of 0.4 s^{-1} is set within the surf zone ($x > 28$ m) and threshold of 0.1 s^{-1} is set offshore of $x = 23$ m where background vorticity signals are weaker, with a linear transition between the two thresholds. Following the identification of the valid extrema, the eddy boundary identification procedure begins. For a given extrema with magnitude ζ_c, an iterative process is initiated, where all points within a search area (2 maximum eddy diameters) around the extrema of vorticity that fall between $\zeta_c - \Delta\zeta$ are found, with $\Delta\zeta$ = 0.05 s^{-1}. These n new points are added to the eddy if the addition of the new points satisfies six criteria:

1. The size of the eddy does not exceed a maximum size threshold ($n < n_{max}$)

2. After a minimum number of iterations, the size of the eddy must be above a certain minimum size threshold ($n > n_{min}$ after i steps)

3. The distance between any two points within the eddy do not exceed a maximum distance (d_{max})

4. The eddy has no points bordering the edge of another eddy

5. The points within the eddy are simply connected, *i.e.*, there are no holes within the eddy

6. The centroid of the eddy is within the boundary of the eddy

Once any of the criteria fails, the eddy boundary identification procedure stops, and the eddy boundary retracts to those points found in the last iteration where all criteria passed. This process is repeated for the remaining vorticity extrema in the time step and for all time steps within the model simulation.

These criteria ensure that the eddies are realistic and that the points included within an eddy do not expand into another eddy (criterion 4), the eddy has grown to a realistic size (criterion 1, 2), the eddy does not include holes (criterion 5), and the eddy does not morph into a particularly irregular shape (criterion 3, 6). Further information on the details of the growing procedure can be found in *Schlax, Michael G and Chelton, Dudley B* (2016). The primary differences between our application of the procedure and the application to sea surface height fields used in the study of mesoscale eddies are the cutoff parameters. In our method, the key parameters are: n_{min} = 50; d_{max} = 4 m; and $\Delta\zeta$ = 0.05 s^{-1}. Our method has an additional constraint that the centroid of the eddy be contained within the boundary of the eddy, which helps to ensure that eddy maintains fairly well-compact shapes.

3.2.3 *Eddy Characteristics*

The total number of eddies across the model domain at a given time is defined as N_ϵ. For each eddy, the following parameters are calculated to help characterize the identified eddies: eddy area (A_ϵ), eddy diameter (D_ϵ), eddy anisotropy ($L_{\text{maj}}/L_{\text{min}}$), eddy circulation ($\Gamma_\epsilon$), rotational speed ($U_\epsilon$), and advective non-linearity (n_ϵ). The eddy size (A_ϵ) is defined as the area encompassed by the eddy boundary and estimated:

$$A_\epsilon = N\Delta x\Delta y \tag{3.1}$$

where N is the number of grid points within the eddy, Δx and Δy are the x and y model grid discretization. From A_ϵ, an effective eddy diameter (D_ϵ), the diameter of an idealized, circular eddy is estimated as:

$$D_\epsilon = 2\sqrt{\frac{A_\epsilon}{\pi}} \tag{3.2}$$

Eddy diameter estimates are presented as normalized by the water depth (h) to provide a non-dimensional scale that can be transferred across wave conditions and between laboratory and field scale.

As eddies are not perfectly circular, we quantify eddy anisotropy by fitting an ellipse to the identified eddy boundary to quantify the major (L_{maj}) and minor (L_{min}) axes, as well as the ellipse rotation angle (θ_ϵ) to characterize the eddy shape and orientation. Eddy orientation ranges from -90° to 90°, where θ_ϵ = 0 is a cross-shore oriented eddy and $\theta_\epsilon = \pm 90^\circ$ is an alongshore oriented eddy.

Eddy circulation (Γ_ϵ) is estimated from the discretized area integral:

$$\Gamma_\epsilon = \sum_{i=0}^{N} \zeta_i \Delta x \Delta y \tag{3.3}$$

where ζ_i is the value of vorticity at grid point i of the eddy. In addition to Γ_ϵ, the rotational speed (U_ϵ) around individual eddies can be calculated. In mesoscale literature, an eddy rotational velocity is estimated as the geostrophic component of the velocity around an eddy (*Chelton et al.*, 2011b); however, for our purposes, we use Kelvin's circulation theorem to estimate U_ϵ as:

$$U_\epsilon = \frac{\Gamma_\epsilon}{\pi D_\epsilon} \tag{3.4}$$

Lastly, to quantify the non-linearity of the eddies we estimate:

$$n_\epsilon = \frac{U_\epsilon}{c_\epsilon} \tag{3.5}$$

where c_ϵ is the translation speed of an individual eddy. This speed is estimated by finding the location of the eddy at the next time step by assuming the eddy at $t_0 + \Delta t$ is within a radius of $r = 0.5$ m of the eddy position at t_0, has the same sign of rotation, and is sufficiently similar ($< 100\%$ change) in size and strength. The location of the next eddy is determined to be the eddy that minimizes the cost function of distance and change in size and circulation. Then c_ϵ is computed from the change in eddy location over Δt. These eddy characteristics are estimated from identified eddies at each time step. For eddies that were not identified at the following time step, c_ϵ was not able to be computed. While most eddies have a translation speed estimate (80%, 90%, and 80% for low, intermediate, and high spreads), these eddies were excluded for c_ϵ and n_ϵ for all model simulations.

Lastly, eddies were identified and characteristics are estimated for eddies within x = 15 - 32.5 m. The onshore limit (x = 32.5 m) corresponds to the minimum rundown and the offshore limit (x = 15 m) ensures analysis is restricted to the model extent where laboratory observations were available for comparison in model evaluation in *Nuss, Emma et al.* (b). Eddy characteristics in this region are also quantified for surf-zone regions. We define the surf-zone edge as $x = 26.9$ m, the location where the gradient in wave energy flux is greatest. Thus the surf zone width (W_{sz}) is 5.6 m, encompassing $x = 26.9 - 32.5$ m (grey shading in Fig. 3.1a-c). Additionally, we define the inner surf zone as the onshore half of the surf zone ($x = 29.7 - 32.5$ m), the outer surf zone as the offshore half of the surf zone ($x = 26.9 - 29.7$ m), the offshore region as half a surf zone width from the surf zone edge ($x = 24.1 - 26.9$ m), and far offshore as anything beyond $x - 24.1$ m.

3.3 *Results*

Eddies identified in the simulated vorticity fields align well with coherent patterns of strong local peaks in vorticity, and the eddy boundaries encompass elevated vorticity (Fig. 3.1a-c). Identified eddies are consistent with visual inspection of local extrema, particularly when background vorticity is low compared to local extrema (see offshore in Fig. 3.1b,c). Parameter choices in the algorithm were optimized to successfully identify strong magnitude and spatially coherent vorticity signals that are distinct from background levels. These choices lead to some features that are eddy-like by visual inspection, but are not identified by the algorithm, particularly in areas where background vorticity is high (e.g. within the inner-surf zone) or where local extrema are small (e.g. low directional spread or offshore).

Vorticity and rotational velocities encompassing each eddy, up the 2 normalized eddy diameters (D_e) away from the eddy center, are averaged for each simulation to provide eddy composites (Fig. 3.1d-i). On average, vorticity within the eddy is broadly symmetric with a strong extrema in the center and decreasing magnitude moving radially outward. Despite radial symmetry in vorticity, the magnitude of the rotational velocity is

asymmetrical with stronger velocities on the north side of positive eddies (Fig. 3.1g-i) and the south side of negative eddies (Fig. 3.1d-f). The structure of vorticity and velocity is similar between spreads. Additionally, the strength of the velocity around the eddies are similar in strength between spreads (see vectors in Fig. 3.1d-i); however, the magnitude of the vorticity varies with directional spread with the weakest vorticity at low directional spread and strongest vorticity at intermediate directional spread (strength of colors in Fig. 3.1d-i). The ratio of the number of positively to negatively signed identified eddies is 0.97, 0.99, and 1.0 for low, intermediate,and high directional spreads respectively. While the asymmetric velocity structure around positive and negatively signed eddies is present, the median characteristics, cross-shore profiles, and distributions of positively and negatively signed eddies are approximately equivalent (not shown) and thus, for simplicity eddy characteristics in the rest of this paper are given as a function of all eddies, rather than split out by the sense of rotation.

A large number of eddies were identified across each model simulation. There were 0.5×10^5, 2.3×10^5, and 2.8×10^5 identifications at low, intermediate, and high spreads respectively. For each model domain, this corresponds to a median number of 6 eddies per time step at low spread, 39 eddies per time step at intermediate spread, and 46 eddies per time step at high spread (Fig. 3.1a-c). Both total number of eddies and N_ϵ increase non-linearly with increasing spread; however this trend does not hold at all cross-shore locations (Fig. 3.2a). Within the surf zone ($x > 26.9$ m), median N_ϵ increases with spread from 1.4, 2.9, and 6.1 in the inner surf zone (Fig. 3.2c) and from 0, 2.5, and 5.4 in the outer surf zone (Fig. 3.2d). Offshore ($24.7 < x < 26.9$ m), median N_ϵ increases with spread with 1.1, 4, and 5 for low, intermediate, and high directional spread (Fig. 3.2b).

Eddy diameter scaled by water depth (D_ϵ/h) is largest in the surf zone and rapidly decreases near the surf-zone edge and leveling off to ~ 2 offshore (Fig. 3.2e). Within the surf zone, D_ϵ/h increases as water depth decreases from the trough to the bar crest ($28 < x < 30$ m) and then decreases rapidly from the bar crest ($x \simeq 28$ m) to the surf zone edge (Fig. 3.2e). Despite variation in cross-shore position, median D_ϵ/h has minimal

variation between spreads both offshore and in the outer surf with median values of 2.1, 2.3, and 2.3 for offshore and 5.5, 5.8, and 6.2 in the outer surf for low, intermediate, and high spreads respectively (Fig. 3.2f,g). In the inner surf, there is a slight sorting between low and higher spreads, with median D_ϵ/h of 16.5, 11, and 11.6 for low, intermediate, and high spreads respectively (Fig. 3.2h). Across all eddies in each simulation, the distributions of D_ϵ/h are right skewed with median values increasing with increasing spread from 2.6, 2.6, and 4 for low, intermediate, and high spread (Fig. 3.3a).

Eddy anisotropy, as measured by the ratio of major axis (L_{maj}) to minor axis (L_{min}), varies as well, with eddies becoming more circular ($L_{\text{maj}}/L_{\text{min}}$ decreasing towards 1) further offshore (Fig. 3.2i). In the inner and outer surf zone, median $L_{\text{maj}}/L_{\text{min}}$ decreases with increasing spread with 3.4, 2.9, and 2.8 in the inner surf and 2.8, 2.3, and 2.1 in the outer surf from low, intermediate, and high spreads (Fig. 3.2k,l). Offshore, median $L_{\text{maj}}/L_{\text{min}}$ is approximately equivalent, with 2.4, 2.5, and 2.3 for increasing spread (Fig. 3.2j). Despite small differences in $L_{\text{maj}}/L_{\text{min}}$ within cross-shore regions, median values across all eddies are nearly indistinguishable between simulations, with median $L_{\text{maj}}/L_{\text{min}}$ at 2.4, 2.3, and 2.2 for increasing spread (Fig. 3.3b).

In addition to being elliptic in shape, L_{maj} can be rotated by an angle of rotation (θ_ϵ). For all simulations, the distribution of θ_ϵ for all eddies is centered around 0°, cross-shore oriented, with mean values of 1.5°, 1.6°, and 1.6° for low, intermediate, and high directional spreads (Fig. 3.3c). Despite most eddies being nearly cross-shore oriented and a decreasing number of eddies as $|\theta_\epsilon|$ increases, there is an increase in alongshore oriented ($\theta_\epsilon = \pm 90°$) eddies (Fig. 3.3c). Despite eddy orientation ranging from cross to alongshore oriented and $L_{\text{maj}}/L_{\text{min}}$ varying in the cross-shore, the mean θ_ϵ does not vary with cross-shore position and is constant around $\sim 1.5°$ (not shown).

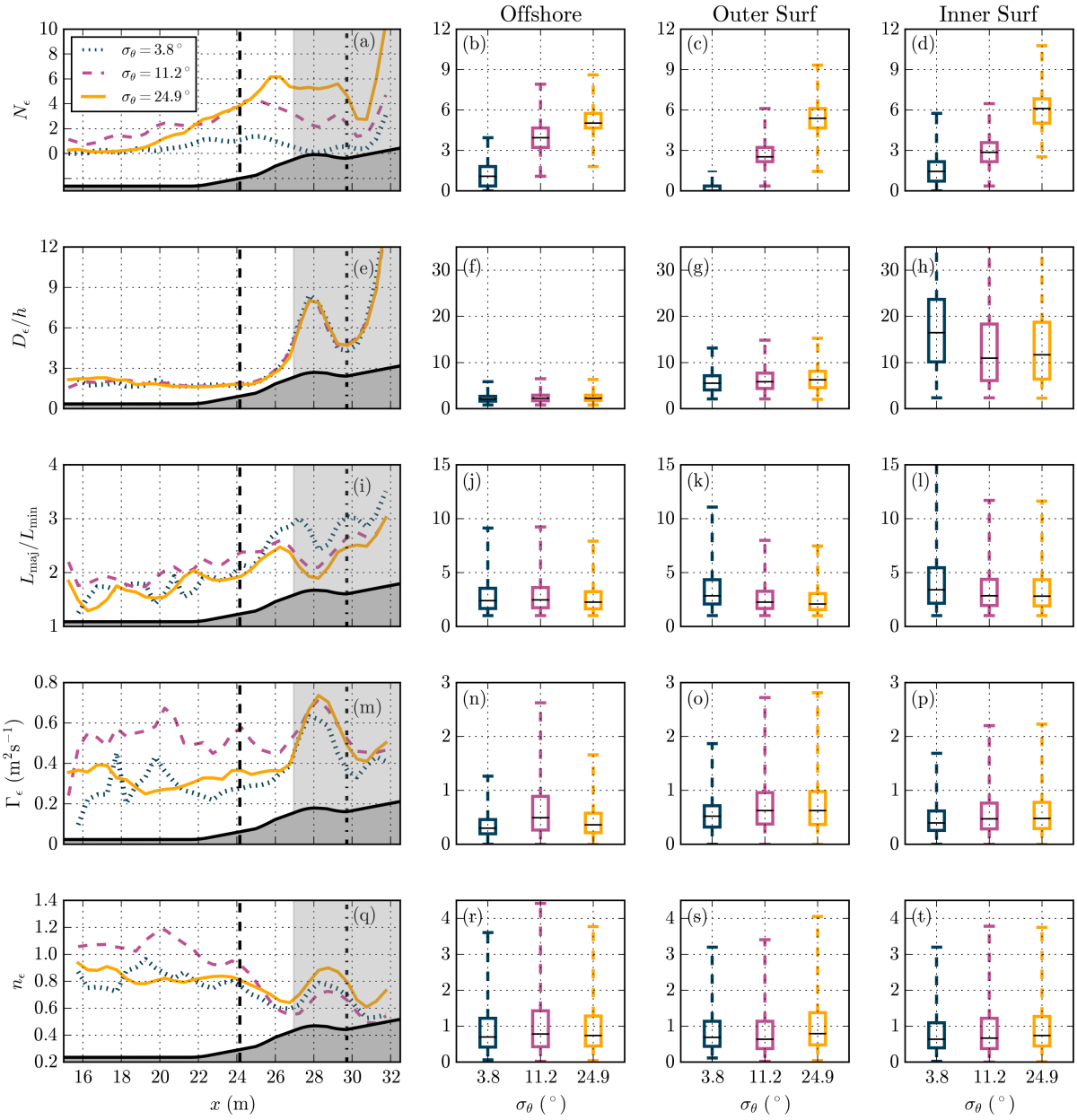

Figure 3.2: Cross-shore profiles of median (a) number of eddies (N_ϵ), (e) eddy diameter to water depth (D_ϵ/h), (i) ratio of major to minor axes (L_{maj}/L_{min}) of fitted ellipse to eddy boundary (m) eddy circulation (Γ_ϵ), and (q) advective non-linearity (n_ϵ) for low, intermediate,and high directional spread (σ_θ) (colors and linestyles in legend in (a)). Box plots for (d,h,l,p,t) within the inner surf zone ($x = 29.7 - 32.5$ m), (c,g,k,o,s) within the outer surf zone ($x = 26.9 - 29.7$ m), and (b,f,j,n,r) offshore of the surf zone ($x = 24.1 - 26.9$ m) for (b,c,d) N_ϵ, (f,g,h) D_ϵ/h, (j,k,l) L_{maj}/L_{min}, (n,o,p) Γ_ϵ, and (r,s,t) n_ϵ for low, intermediate, and high σ_θ (colors matching cross-shore curves in legend in (a)). Note that boxplot whiskers are extended to 3 times the interquartile range (compared with standard 1.5) due the skewness of the data.

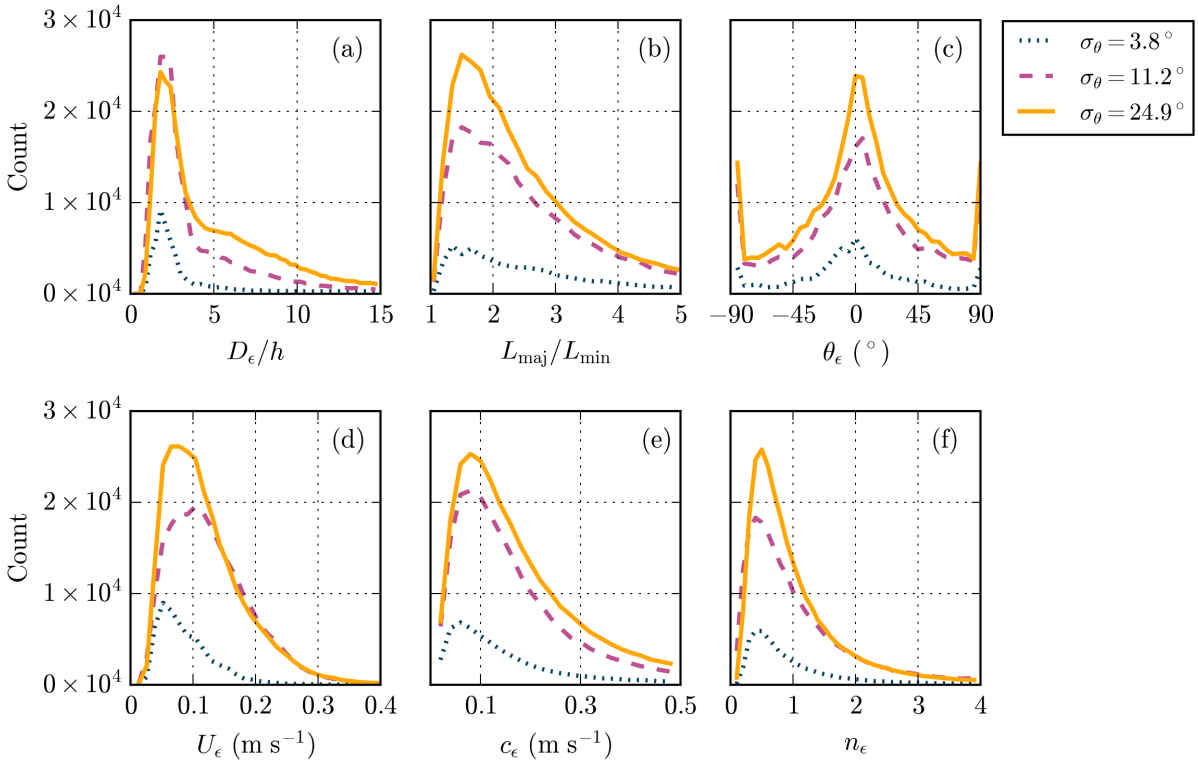

Figure 3.3: Distribution of (a) the ratio of an assumed circular eddy diameter (D_ϵ) to water depth (h), (b) the ratio of the major (L_{maj}) and minor (L_{maj}) axes of fitted ellipse to eddy boundary (c) the angle of rotation of the fitted ellipse (θ_ϵ) where 0° is cross-shore oriented and 90° is alongshore oriented, (d) the rotational velocity (U_ϵ) of individual eddies, (e) the translation speed of each eddy (c_ϵ), (f) the advective nonlinearity parameter (n_ϵ) for each eddy for low, intermediate, and high directional spreads (color and linestyle in legend)

Eddy circulation (Γ_ϵ) varies with cross-shore position similar to D_ϵ/h with an increase in Γ_ϵ from the trough to the bar crest ($28 < x < 30$ m) and then decreasing in magnitude from the bar crest ($x \simeq 28$ m) to the surf zone edge for all directional spreads (Fig. 3.2m). Median Γ_ϵ in the surf zone shows stronger eddies at intermediate and high spreads with 0.4, 0.5, and 0.5 m^{2}s^{-1} in the inner surf and 0.5, 0.6, and 0.6 m^{2}s^{-1} in the outer surf for low, intermediate, and high spreads (Fig. 3.2p). Offshore ($x < 26.9$ m), Γ_ϵ is relatively constant with cross-shore position but varies by directional spread, with stronger Γ_ϵ for

intermediate spread (Fig. 3.2m). Median Γ_ϵ offshore is 0.3, 0.5, and 0.4 m^2s^{-1} for low, intermediate, and high directional spread respectively (Fig. 3.2n).

Similar to D_ϵ/h and Γ_ϵ, advective non-linearity (n_ϵ) exhibits a local peak near the bar crest ($x \simeq 28$ m) in the surf zone for all spreads (Fig. 3.2q). In the surf zone and offshore median n_ϵ is less than 1 for all spreads (Fig. 3.2r-t). In the inner surf, median n_ϵ is 0.6, 0.7, and 0.7 for increasing spread (Fig. 3.2t). In the outer surf zone, median n_ϵ is slightly elevated with 0.7, 0.6, and 0.8 for low, intermediate, and high directional spreads (Fig. 3.2s). Offshore, median n_ϵ is instead slightly elevated for intermediate spread with 0.7, 0.8, and 0.7 for increasing spread (Fig. 3.2r). Across all eddies, median n_ϵ is smallest for low directional spread with 0.7, 0.8, and 0.8 for increasing spread (Fig. 3.3f). While the distribution of n_ϵ is similar between spreads, the upper tails of the distributions of U_ϵ shift with spread resulting in median U_ϵ with 0.07, 0.11, and 0.10 ms^{-1} for increasing spread (Fig. 3.3d). The upper tail of the c_ϵ distribution for intermediate spread is reduced leading to median c_ϵ of 0.1, 0.13, and 0.13 ms^{-1} (Fig. 3.3e).

3.4 Discussion

The application of mesoscale eddy identification to surf zone vorticity gives a novel perspective on surf-zone eddy characteristics and transformation across the surf zone and inner shelf and with varying wave directional spread. This comparison highlights similarities of eddy characteristics that span wave conditions. From rotational velocity eddy composites, we see that regardless of directional spread the velocity structure around an eddy is asymmetric (Fig. 3.1d-i). This asymmetry is not consistent with expectations of velocity structure in Rankine vortices, which have been used to approximate velocity and circulation of identified surf-zone eddies on variable bathymetry (*Bondehagen et al.*, 2024). Asymmetric velocity may suggest that eddies tend to be paired with a positive and negative dipole, such that their orientation influences each other enhancing offshore directed flow between the eddy pairs. Alternatively, asymmetric velocity may also suggest that despite a coherent vorticity extrema, surf-zone eddies exist in background currents

that modify the vortex structure. While irrotational features of individual breaking waves are removed prior to eddy identification and compositing, background velocity is not filtered out. In contrast to mesoscale eddies, surf-zone eddies are of a similar length scale ($O(1\text{m})$) as background currents compared with mesoscale eddies ($O(100\text{km})$) and their background currents ($O(1000\text{km})$).

In addition to their structure, eddy size, shape, circulation, and advective non-linearity all exhibit similar features between wave conditions. The presence of an alongshore uniform bar near the surf-zone edge (bar crest at $x \simeq 28$ m, surf-zone edge at $x = 26.9$ m) influences these eddy characteristics as they transform across the surf zone. From the trough to the bar crest (decreasing depth), eddies get larger and increase circulation strength, while also decreasing in their ellipticity, becoming more circular, and increasing their non-linearity. From the bar crest to the edge of the surf zone, eddies shrink in size, but become more elliptical, while weakening their circulation and decreasing their non-linearity. This transformation of eddies across the surf zone is consistent with prior analysis of alongshore wavenumber spectra of vorticity, which have shown that mean eddy length increases from the inner to outer surf zone (*Baker et al.*, 2021; *O'Dea et al.*, 2021) consistent with the transformation of eddy size through the surf zone in our simulations.

Additionally, transformation of eddy characteristics over the bar crest appears consistent with conservation of potential vorticity. As the depth shoals to the bar crest, conservation of potential vorticity would suggest that the magnitude of the local vorticity of an eddy would decrease from the trough to the bar crest. Strength of local vorticity can decrease in two ways - through a reduction in rotational currents (i.e. direct decrease in rotational velocities) or an increased area (i.e. larger circumference for rotational speed to traverse, thus decreased vorticity). For all directional spreads, we observe an increase in eddy size from the trough to the bar crest and then a decrease in eddy size from the bar crest to the surf zone edge (Fig. 3.2e), indicative of an expected decreased in local vorticity magnitude. While not shown here, the median eddy vorticity ($\zeta_\epsilon = \Gamma_\epsilon / A_\epsilon$) decreases from the trough to the bar crest and slightly increases from the bar crest to the surf zone

edge.

While there are a number of eddy characteristics that are consistent between wave conditions, there are also distinct differences. Most notably, the total number of identified eddies and the median number of eddies across the surf zone non-linearly increase with increasing spread. This increase in eddy counts with spread is consistent with prior work showing that low frequency power (*O'Dea et al.*, 2021; *Nuss, Emma et al.*, b) and vorticity variance (*Spydell and Feddersen*, 2009; *Baker et al.*, 2021; *Dooley et al.*, 2024) increase with increasing directional spread in the inner surf zone. Prior work has also shown that there is higher vorticity variance (*Spydell and Feddersen*, 2009; *Kumar and Feddersen*, 2017a; *Baker et al.*, 2021) and higher low-frequency power (*Feddersen et al.*, 2011; *O'Dea et al.*, 2021) in the inner surf zone compared with the outer surf and offshore; however, median eddy counts increase from the inner to outer surf for all directional spreads. This discrepancy may suggest that eddy counts characterize an aspect of the vorticity field that is distinct from these Eulerian based metrics; however, this past work characterizes surf-zone vorticity on planar and terraced beaches and when comparing the cross-shore profiles of eddy counts for these wave conditions to cross-shore profiles of low-frequency power on the same cross-shore bathymetry and wave conditions, the eddy counts and low-frequency power do co-vary together (*Nuss, Emma et al.*, b).

In addition to eddy counts, eddy ellipticity also varies slightly between wave conditions in the surf zone. Eddies are more elliptical at low directional spread compared to intermediate and high spreads within the surf zone. While the magnitude of these eddy characteristics varies, their trend as a function of cross-shore position is similar and appears influenced by cross-shore bathymetry. Moving from the trough to the bar crest, eddies become more circular and eddy size increases, suggesting that as elliptical eddies in the inner surf zone conserve potential vorticity, they do so by increasing their area along L_{min}, thereby decreasing their ellipticity. As eddies are primarily cross-shore oriented (Fig. 3.3c), increasing L_{min} likely is aligned in the cross-shore (i.e. along constant water depth). Conversely, moving from the bar crest to the surf-zone edge, eddies again

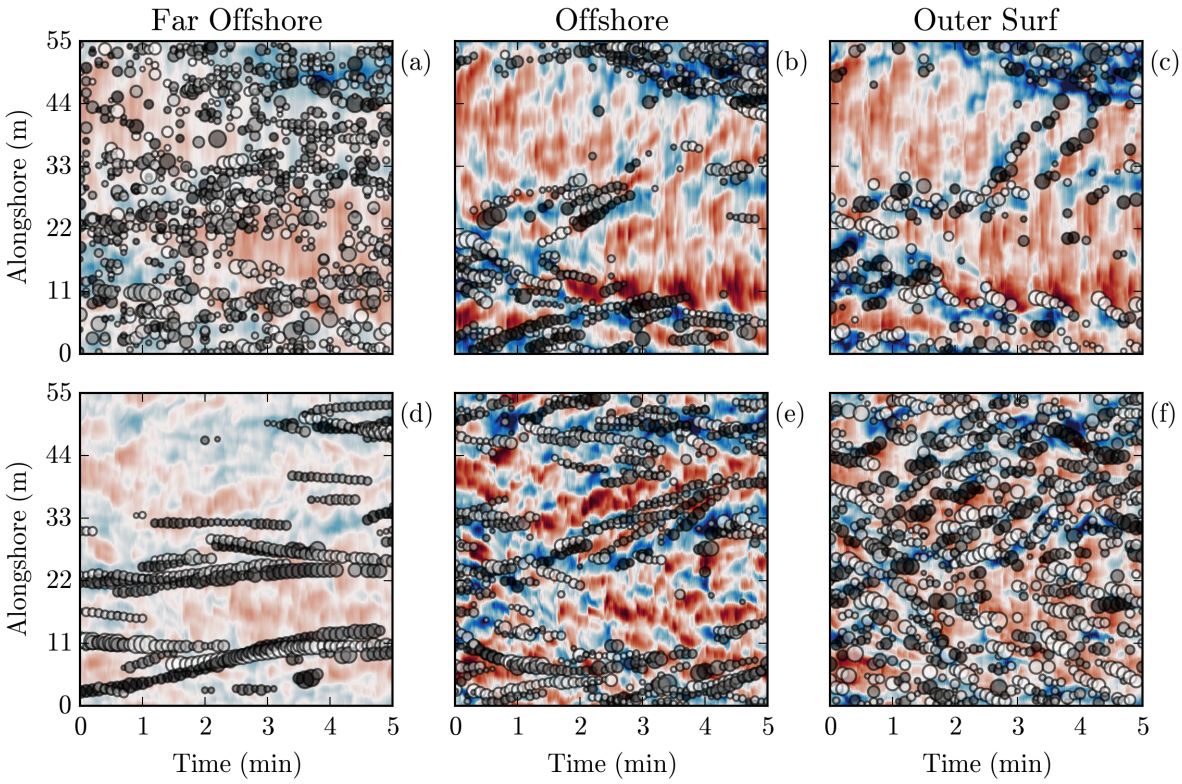

Figure 3.4: Alongshore locations of identified eddies in the (c,f) outer surf ($x = 26.9 - 29.7$ m), (b,e) offshore ($x = 24.1 - 26.9$ m), and (a,d) far offshore ($x < 24.2$ m). Eddy locations are denoted by circles scaled by eddy size (A_ϵ) and magnitude of rotational velocity (U_ϵ). Cross-shore rotational velocity (u_ψ) is shown in red/blue colors in each panel, with red denoting onshore flow and blue denoting offshore flow. (c,f) Shows u_ψ at the surf zone edge ($x = 26.9$ m), (b,e) shows u_ψ averaged over the offshore region ($x = 24.1 - 26.9$ m), and (a,d) shows u_ψ averaged over $x = 15 - 24.2$ m. Eddy locations and cross-shore velocity is shown for (a,b,c) intermediate and (d,e,f) high directional spread (σ_θ). Note that eddy positions are subsampled for every 30 time steps (6 s).

become more elliptic as they decrease their area.

Characterizing individual eddies throughout the surf zone and offshore provides a novel perspective into surf zone vorticity dynamics. This eddy focused perspective aligns well with aspects of Eulerian metrics of surf-zone vorticity, but also highlights where eddy metrics provide a distinctly different view of the surf zone. Notably, while the

total number of eddies varies, distributions and cross-shore profiles of eddy size and shape show statistically insignificant differences between directional spreads. In contrast, from a Eulerian perspective it has been shown that energy at small scales in alongshore wavenumber spectra of vorticity increases with increasing directional spread, decreasing mean length scales for increasing spreads (*Spydell and Feddersen*, 2009; *O'Dea et al.*, 2021; *Nuss, Emma et al.*, b). This discrepancy highlights the need to tie these two perspectives together.

To begin this process, we compare cross-shore rotational velocity (u_ψ) at the surf-zone edge to alongshore locations, size, and strength of rotational velocity of identified eddies within the outer surf zone, offshore, and far offshore for intermediate and high directional spreads (Fig. 3.4). This visual comparison provides initial insight into how these two perspectives may merge. Across all cross-shore regions, eddy size is indistinguishable between intermediate and high directional spreads (compare circle size in top to bottom row in Fig. 3.4). In contrast, eddy counts vary between spreads with a larger number of eddies in the outer surf and offshore for high spread, but a larger number of eddies far offshore for intermediate spread (Fig. 3.4). While eddy counts differ between spreads and cross-shore position, the locations of eddies in the outer surf and offshore tend to be co-located with inflection points in cross-shore flow or within offshore directed flow for both intermediate and high spreads (see eddy circles in blue velocities Fig. 3.4). This co-location of eddies and background u_ψ contributes to higher eddy counts at large directional spread, as the alongshore length-scales observed in u_ψ in the outer surf and offshore are shorter for high spreads. This decrease in alongshore length-scales with spread is consistent with prior work that has shown that mean alongshore length-scales in vorticity decrease with increasing spread (*Spydell and Feddersen*, 2009; *Baker et al.*, 2021).

Co-location of eddies with inflections in u_ψ is to some extent expected, as eddies are identified from vorticity which is present where the alongshore gradient of cross-shore velocities is non-zero. However, the locations and number of eddies is related to cross-shore exchange and tracer transport is still unknown. Far offshore, eddy counts are

significantly larger and spatially variable for intermediate vs. high directional spread (Fig. 3.4a,d). For intermediate spread, these far offshore eddies are also associated with higher advective non-linearity (Fig. 3.2q) and stronger rotational velocities (color of circles in Fig. 3.4a) compared with high directional spread.

A larger number of more nonlinear eddies far offshore is consistent with expectations from prior work showing that cross-shore exchange velocities are strongest for intermediate spreads for these model simulations (*Nuss, Emma et al.*, b). Elevated cross-shore exchange would suggest strong eddy driven transport and therefore more non-linear eddies, which has a stronger ability to transport material (*Flierl, Glenn R*, 1981; *Chelton et al.*, 2011a) and is characterized by a greater number of eddies that transport offshore. Investigation of the transformation and tracking of these individual eddies that eject offshore may provide insight into how, why, and when transient rip currents develop offshore ejections. However, the depth-averaged nature of the simulations constrain eddy evolution to two-dimensional dynamics and do not account for three-dimensionality of eddies as they propagate into deeper water. It is known that three-dimensionality may affect how eddies interact in the surf zone (*Marchesiello et al.*, 2021) and as they move offshore (*Kumar and Feddersen*, 2017b). Therefore future work can quantify and relate these eddy metrics to exchange velocities and explore these dynamics with a three-dimensional model that includes the impact of stratification and three-dimensionality of the eddies.

3.5 *Summary and conclusions*

In this study we take an eddy focused perspective of surf-zone eddy dynamics by adapting methods commonly used in mesoscale eddy identification to identify and characterize eddies in wave-resolved numerical simulations. We characterize the distributions of eddy characteristics for low, intermediate,and high directional spreads and quantify how eddy characteristics vary in the cross-shore. We find that the number of eddies increases with increasing spread, but exhibit a similar size, strength, and non-linearity within the surf zone. However, far offshore of the surf zone, intermediate-directional spread

has the largest proportion of eddies that advect offshore, as well as larger circulation strength and non-linearity. Eddy characteristics can be linked to Eulerian perspectives to better understand the dynamics leading to offshore ejection events and the implications for material transport by surf-zone eddies. Future work should explore how eddy characteristics relate to other surf zone processes, as well as investigate the life cycle and trajectories of individual eddies to better understand what leads to variation in offshore eddy driven transport across wave conditions.

Chapter 4
TRACKING EDDIES THROUGH THE SURF ZONE

How do coherent eddies vary over their life cycle?

4.1 Introduction

On alongshore-uniform beaches, directionally spread wave conditions result in short-crested breaking waves. In these short-crested waves, along-crest irregularities in the strength of wave breaking, particularly at the ends of breaking waves (*Peregrine*, 1998), generate small-scale vertical vorticity in the surf zone (*Clark et al.*, 2012; *Kirby and Derakhti*, 2019; *Wei et al.*, 2017). Energy from small-scale vorticity can be transferred to larger scale rotational motion, consistent with a forced two-dimensional turbulence system (*Elgar and Raubenheimer*, 2020; *Elgar et al.*, 2023; *Baker et al.*, 2023a; *Spydell and Feddersen*, 2009; *Feddersen*, 2014).

These larger rotational motions can enhance cross-shore exchange through the development of offshore ejection of material via transient rip currents (*Johnson and Pattiaratchi*, 2006; *Clark et al.*, 2010; *Feddersen et al.*, 2011; *Hally-Rosendahl and Feddersen*, 2016; *Suanda and Feddersen*, 2015; *Kumar and Feddersen*, 2017a,b; *Grimes et al.*, 2020; *Grimes and Feddersen*, 2021; *Choi and Roh*, 2021). These ejection events driven by horizontal rotational motions can enhance tracer dispersion (*Hally-Rosendahl et al.*, 2014) and cross-shore exchange of tracers (*Kumar and Feddersen*, 2017a; *Grimes et al.*, 2020), influencing the transport of pollutants impacting nearshore water quality (*Halpern et al.*, 2008; *Boehm et al.*, 2017) and larval transport and recruitment (*Morgan et al.*, 2017; *Moulton et al.*, 2023).

Prior modeling work on along-shore uniform planar beaches has investigated the

relationship between wave field conditions, particularly wave directional spread, and the strength of cross-shore exchange velocities, finding that exchange velocities are higher for larger spreads than for low directional spreads (*Suanda and Feddersen*, 2015; *O'Dea et al.*, 2021; *Nuss, Emma et al.*, b). While these previous model simulations on planar beaches have suggested that exchange monotonically increases with increasing spread (*Suanda and Feddersen*, 2015), simulations using terraced and barred-beaches have shown that exchange velocities may plateau or peak at mid-directional spreads (*O'Dea et al.*, 2021; *Nuss, Emma et al.*, b). This difference in behavior suggests that further investigation of how surf-zone vorticity evolves to generate offshore flow at the surf-zone edge is needed to better predict exchange velocities.

Accurately predicting exchange velocities requires understanding vorticity generation, and also how vorticity is transformed and develops into large scale flows. Prior work using structure functions of surf-zone velocities has indicated consistency with a forced two-dimensional turbulence system (*Spydell and Feddersen*, 2009; *Feddersen*, 2014; *Elgar and Raubenheimer*, 2020; *Elgar et al.*, 2023). However, this consistency is not observed across all directional spreads in laboratory experiments (*Baker et al.*, 2023a). This discrepancy highlights gaps in our understanding of the transfer of energy between scales, the nature of eddy-eddy interactions, the life cycle of surf zone eddies, and the development of transient rip currents in the surf zone for varying wave conditions.

Prior investigation of surf-zone vorticity has explored Eulerian velocities and used spectral methods to understand how energy associated with rotational motions varies across scales and between wave conditions. To complement this Eulerian perspective, a mesoscale eddy identification algorithm was applied to surf zone vorticity to identify coherent rotational motions, or eddies, in the surf zone *Nuss, Emma et al.* (a). Application of this identification method has allowed for characterizing surf-zone eddies to complement Eulerian analyses (e.g. wave number spectra). It was found that eddy characteristics of size, shape, and rotational strength vary as a function of water depth, particularly over the bar crest, likely related to conservation of potential vorticity (*Nuss, Emma et al.*, a). While

these size, shape, and strength characteristics are tied to bathymetry and vary minimally between low to high directional spreads, the total number of eddies in the surf zone increase nonlinearly with increasing spread. Despite a larger number of eddies in the surf at high spread, a greater number of eddies, with stronger circulation and non-linearity, for intermediate directional spread, consistent with a peak in exchange velocities (*Nuss, Emma et al.*, b,a).

While eddy identification has allowed for quantification of eddy characteristics throughout the surf zone and with varying wave conditions, questions about how individual eddies transform over their life cycle and why some eddies advect offshore leading to cross-shore exchange and other stay in the surf zone remain unanswered. To investigate these questions from this eddy focused perspective, we apply a tracking algorithm to identified eddies in a model simulation of intermediate directionally spread waves on a laboratory barred beach (*Nuss, Emma et al.*, b,a). The dataset of eddies tracked from initial identification to cessation provides a new way to explore the transformation of vorticity from wave-breaking driven generation, evolution, to offshore ejection.

Identification and tracking of individual eddies results in a large spatio-temporal dataset. Methods of analyzing trajectory data have increased with the prevalence of location tracking information. The use of machine learning has increasingly become a tool used to analyze and predict trajectory paths (*Gariel et al.*, 2011; *Zheng*, 2015; *Grossi et al.*, 2020; *Kontopoulos et al.*, 2021; *Qiao et al.*, 2022). Clustering is an unsupervised machine learning tool that is useful for classifying patterns of data into groups or clusters (*Jain et al.*, 1999). There are a variety of clustering methods, including K-means, which have been used for a variety of clustering applications including monitoring airspace and classifying airplane trajectories (*Gariel et al.*, 2011), differentiating driving patterns (*Wu and Chan*, 2018), and determining storm type and path trajectories (*Gaffney and Smyth*, 1999; *Smyth et al.*, 1999). In this paper we apply an unsupervised K-means algorithm to cluster similar trajectories to characterize types of eddy trajectories and investigate how eddies evolve in the surf zone.

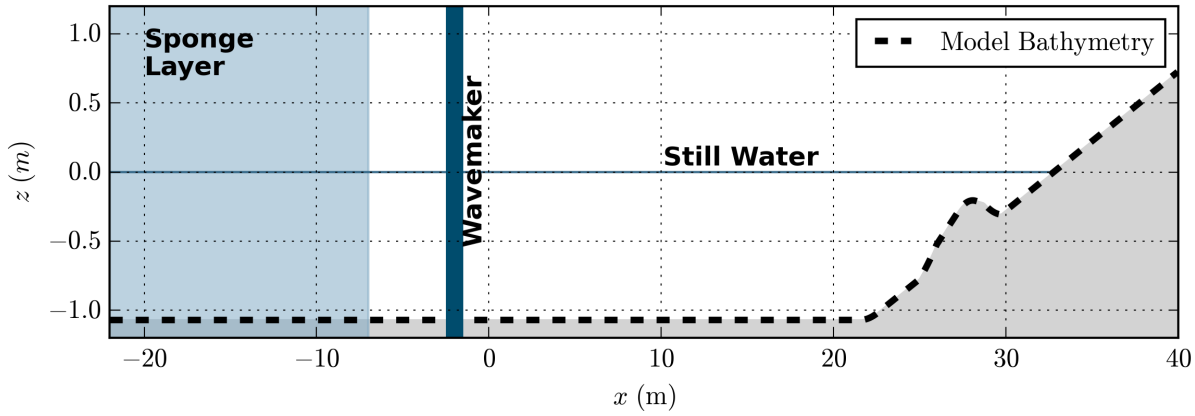

Figure 4.1: Cross-shore profile of model bathymetry with dashed black line and grey shading denoting the model bathymetry, horizontal blue line denoting the still water level, vertical thick blue line denoting the location of the wavemaker, and light blue shading denoting the region of the sponge layer in the model setup.

4.2 Methods

4.2.1 Numerical modeling

We use a numerical simulation of directionally spread irregular waves on a laboratory-scale barred beach using FUNWAVE-TVD, a phase-resolved Boussinesq model (*Shi et al.*, 2012), from *Nuss, Emma et al.* (b). The model domain is 62 m in the cross-shore (dx = 0.05 m) and 55 m in the alongshore (dy = 0.1 m). The model bathymetry is alongshore uniform, with a bar ($x \simeq 27.5$ m) and trough ($x \simeq 28$–31 m) (Fig. 4.1). The model bathymetry and configuration was set up to simulate wave conditions observed during laboratory experiments (*Baker et al.*, 2023b) and remote sensing and in situ data from the experiments were used to evaluate model performance *Nuss, Emma et al.* (b). Wave forcing of 0.25 m significant wave height (H_s) with a peak period (T_p) of 2 s and directional spread (σ_θ) of $\sim 11.2^\circ$ was simulated for 25 minutes. The first 5 minutes of the model simulation were excluded from all analyses to allow for model spinup.

4.2.2 *Eddy identification*

Spatially coherent features of vorticity, referred to as eddies throughout this paper, were identified using a modified mesoscale eddy identification algorithm *Nuss, Emma et al.* (a). This eddy identification algorithm is applied to low-pass filtered vorticity (Butterworth filter, frequency cutoff of 8 s) computed from the rotational component of the simulated velocity field via a Helmholtz decomposition (*e.g.*, *Spydell and Feddersen*, 2009; *Nuss, Emma et al.*, b). Based on *Schlax, Michael G and Chelton, Dudley B* (2016), the eddy identification algorithm locates vorticity extrema and then expands the eddy boundary around the extrema. The eddy boundary expands based on a set of criteria that ensures that the eddy is a reasonable size (i.e. not too large or small) and shape (i.e. non-overlapping points or holes within an eddy), full details of eddy boundary expansion algorithm are described in *Schlax, Michael G and Chelton, Dudley B* (2016); *Nuss, Emma et al.* (a).

In addition to identifying the location and boundary of eddies in the model simulation, the eddy identification algorithm quantifies characteristics of individual eddies. For each identified eddy, the cross-shore (x) and alongshore (y) coordinates of the eddy center, the area associated with the eddy boundary (A_e), and the circulation of the identified eddy (Γ_e) were quantified. The eddy size (A_e) is defined as the area encompassed by the eddy boundary and estimated as:

$$A_e = N\Delta x\Delta y \tag{4.1}$$

where N is the number of grid points within the eddy, Δx and Δy are the x and y model grid discretization. Eddy circulation (Γ_e) is estimated from Kelvin's circulation theorem as a discretized area integral:

$$\Gamma_e = \sum_{i=0}^{N} \zeta_i \Delta x \Delta y \tag{4.2}$$

where ζ_i is the value of vorticity at grid point i of the eddy. These eddy characteristics are quantified for all eddies at all time steps and are used for in tracking eddies in time.

4.2.3 *Eddy tracking*

Identified eddies and eddy characteristics are used to track eddies through time and space. The eddy tracking algorithm uses several assumptions:

1. The sign of the vorticity signature of the eddy cannot change at any time
2. Eddies do not travel more than 0.3 m in a 0.2 s timestep (corresponding to speeds less than 1.5 m s^{-1})
3. Eddies can only be in one track (i.e. merging or splitting of eddies are not accounted for in this algorithm)
4. Changes in eddy properties (A_ϵ and Γ_ϵ) stay within a designated threshold percentage (100% change from prior time step)

Based on these assumptions our eddy tracking algorithm goes through the following steps to track a given eddy through time. At an initial time step, t_0, we have our initial eddy, ϵ_{t_0}, with size, $A_{\epsilon_{t_0}}$, and circulation $\Gamma_{\epsilon_{t_0}}$. To track ϵ_{t_0}, first all eddies at the next time step, $\epsilon_{t_0+\Delta t}$, are found. Next, only eddies within a distance threshold, $d < 0.3$ m, are retained from $\epsilon_{t_0+\Delta t}$, such that a new subset of eddies is found where:

$$\epsilon'_{t_0+\Delta t} = \{\epsilon \in \epsilon_{t_0+\Delta t} |\ d < 0.3\text{m}\} \tag{4.3}$$

Next, a sign check between ϵ_{t_0} and $\epsilon'_{t_0+\Delta t}$ subsets the possible eddies further such that:

$$\epsilon''_{t_0+\Delta t} = \{\epsilon \in \epsilon'_{t_0+\Delta t} |\ \text{sgn}(\Gamma_\epsilon) = \text{sgn}(\Gamma_{\epsilon_{t_0}})\} \tag{4.4}$$

If there are multiple eddies in $\epsilon''_{t_0+\Delta t}$, then a cost function is minimized:

$$L = \min\{d_\epsilon + \Delta A_\epsilon + \Delta\Gamma_\epsilon\} \tag{4.5}$$

where d_ϵ is the distance, ΔA_ϵ is the percentage change in eddy size, and $\Delta\Gamma_\epsilon$ is the percentage change in circulation between ϵ_{t_0} and eddies in $\epsilon''_{t_0+\Delta t}$. Finally, the eddy that

minimizes this cost function goes through a final check to ensure that ΔA_ϵ and $\Delta\Gamma_\epsilon$ are below a 100% change from the prior time step and that this eddy is not included in any other eddy trajectories. Testing of the threshold for ΔA_ϵ and $\Delta\Gamma_\epsilon$ was found to not be sensitive and is mainly meant to check that A_ϵ and Γ_ϵ are not more than doubling their size. If this last condition on size and inclusion in other eddy trajectories is met, then this eddy is marked as tracked and added to the eddy track. Then, this process is repeated for $t_0 + 2\Delta t$ and so forth until no eddies satisfy all these conditions.

Eddy tracks can occasionally stop preemptively due to intermittent eddy changes due to short lived changes in the vorticity field (e.g., vorticity signature from wave breaking) that impact the eddy identification algorithm making eddy size or circulation change drastically or make the eddy not identifiable for a short period of time (i.e. 10 time steps, 2 s). To account for this intermittency, if an eddy at a given time step, t_i, is a part of an existing trajectory and no eddy satisfying the above conditions is met at $t_{i+\Delta t}$. Instead of stopping the eddy trajectory at t_i with the last eddy found, the eddy tracking algorithm will continue to $t_{i+2\Delta t}$ to check for eddies that satisfy the criteria using eddy size, circulation, and location from the last time step where an eddy in the track was identified, t_i. If an eddy at $t_{i+2\Delta t}$ is found that satisfies the above tracking conditions, then the tracking algorithm moves forward in time normally. If no eddy is found at $t_{i+2\Delta t}$ to satisfy the tracking conditions, the algorithm again jumps forward to $t_{i+3\Delta t}$, but continuing to use eddy information from t_i. This jumping method will continue for up to 10 time steps beyond t_i. If no eddies are found at each iteration, then the track finishes and the tracking algorithm moves to the next eddy.

This entire eddy tracking process is iteratively applied to each eddy at t_0, finding the entire track for ϵ_1 up to ϵ_N, where N is the number of eddies identified at t_0. Then the eddy tracking algorithm advances forward in time to $t_0 + \Delta t$ and iteratively applied to each eddy identified at $t_0 + \Delta t$ that are not already in an eddy track. This process continues until the last time step and results in every identified eddy from the model simulation included in an eddy track, even if the track duration is a single time step.

4.2.4 *Eddy trajectory statistics*

From the eddy identification process, eddy size (A_ϵ) and circulation (Γ_ϵ) are quantified for all eddies. In addition to these eddy statistics, other statistics are quantified from the eddy trajectories to characterize the nature of each trajectory. First, a track duration, T_ϵ, is quantified as the duration that a track lasts, from the time step associated with the first eddy in the trajectory to the time step associated with the last eddy in the trajectory. Additionally, from the x and y positions of each eddy center throughout the track, the distance traveled from each time step is estimated as Euclidean distance:

$$d_i = \sqrt{(x_i - x_{i+\Delta t})^2 + (y_i - y_{i+\Delta t})^2} \tag{4.6}$$

where $(x_i,\ y_i)$ are the position coordinates of the eddy at t_i and $(x_{i+\Delta t},\ y_{i+\Delta t})$ are the position coordinates of the eddy at $t_{i+\Delta t}$. This distance is then used to compute an eddy translation speed, c_ϵ:

$$c_\epsilon = \frac{d_i}{\Delta t} \tag{4.7}$$

In addition to translation speed, the direction of translation is estimated from the x and y positions of each eddy throughout the track by:

$$\Theta_\epsilon = \arctan\left(\frac{y_{i+\Delta t} - y_i}{x_{i+\Delta t} - x_i}\right)\frac{180}{\pi} \tag{4.8}$$

where Θ_ϵ is between $\pm 18o^\circ$ with 0° associated with onshore cross-shore translation, $\pm 180^\circ$ associated with offshore cross-shore translation, and $\pm 90^\circ$ associated with alongshore translation. We use Θ_ϵ to decompose eddy translation speed (c_ϵ) to along (u_ϵ) and cross-shore (v_ϵ) translation speeds:

$$\begin{aligned} u_\epsilon &= c_\epsilon \cos(\Theta_\epsilon) \\ v_\epsilon &= c_\epsilon \sin(\Theta_\epsilon) \end{aligned} \tag{4.9}$$

with $u_\epsilon < 0$ corresponding to offshore eddy translation, $u_\epsilon >$ corresponding to onshore eddy translation, $v_\epsilon < 0$ corresponding to southward (decreasing y) alongshore

translation, and $v_\epsilon > 0$ corresponding to northward (increasing y) alongshore translation. Alongshore translation speed throughout the results will be reported as $|v_\epsilon|$ since alongshore translation is expected to be symmetric and have no directionality preference.

In addition to Γ_ϵ, the rotational speed (U_ϵ) around individual eddies is estimated using Kelvin's circulation theorem as:

$$U_\epsilon = \frac{\Gamma_\epsilon}{\pi D_\epsilon} \tag{4.10}$$

where D_ϵ is the diameter of the eddy assuming a circle with area A_ϵ:

$$D_\epsilon = 2\sqrt{\frac{A_\epsilon}{\pi}} \tag{4.11}$$

Finally, we use U_ϵ and c_ϵ to quantify the advective nonlinearity (n_ϵ) of the eddies:

$$n_\epsilon = \frac{U_\epsilon}{c_\epsilon} \tag{4.12}$$

When n_ϵ is greater than 1, eddies are nonlinear and associated with greater potential to transport tracers due to its slow translation speed or strong rotational speed (*Flierl, Glenn R*, 1981; *Chelton et al.*, 2011a,b; *Wekerle et al.*, 2020).

4.2.5 Trajectory clustering

The eddy tracking algorithm results in a multitude of data, which includes spatiotemporal information about eddy position and characteristics for all eddy tracks throughout the simulation. Parsing out meaningful patterns in these trajectories requires comparison of many features of the trajectories, i.e. duration, translation speed, eddy size, etc. A useful step towards finding meaningful patterns in these trajectories is to cluster these trajectories into trajectory types. One approach for clustering trajectory data is through quantifying features attributed to each trajectory, for example, the total distance traveled, median speed, number of stops, etc. (*e.g.*, *Wu and Chan*, 2018; *Gariel et al.*, 2011).

To cluster these eddy trajectories we apply K-means to trajectory information to categorize trajectory types. K-means is an unsupervised algorithm that partitions a set

of observations in k types. The general goal of K-means is to take a set of observations, cluster them in k types such that the within-cluster variance is minimized. For our eddy trajectories, we have a set of N trajectories ($\{\mathbf{t_1}, \mathbf{t_2}, \ldots, \mathbf{t_N}\}$) to be clustered. For each trajectory we we quantify 6 track features for every trajectory: 1. the standard deviation of rotational velocity ($\sigma(U_\epsilon)$), 2. the average translation speed throughout the track ($\overline{c_\epsilon}$), 3. the standard deviation of translation speed throughout the track ($\sigma(c_\epsilon)$), 4. the starting cross-shore position of the track (x_0), 5. the track duration (T_ϵ), and 6. the average advective nonlinearity throughout the track ($\overline{n_\epsilon}$). This results in each trajectory in the set ($\mathbf{t_i}$) to be a one-dimensional vector with length of 6, associated with the 6 trajectory features. A larger set of trajectory features was tested and this subset of 6 features was chosen to maximize cluster performance. Additionally, as we are interested in understanding low frequency surf-zone currents, we exclude short eddy tracks where $T_\epsilon < 5$ s ($2.5 \times T_p$). This allows the K-means algorithm to cluster types of trajectories associated with low frequency motions. The process of subsetting trajectory features and sensitivity of feature and algorithm choices, such as T_ϵ cutoff, to cluster assignment and performance is discussed further in Section 4.4.2.

To cluster our set of trajectories, we apply a standard K-means algorithm to $\{\mathbf{t_1}, \mathbf{t_2}, \ldots, \mathbf{t_N}\}$. The basic steps in this algorithm are:

1. Initialize k centroids

2. Assign every trajectory in $\{\mathbf{t_1}, \mathbf{t_2}, \ldots, \mathbf{t_N}\}$ to a cluster ($1 - k$)

3. Recalculate centroids from trajectories in each cluster

4. Iterate until centroids converge (i.e. no change between iterations)

This algorithm relies on providing the number of clusters to assign trajectories. As we do not know how many different types of eddy trajectories may exist we optimize the number of clusters through quantifying the silhouette score. The silhouette score is a

measure of how well observations within a cluster match their assigned cluster, compared to the other clusters. The silhouette score is computed as:

$$a(i) = \frac{1}{|C_I| - 1} \sum_{j \in C_I, i \neq j} D(i,j) \tag{4.13}$$

for every $i \in C_I$, where i is an observation in cluster C_I and $D(i,j)$ is a measure of the Euclidean distance between observation i and j. The silhouette score ranges between ± 1 and high scores denote a more optimal cluster configuration. To determine the optimal number of clusters for our data, we apply K-means to the trajectory dataset for varying number of clusters and compute silhouette score for each. The number of clusters associated with the highest silhouette score is then used for further analysis.

4.3 Results

4.3.1 Eddy trajectories

Application of the eddy tracking algorithm to 283,217 identified eddies over a 20 minute simulation resulted in 21,926 distinct eddy trajectories. Trajectories range in length from a single time step (dt $= 0.2$ s) to 9.3 minutes. As we are interested in eddies associated with low frequency ($f < 0.003$ Hz) surfzone currents, we focus analysis on longer trajectories and removed trajectories that are shorter than a couple of wave periods (less than 5 s long) and trajectories that start in the swash zone ($x > 32.5$ m). The total number of these longer trajectories is 1,933 tracks, consisting of 66% of the total number of identified eddies. Examination of animations of simulated vorticity with eddy boundaries and trajectory history overlaid (Fig. 4.2) provide confidence that the tracking algorithm is successful.

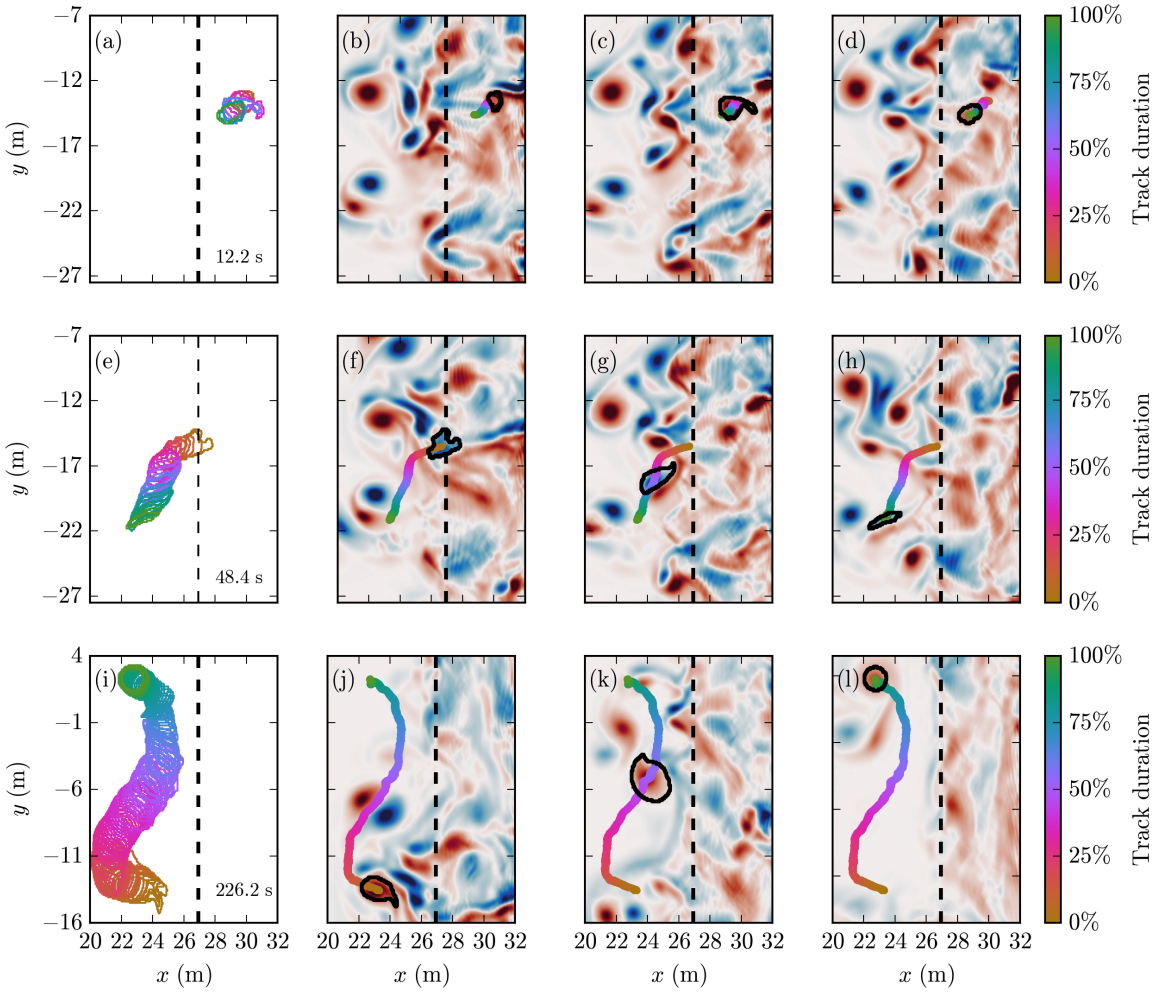

Figure 4.2: Three examples of (a,e,i) eddy boundaries for the entire track duration, (b,f,j) the initial eddy outline, (c,g,k) the eddy outline 50% of the way through the track duration, and (d,h,l) the final eddy outline. The initial, midpoint, and final eddy outlines are overlaid with vorticity at that timestep and the locations of the trajectory over the track duration. Colors of eddy outlines in (a,e,i) and trajectory history in (b,c,d,f,g,h,j,k,l) denote track duration percentage and are shown in colorbars. Track duration of each track are written in (a,e,i) in seconds. In all panels, dashed line denotes the surf-zone edge.

Eddy trajectories range in duration, location, and eddy characteristics. Some eddy tracks are short lived and can vary significantly in eddy size over their life cycle (Fig. 4.2a-d). These short lived eddy tracks tend to occur within the surf zone where background vorticity is strong and can influence the identified boundary of the eddy resulting in changes in eddy size and circulation changes. The eddy trajectory example shown in Fig. 4.2a-d starts within the surf zone, translates towards the surf-zone edge growing in size, then decreases in size and rotational strength (Fig. 4.3a,d), resulting in termination of the eddy track after 12.2 s. Over the life of this eddy track, the eddy translation speed is relatively constant with a decrease in speed towards the end of the track (Fig. 4.3g). The eddy is generally transiting offshore ($u_\epsilon < 0$) with a non-zero alongshore component of translation resulting in an angled translation offshore (Fig. 4.3j,m, 4.2a-d). The eddy in this track tends to stay linear ($n_\epsilon < 1$), but increases in nonlinearity as the eddy translation speed slows towards the end of the track (Fig. 4.3p).

Similar to the eddy within the surf zone, an example eddy near the surf-zone edge also exists in a field of relatively high background vorticity (Fig. 4.2e-h). This eddy track lasts longer than the example eddy trajectory that starts within the surf zone (Fig. 4.2). The eddy trajectory example shown in Fig. 4.2e-h lasts for 48.4 s, ending with smaller eddy size and weaker rotational speed (Fig. 4.3b,e). In the initial phase of the eddy trajectory (0 - 10 s), the eddy rotational speed increases while its size decreases (Fig. 4.3b,e). In the middle phase of the eddy trajectory (10 - 35 s), the eddy size remains relatively constant, but eddy rotational speed decreases in magnitude (Fig. 4.3b,e). In the final phase of the eddy trajectory (35 - 50 s), the eddy continues to decrease its rotational speed, but also decrease in size (Fig. 4.3b,e). While the eddy size and rotational speed changes over the eddy track, the eddy translation speed is relatively constant throughout the duration of the track, with slightly elevated speeds at both the beginning and end of the track (Fig. 4.3h). Similarly, the along and cross-shore components of eddy translation speed are also relatively constant, with mean offshore velocity and a slight non-zero alongshore velocity resulting in angled propagation of the eddy offshore (Fig. 4.2e-h, 4.3k,n). Throughout

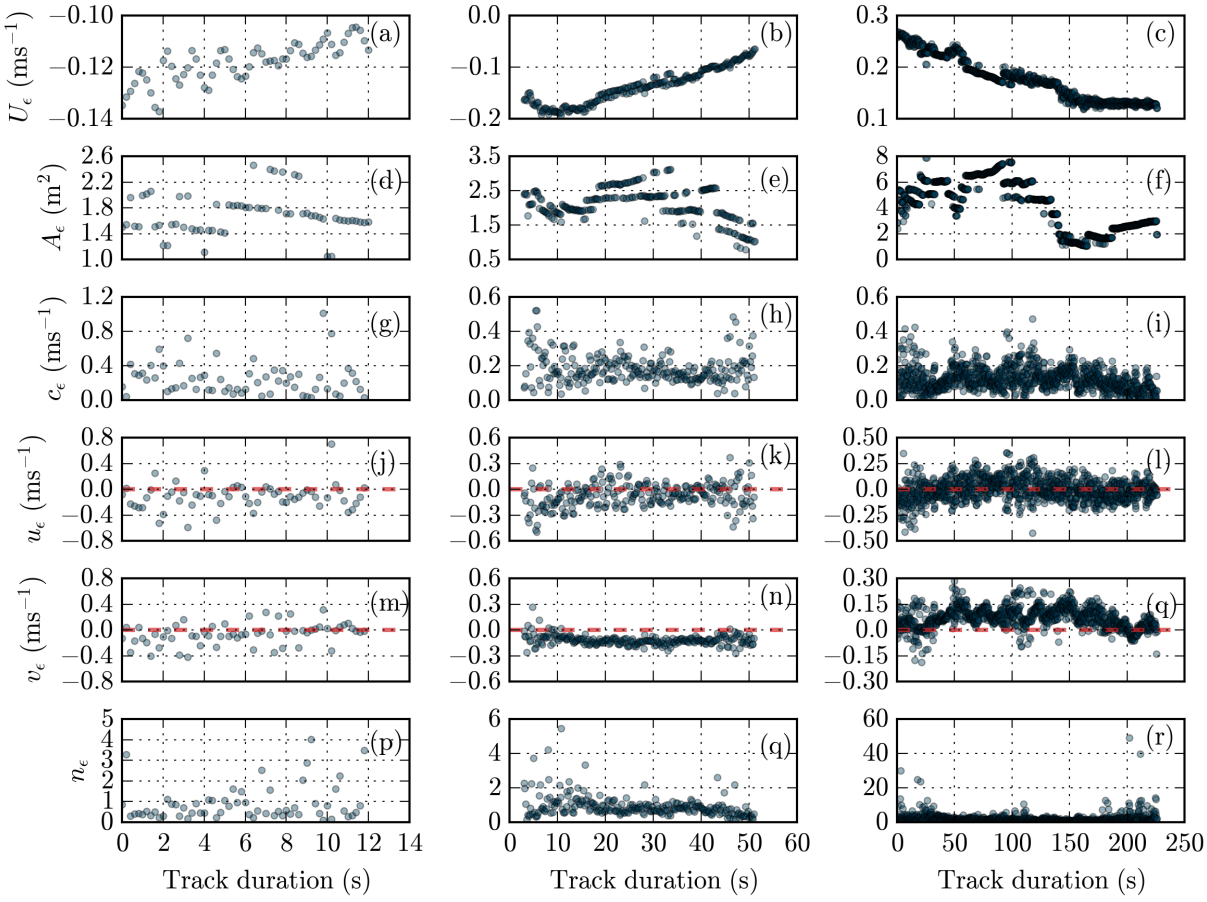

Figure 4.3: Eddy characteristics of (a-c) rotational velocity (U_ϵ), (d-f) eddy size (A_ϵ), (g-i) eddy translation speed (c_ϵ), (j-l) cross-shore eddy translation speed (u_ϵ) with $u_\epsilon < 0$ indicating offshore flow and $u_\epsilon > 0$ indicating onshore flow, (m-q) alongshore eddy translation speed (v_ϵ), and advective nonlinearity parameter (n_ϵ) over eddy track duration. Eddy characteristics in the first column (a,d,g,j,m,p) correspond to eddy track shown in (a-d) in Fig. 4.2. Eddy characteristics in the second column (b,e,h,k,n,q) correspond to eddy track shown in (e-h) in Fig. 4.2. Eddy characteristics in the third column (c,f,i,l,q,r) correspond to eddy track shown in (i-l) in Fig. 4.2.

the track duration, the eddy nonlinearity hovers near 1, but the eddy tends to be more nonlinear at the beginning of the track, when the magnitude of eddy rotational speed is largest (Fig. 4.3q).

Offshore of the surf zone, our example eddy trajectory is longer lived (Fig. 4.4a) and experiences relatively lower background vorticity (Fig. 4.2i-l) than the prior examples. The eddy trajectory example shown in Fig. 4.2i-l lasts for 226.2 s. Compared with the prior two eddy trajectory examples, this eddy is larger in size and rotational speed (Fig. 4.3c,f). Similar to both other eddy tracks, the rotational speed tends to decrease in magnitude over the track duration (Fig. 4.3c). Eddy size over the track duration varies greatly throughout the track, from 0 - 100 s the eddy size is relatively constant, but between 100 - 150 s the eddy size decreases rapidly (by $\sim$6 m^2), and then remains relatively constant with slight growth in eddy size from 150 s to the end of the track (Fig. 4.3f). The eddy translation speed is variable over the duration, but tends to remain relatively constant with a decrease in speed near the end of the track (Fig. 4.3i). In contrast with the other two eddy tracks, the cross-shore component of eddy translation speed oscillates between offshore and onshore velocity throughout the track duration and the alongshore component of eddy translation speed is non-zero resulting in strong alongshore translation of the eddy over its lifetime (Fig. 4.2i-l, 4.3l,q). While most of the time the eddy nonlinearity stays below 1.5, eddy nonlinearity is an order of magnitude larger than the other eddy tracks near the beginning and end of the eddy track (Fig. 4.3r).

4.3.2 Cross-shore variation

The example eddy trajectories shown in Fig. 4.2, 4.3 highlight variation that can exist between individual eddy trajectories. Here we consider the full eddy trajectory dataset and investigate median properties as a function of cross-shore position. Median eddy properties are computed as a function of instantaneous cross-shore position for rotational velocity and translation speeds (Fig. 4.4b-e). In addition, the median trajectory duration is presented as function of cross-shore starting location of the trajectory (Fig. 4.4a).

We find that trajectory duration tends to be shorter for eddies that start in the surf zone than for eddies that start farther offshore, with a sharp increase in trajectory duration

from the surf-zone edge ($x = 26.9$ m) to 24.2 m ($1.5W_{sz}$) (Fig. 4.4a). We find that the median rotational speed tends to decrease from the surf zone moving offshore, with some local variation in the surf zone (Fig. 4.4b). Additionally, median eddy translation speed decreases from the surf zone moving offshore, but exhibits a local maximum near the bar crest ($x \simeq 28$ m) and a local minimum in the trough ($x \simeq 29.7$ m) (Fig. 4.4c). The signed cross-shore component of eddy translation speed has relatively constant weak offshore translation from the surf zone to far offshore (Fig. 4.4d). The magnitude of the alongshore component of eddy translation speed decreases to near zero moving offshore (Fig. 4.4e). However, in the surf zone, the direction of eddy translation varies with cross-shore position and the magnitude of both along and cross-shore components of translation is larger than offshore.

In the inner surf ($x > 29.7$ m, onshore of dash-dotted line in Fig. 4.4d), eddy translation is offshore with strong alongshore contribution near the shoreline but decreasing alongshore translation near the edge of the inner surf zone. Near the transition between inner and outer surf ($x = 29.7$ m), the offshore component of eddy translation decreases, indicating that eddies may be stalling in the trough or that on average in the eddy field eddies are nearly as likely to move onshore as offshore (Fig. 4.4d,e). In the outer surf, magnitude of the alongshore component of translation remains relatively large and constant till the edge of the surf zone, where alongshore translation continues to decrease(Fig. 4.4e). Meanwhile the magnitude of the cross-shore component of eddy translation reaches its minimum in the middle of the outer surf, near $x \simeq = 28.5$ m and then reaches its maximum near the surf-zone edge (Fig. 4.4d).

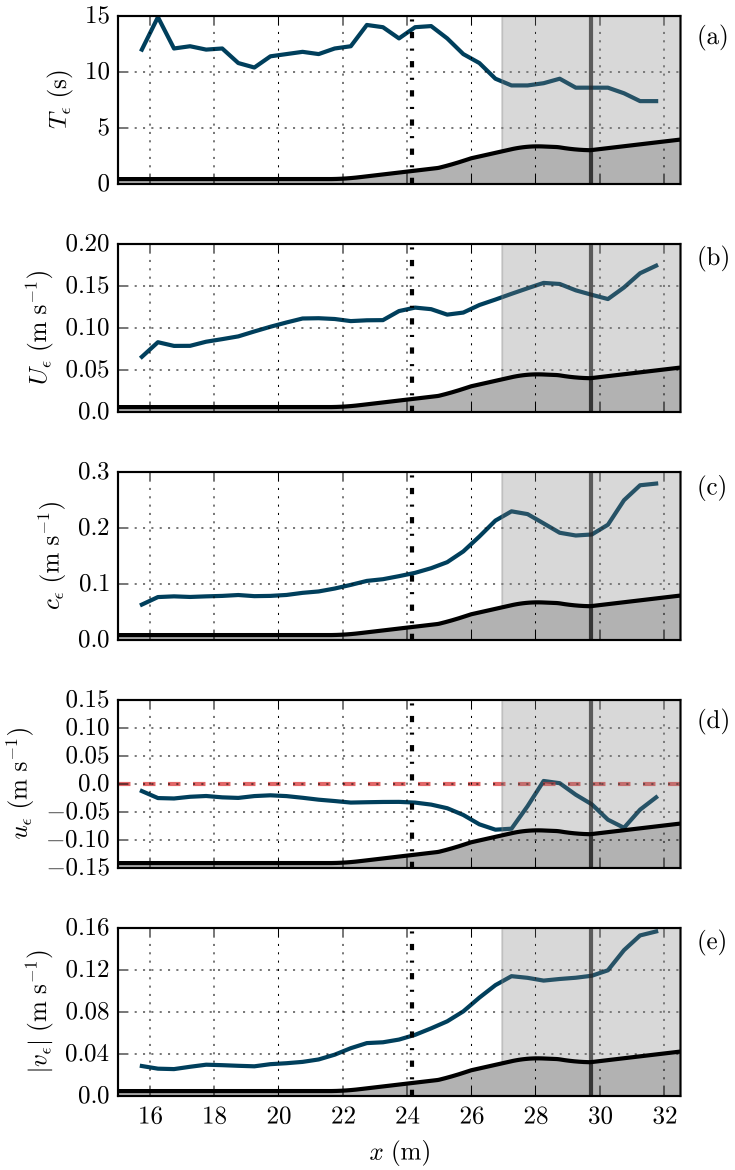

Figure 4.4: Cross-shore profiles of median (a) track duration (T_ϵ) as a function of trajectory starting location, (b) eddy rotational velocity (U_ϵ), (c) eddy translation speed (c_ϵ), (d) cross-shore eddy translation speed (u_ϵ) with $u_\epsilon < 0$ indicating offshore flow and $u_\epsilon > 0$ indicating onshore flow (u_ϵ = 0 noted with red dashed line), (e) alongshore eddy translation speed (v_ϵ). Model bathymetry is shown at the bottom of each panel for reference (not to scale) with solid black line and grey shading. Light grey shading denotes the surf zone, solid vertical line denoting the transition from inner to outer surf zone ($0.5W_{sz}$), and dash-dotted vertical line denoting the edge of the offshore surf zone region ($1.5W_{sz}$).

4.3.3 *Application of K-means to eddy trajectories*

To cluster trajectories into subsets of trajectories with similar behavior, characteristics of each trajectory were compiled and then input to a K-means clustering algorithm. These characteristics included standard deviation of rotational velocity ($\sigma(U_\epsilon)$), mean translation speed ($\overline{c_\epsilon}$), standard deviation of translation speed ($\sigma(c_\epsilon)$), starting cross-shore position (x_0), track duration (T_ϵ), and mean advective nonlinearity ($\overline{n_\epsilon}$). K-means was applied for a range of 2 - 40 clusters and silhouette score was quantified for each different number of clusters. The maximum silhouette score was 0.32 and associated with 3 clusters, with slightly lower score for 2 clusters, and decreasing score for higher numbers of clusters (Fig. 4.5a).

Eddy characteristics by cluster type

These 3 clusters can be visualized in PCA space, where each trajectory is mapped onto a location as a function of the two dominant PCA components (Fig. 4.5b). The top PCA component, PCA 1, explains 47% of the variance of trajectory features across all tracks with $\sigma(U_\epsilon)$, $\overline{c_\epsilon}$, $\sigma(c_\epsilon)$, and x_0 being the dominant coefficients (Fig. 4.5c). The second PCA component, PCA 2, explains 23% of the variance of the dataset and has $\sigma(U_\epsilon)$, T_ϵ, and $\overline{n_\epsilon}$ as the dominant coefficients (Fig. 4.5d). Mapping each trajectory onto PCA space indicates some differences in trajectory characteristics between these 3 clusters, which we will refer to as; cluster 1 (surf zone cluster), cluster 2 (offshore cluster), and cluster 3 (long lived cluster). Centroids for cluster 1 (pink) and cluster 2 (blue) are similar for PCA 2, whereas cluster 3 (yellow) is more distinct (Fig. 4.5b). For PCA 1, cluster 2 and cluster 3 have similar centroids and cluster 1 is distinct from the other two (Fig. 4.5b).

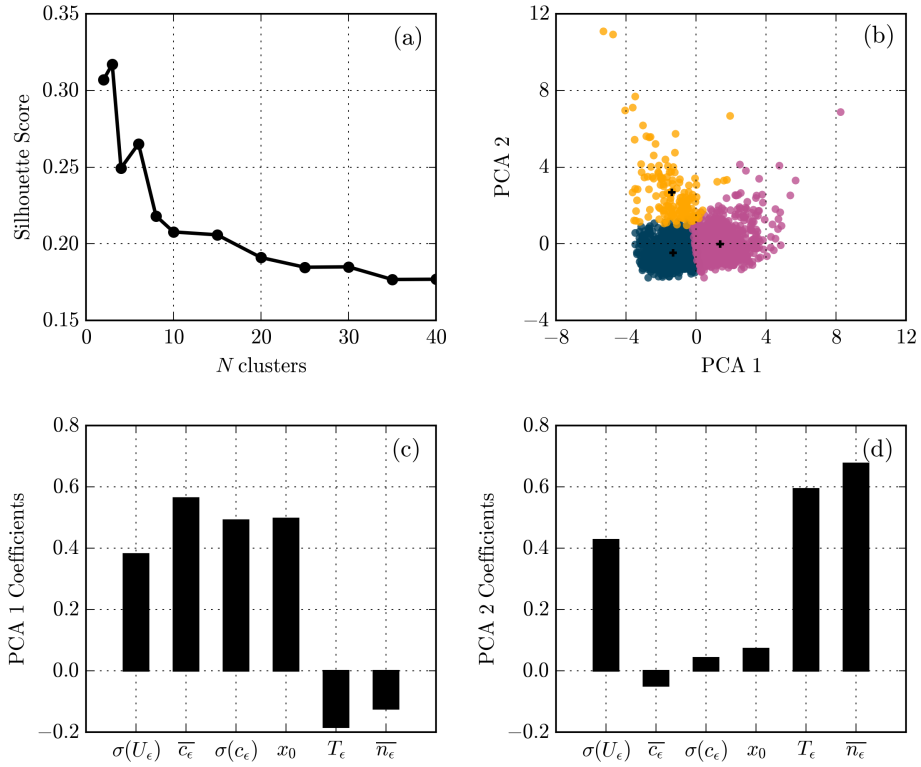

Figure 4.5: (a) Silhouette score for varying numbers of clusters. (b) Scatterplot of trajectories plotted along the largest two principle components, PCA 1 and PCA 2. Trajectories in the scatterplot are colored by cluster with cluster 1 shown in pink, cluster 2 shown in blue, and cluster 3 shown in yellow. Centroids of each cluster are noted by black plus sign (+). (c) PCA 1 coefficients and (d) PCA 2 coefficients showing relative contribution of trajectory characteristics to each PCA component. Trajectory characteristics are standard deviation of rotational velocity ($\sigma(U_\epsilon)$), mean eddy translation speed ($\overline{c_\epsilon}$), standard deviation of eddy translation speed ($\sigma(c_\epsilon)$), starting cross-shore location (x_0), track duration (T_ϵ), and mean advective nonlinearity parameter ($\overline{n_\epsilon}$) indicated on figure with notation.

To examine how these eddy track characteristics vary between each cluster we compare probability density functions of the 6 eddy track features split by cluster type. Cluster 1 (surf zone cluster) is characterized by a larger standard deviation in rotational velocity (median $\sigma(U) = 2.2$ cm s^{-1}), but has a relatively low average advective nonlinearity

(median $\overline{n_\epsilon}$ = 0.9) (Fig. 4.6a,f). Eddies in cluster 1 have the fastest translation speeds (median $\overline{c_\epsilon}$ = 0.28 m s^{-1}) and larger variation in translation speed (median $\sigma(c_\epsilon)$ 0.22 m s^{-1}) (Fig. 4.6b,c). Trajectories in cluster 1 tend to start within the surf zone (median x = 28.6 m), our reasoning for the shorthand 'surf zone cluster' to refer to this group. The tracks in this cluster are relatively short lived (median track duration 8.6 s) (Fig. 4.6d,e).

Cluster 2 (offshore cluster) is characterized by a smaller standard deviation in rotational velocity (median $\sigma(U)$ = 0.6 cm s^{-1}) and lower average advective nonlinearity (median $\overline{n_\epsilon}$ = 0.9) (Fig. 4.6a,f). Eddies in cluster 2 translate at a slower speed (median $\overline{c_\epsilon}$ = 0.13 m s^{-1}) and have smaller variation in translation speed (median $\sigma(c_\epsilon)$ 0.09 m s^{-1}) (Fig. 4.6b,c). Trajectories in cluster 2 range in start locations, but tend to start further offshore (median x = 24.3 m), hence referring to this as the 'offshore cluster' (Fig. 4.6d. Additionally, trajectories tend to be slightly longer in duration than cluster 1 with median track duration of 10.6 s (Fig. 4.6e).

Similar to cluster 2, trajectories from cluster 3 (long lived cluster) start further offshore (median x = 24.6 m) and have slower translation speeds (median $\overline{c_\epsilon}$ = 0.14 m s^{-1}) and standard deviation in translation speeds (median $\sigma(c_\epsilon)$ 0.12 m s^{-1}) (Fig. 4.6b,c,d). The distribution of the rotational velocity standard deviation for cluster 3 is similar to cluster 1, with median $\sigma(U)$ = 2.2 cm s^{-1}, which is larger than that for cluster 2 (Fig. 4.6a). While these trajectory characteristics are similar to the two other clusters, track duration and advective nonlinearity show a distinct difference. Track duration is significantly longer, hence referring to this as the 'long lived cluster,' with a range of durations from 5.4 s to 9.9 min (note that pdf shown in Fig. 4.6e is cut off at 2 min) and median of 55.8 s (Fig. 4.6e). Additionally, the median advective nonlinearity is 2.4, which is larger for cluster 3 compared to the other two clusters (Fig. 4.6f).

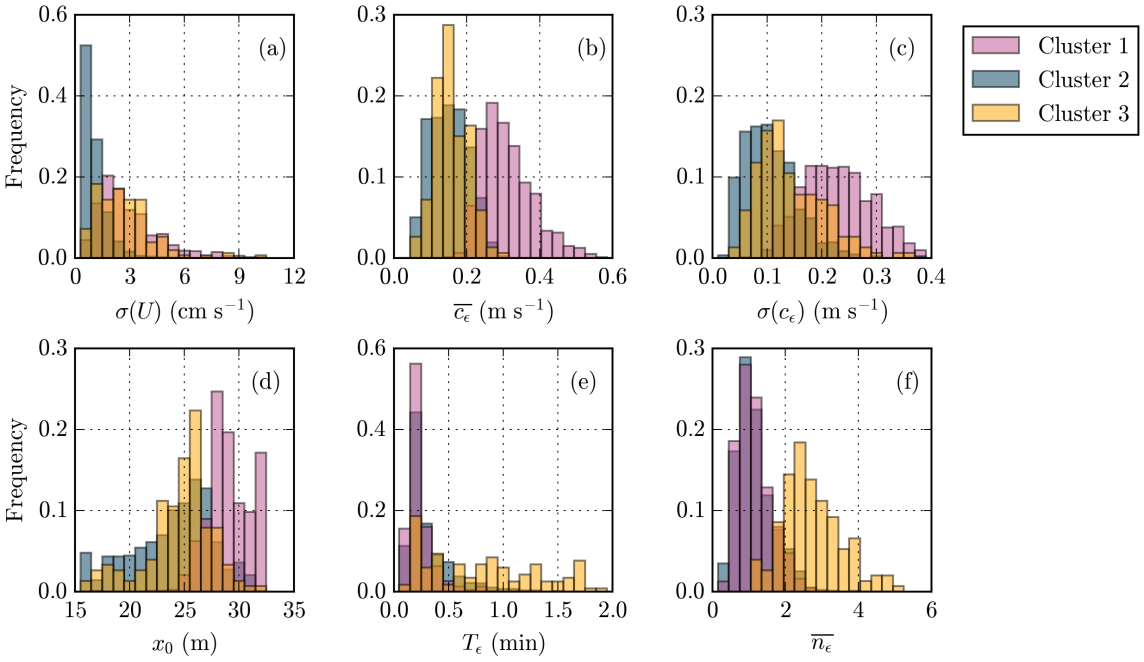

Figure 4.6: Probability density functions of eddy trajectory characteristics (a) standard deviation of rotational velocity ($\sigma(U_\epsilon)$), (b) mean eddy translation speed ($\overline{c_\epsilon}$), (c) standard deviation of eddy translation speed ($\sigma(c_\epsilon)$), (d) starting cross-shore location (x_0), (e) track duration (T_ϵ), and (f) mean advective nonlinearity parameter ($\overline{n_\epsilon}$) colored by cluster type, colors in legend.

In plan view, eddy trajectories traverse the entire surf zone and can persist far offshore (Fig. 4.7a). Eddy trajectories within the surf zone appear shorter and patchy in space (see onshore of white dashed line in Fig. 4.7a). Near the edge of the surf zone, the density of eddy trajectories is high and eddy tracks appear to cover nearly the entire area ($x \simeq$ 24 - 27 m in Fig. 4.7). Far offshore ($x < 23$ m), eddy trajectories are long, but sparse in space with localized areas of higher density of tracks. When broken out by cluster, eddy trajectories within the surf zone tend to be associated with cluster 1 (surf zone cluster), while eddy trajectories that start offshore of the surf zone tend to be associated with cluster 2 (offshore cluster) and 3 (long lived cluster) (Fig. 4.7b-d). Consistent with longer duration tracks (Fig. 4.6e), track lengths in cluster 3 appear significantly longer in space,

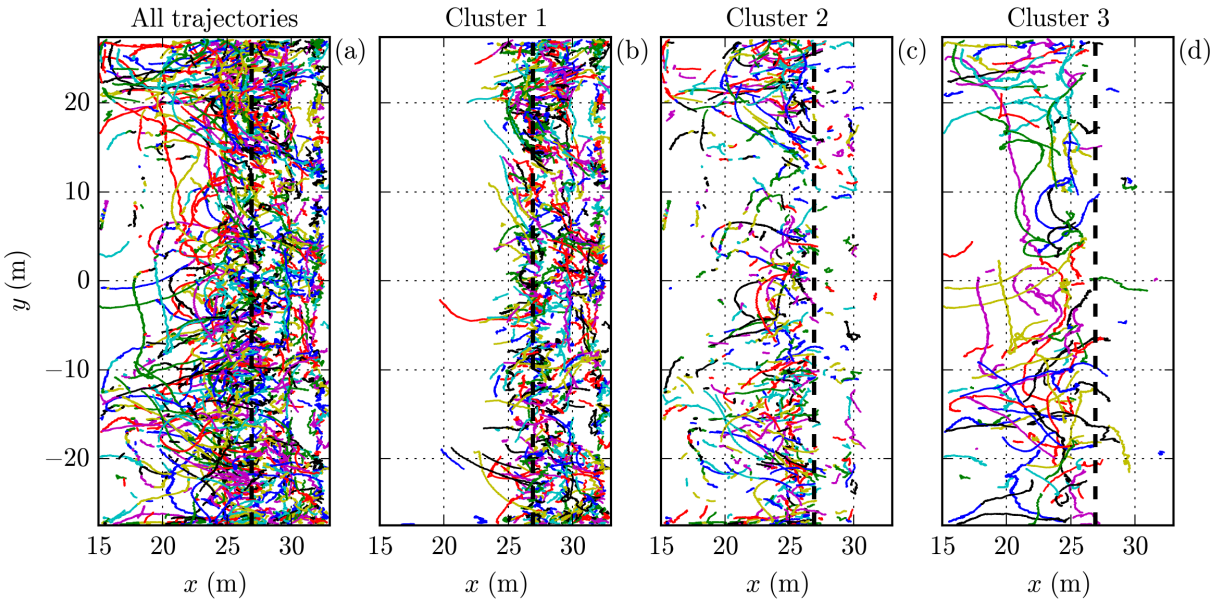

Figure 4.7: Planar view of (a) all eddy trajectories with a track duration of at least 5 seconds used in K-means clustering algorithm (tracks assigned random colors). Eddy trajectories in (b) cluster 1, (c) cluster 2, and (d) cluster 3. surf-zone edge is denoted by white dashed line and colored contours show model bathymetry.

sometimes spanning from the surf-zone edge to the model boundary (Fig. 4.7d).

Cross-shore variation by cluster type

Similar to Fig. 4.4, we examine cross-shore variation by cluster type by computing median eddy properties as a function of instantaneous cross-shore position for rotational velocity and translation speeds (Fig. 4.8b-e). In addition, the median trajectory duration is presented as function of cross-shore starting location of the trajectory (Fig. 4.8a). Since the number of trajectories varies by cluster (i.e. few trajectories offshore for cluster 1), we compute median characteristics only for locations where there is at least 5 trajectories that start in that cross-shore region.

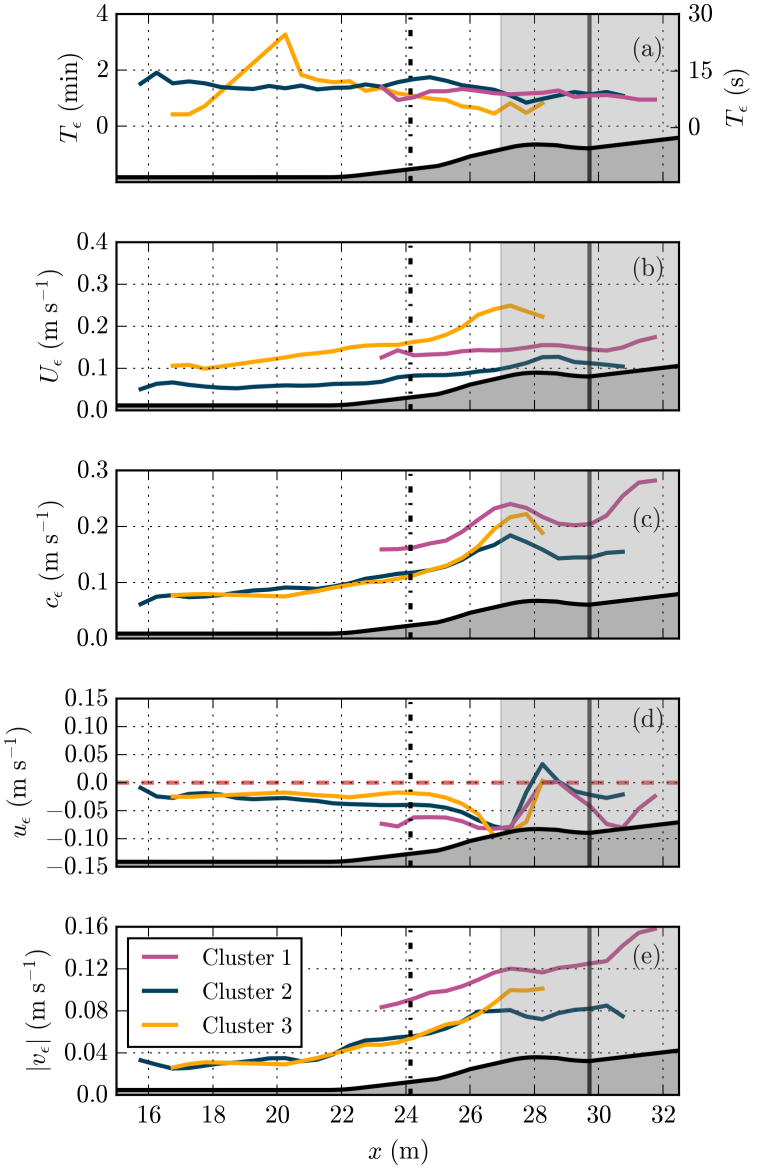

Figure 4.8: Cross-shore profile of median (a) track duration (T_ϵ) of trajectories as a function of start location (note that cluster 1 (pink) and 2 (blue) are plotted on right y-axis in seconds, and cluster 3 (yellow) is plotted on left y-axis in minutes), (b) eddy translation speed (c_ϵ), (c) eddy rotational velocity (U_ϵ), (d) cross-shore eddy translation speed (u_ϵ) with $u_\epsilon < 0$ indicating offshore flow and $u_\epsilon > 0$ indicating onshore flow, (e) alongshore eddy translation speed (v_ϵ) for each cluster with cluster type denoted by color (colors in legend in (e)). Model bathymetry is shown at the bottom of each panel for reference (not to scale) with solid black line and grey shading. Light grey shading denotes the surf zone, solid vertical line denoting the transition from inner to outer surf zone ($0.5W_{sz}$), and dash-dotted vertical line denoting the edge of the offshore surf zone region ($1.5W_{sz}$).

Eddy rotational speed generally decreases from the surf zone moving offshore for all cluster types, with cluster 2 having the slowest speeds and cluster 3 having the fastest speeds (Fig. 4.8b). In cluster 3, the eddy rotational speed has local maxima near the edge of the surf zone. Additionally, cluster 2 also exhibits a slight increase in rotational speed from the inner surf to the bar crest before continually decreasing offshore (Fig. 4.8b).

For all clusters, eddy translation speed also generally decreases from the surf zone moving offshore with a local peak in translation speeds near the surf zone edge and bar crest ($x \simeq$28 m) and lower speeds in the trough ($x \simeq$ 29.7 m) and offshore (Fig. 4.8c). While the cross-shore trend is similar, the magnitude in translation speed varies between clusters with the fastest speeds for cluster 1 and similar speeds for cluster 2 and 3 across most cross-shore positions (Fig. 4.8c).

The cross-shore component of eddy translation speed follows a similar pattern for all cluster types with maximum cross-shore translation speed at the surf-zone edge and minimal cross-shore translation in the trough (Fig. 4.8d). The magnitude of cross-shore translation is similar between cluster 2 and 3 at all cross-shore positions. However, while cross-shore translation speeds are similar in the outer surf between all three cluster types, cluster 1 offshore speeds tends to be slightly larger in magnitude in the inner surf and offshore (Fig. 4.8d). The magnitude of alongshore translation speeds tend to decrease moving offshore for all clusters, but speeds are largest for cluster 1, particularly in the surf zone (Fig. 4.8e). While alongshore translation decreases offshore, all clusters exhibit relatively constant translation speeds in the outer surf, but similarly vary in magnitude with cluster 1 with the fastest speeds and cluster 2 with the slowest speeds (Fig. 4.8e).

The trend in track duration as a function of starting cross-shore position exhibits a more constant relationship for each cluster (Fig. 4.8a) compared to an increase in track duration with starting locations further offshore for all trajectories (Fig. 4.4a). However, there is a slight increase in duration offshore with cluster 1 and 2 track durations both hover around $\sim$ 10 s offshore and around $\sim$ 8 s in the surf zone (Fig. 4.8a). Additionally, it should be noted that cluster 3 has too few tracks within the surf zone, so this relationship

is only observed from the outer edge of the outer surf and offshore. Another notable feature between clusters is that cluster 3 has significantly longer track durations at all cross-shore locations with track duration hovering around 1 min across all locations (Fig. 4.8a)

4.3.4 Eddy life cycles

Eddy characteristics vary over the duration of the trajectory (Fig. 4.3) and eddy characteristics vary between clusters (Fig. 4.6), so we explore how eddy life cycles vary for all trajectories and between clusters. Median eddy life cycles are computed from duration-normalized eddy trajectory characteristics for all trajectories and for trajectories in each cluster (Fig. 4.9). For all trajectories (black dashed line in Fig. 4.9a), the magnitude of eddy circulation increases during the initial stage of the trajectory. Following this increase, eddy circulation decreases over the rest of the track duration (black dashed line in Fig. 4.9a). However, this trend does not hold for individual clusters. Cluster 1 exhibits the same increasing phase followed by a decreasing phase, but cluster 2 and 3 start at maximum values and decrease over the duration of the track (Fig. 4.9a). The median circulation magnitude decreases by 27% over the track duration for cluster 2, whereas for cluster 3 this quantity decreases in circulation magnitude by 49%.

Similar to circulation, the median life cycle for all trajectories shows that eddies tend to exhibit an increase in size during the initial phase, reach a maximum size, then gradually decrease in size to the end of the track (black dashed line in Fig. 4.9b). This trend in size over track duration is also observed in trajectories in cluster 1, whereas eddy size remains constant and then decreases near the end of the track for both cluster 2 and 3 (Fig. 4.9b). Eddy sizes are similar between cluster 1 and 2 with median size over the eddy life 1.7 and 1.4 m^2 for cluster 1 and 2 respectively. Eddy size for cluster 3 is $\sim$2 times larger (median 3 m^2) and exhibits a 46% decrease in size over the trajectory duration, compared with 12 and 27% decrease for cluster 1 and 2 respectively.

While there are large changes in circulation and eddy size over track duration, the water depth that eddies experience also changes and may influence these characteristics through conservation of potential vorticity (*Bühler and Jacobson*, 2001). For all trajectories, potential vorticity (PV_ϵ), as measured by $\frac{\Gamma_\epsilon}{A_\epsilon h}$ is computed throughout the track duration. Each PV_ϵ is normalized by its median value to allow for comparison between clusters. For all trajectories, median normalized potential vorticity ($\langle PV_\epsilon \rangle$) over the trajectory duration decreases slowly with an 11% decrease over the track duration (black dashed line in Fig. 4.9c). Normalized potential vorticity for cluster 1 also slowly decreases with an 14% change from the beginning of the track to the end of the track (Fig. 4.9c). For cluster 2, $\langle PV_\epsilon \rangle$ over the trajectory duration decreases slowly over the track duration (8% decrease); however, for cluster 3, $\langle PV_\epsilon \rangle$ decreases rapidly, then decreases at a similar rate as cluster 1 and 2 resulting in a 22% decrease over the track duration (Fig. 4.9c).

Eddy translation speed for all trajectories and each cluster type is relatively constant over time, with a slight decrease over the track duration (Fig. 4.9d). Eddy translation speed is fastest for cluster 1 (median 0.24 m s^{-1}) and slowest for clusters 2 and 3 (median 0.11, 0.11 m s^{-1}). While the total eddy translation speed is relatively constant over time, the along and cross-shore components of eddy translation vary over the track duration (Fig. 4.9d). Median cross-shore eddy translation is offshore directed throughout the entire track duration for all trajectories and cluster types; however, the strength and decrease in offshore speed varies (Fig. 4.9d). The strength of offshore translation weakens over the entire track duration and for cluster 2 and 3 this trend corresponds to a 32 and 81% weakening respectively (Fig. 4.9d). In contrast, offshore translation remains relatively constant with a slight (15%) weakening, over entire track duration for trajectories in cluster 1 (Fig. 4.9d). The magnitude of the alongshore component of eddy translation follows the same trend as total eddy translation speed, with relatively constant alongshore speed over time; however, speeds are slightly elevated at the beginning of the track and then decrease to a relatively constant value. Additionally, the magnitude of alongshore translation speeds is largest for cluster 1 and smaller for cluster 2 and 3 (Fig. 4.9d).

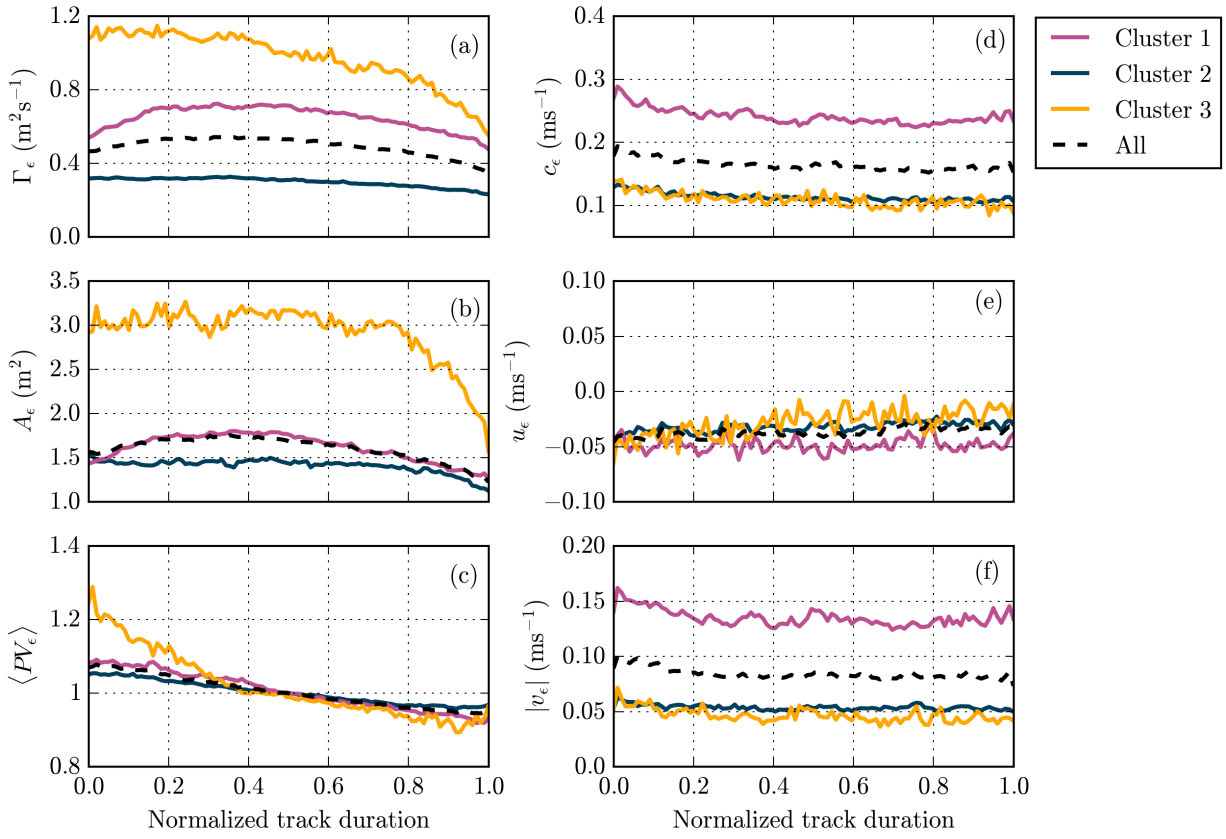

Figure 4.9: Normalized median eddy life cycles of (a) magnitude of eddy circulation (Γ_ϵ), (b) eddy size (A_ϵ), and (c) normalized potential vorticity ($PV_\epsilon = \frac{\Gamma_\epsilon}{A_\epsilon h}$, normalized by median PV_ϵ for each eddy track), (d) eddy translation speed (c_ϵ), (e) cross-shore eddy translation speed (u_ϵ), and (f) magnitude of alongshore eddy translation speed ($|v_\epsilon|$) over all eddy trajectories greater than 5 s (dashed black line) and over each cluster (solid colored lines, colors in legend).

4.4 Discussion

4.4.1 Eddy trajectories

Identification of coherent vortices, or eddies, provides a unique perspective to characterize surf-zone vorticity that complements existing spectral estimates of energy and spatial scales of vorticity in the surf zone *Nuss, Emma et al.* (a). Our application of a tracking

method characterizes the time variation and spatial movement of these eddies. These eddy trajectories show that surf-zone eddies can vary significantly in their characteristics, both between different eddy trajectories and over an individual track duration. With $O(10^3 - 10^4)$ tracks made up of $O(10^5)$ eddies, manually determining patterns and similarities between trajectories is difficult. Application of the unsupervised clustering algorithm, K-means, is an excellent tool for discerning distinctive types of trajectories.

4.4.2 Trajectory clustering

The first step in the trajectory clustering process is determining what information about each trajectory to feed into the K-means algorithm. Initially, 12 different trajectory features were quantified from eddy size (mean, change over track duration, and standard deviation), rotational speed (mean, change over track duration, and standard deviation), translation speed (mean and standard deviation), direction (mean and standard deviation), start location, and track duration. These 12 features quantify important characteristics of each eddy trajectory and were fed into the K-means algorithm and found to have a lower maximum silhouette score (~ 0.2) for 2 clusters, compared with the 3 clusters analyzed here (0.31) determined by the 6 trajectory features described in Section 4.2.5. The 2 clusters determined by using all 12 features were similar to the clusters we have presented here, but with cluster 2 and 3 combined rather than split.

Starting with the full set of 12 trajectory features, we iterated and removed features that minimally contributed to cluster assignment and maximized the silhouette score. Throughout the iteration process, the number of clusters mostly varied between 2 and 3 clusters, with either 3 clusters similar to the current cluster types or 2 clusters with cluster 2 and 3 combined. This consistency between different combinations of features suggests that with information about the eddy size, rotational speed, translation speed, direction, start location, and track duration these clusters are robust. Inclusion of other eddy trajectory features may result in variation of cluster assignment, but as these features

are fundamental to our understanding of characterizing eddy variation and of interest to our science questions, future work can explore if different trajectory features would provide a new perspective on clustering trajectory types.

In addition to inclusion of trajectory features, sensitivity to the number of trajectories included in the K-means algorithm was also tested. We applied K-means to all trajectories of at least a certain track duration, but varied the duration threshold. Similar to the feature inclusion testing, the ideal number of clusters switched between 2 and 3. When there were only 2 clusters, the clusters were similar to our cluster 1, 2, and 3, but with a combined cluster 2 and 3 (i.e. offshore and long-lived trajectories were combined). Similarity of cluster types, suggests that exclusion of short lived eddies does not substantially change cluster assignment. Additionally, we tested the sensitivity to alongshore location by subsampling the full set of eddy trajectories to only trajectories that occurred within a certain alongshore range and cluster assignments varied minimally compared to inclusion of trajectories throughout the entire model domain.

Testing of clustering performance suggests that cluster assignment is robust and characterizes distinct types of trajectories. While a silhouette score of ~ 0.3 is relatively low, compared to maximum value of 1 (*Pauletic et al.*, 2019). However, the minimal sensitivity to K-means input variation provides confidence in cluster assignment. Additionally, the use of high dimensions of data (6 features) does limit the silhouette score, which is based on distance metrics. Euclidean distances in high dimensions are much larger than in lower dimensions and thus make metrics such as silhouette scores decrease in higher dimensions. This was observed during sensitivity testing where the silhouette score tended to increase with a smaller number of features included, despite cluster assignment varying minimally.

4.4.3 *Cluster 1: surf-zone trajectories*

A key defining characteristic of cluster 1 is that trajectories typically start in the surf zone and end within the surf zone or near the surf-zone edge. The trajectories have a larger median translation speed and a larger variation in translation speed over the track duration than the other clusters (Fig. 4.6b,c). Eddy trajectories in the surf zone experience stronger background vorticity, close proximity to other eddies, and actively breaking waves. While not explicitly quantified or explored in this paper, the stronger background currents in the surf zone likely act to advect eddies faster than eddy trajectories offshore, where there is little background vorticity.

Interaction with breaking waves likely impacts eddy characteristics and translation. Short-crested breaking waves generate signed vorticity near crest ends (*Peregrine*, 1998; *Spydell and Feddersen*, 2009; *Clark et al.*, 2012) and within individual wave crests (*Nuss, Emma et al.*, b; *Baker, Christine et al.*). As these short-crested wave break and generate vorticity, new vorticity is generated with existing vorticity in its proximity. Oscillations in rotational speed are observed at approximately 2 s period in some trajectories (Fig. 4.3a), consistent with the wave peak period, suggesting that eddy characteristics may vary due to interaction with the wave field and short-crested wave breaking vorticity generation. However, further work explicitly exploring eddy-wave interaction is needed.

In addition to changes in rotational speed, wave breaking and background surf-zone currents may also impact eddy translation speed and direction. Stronger background currents may account for higher average translation speeds (Fig. 4.6b, 4.9d). Similar to rotational speed, cross-shore translation speed can exhibit oscillations at $\sim$2-s periods (Fig. 4.3j), which may be associated with passing waves acting to advect the eddy shoreward in the wave crest and seaward in the trough on top of the mean eddy propagation.

While eddy rotational speeds are larger for these surf-zone trajectories, their fast translation speeds make these eddies relatively linear. More nonlinear eddies have a greater potential for material transport due to fast rotational speed that can cause tracers

to get caught in the eddy or slow translation speeds so that tracers within the eddy can stay within the eddy as it translates (*Chelton et al.*, 2011a; *Wekerle et al.*, 2020).

Eddy trajectories on barred bathymetry

Tracking of eddies through space and time provides a unique perspective of how coherent surf-zone vorticity evolves through the surf zone leading to offshore flow. Eddy trajectories span a wide range of durations, but tend to be shorter lived in the surf zone compared with offshore (Fig. 4.4a), where background vorticity is larger and more spatially variable (compare vorticity in surf zone with offshore of dashed back line in Fig. 4.2). Within the surf zone, these shorter lived eddy tracks have higher translation speed and rotational velocity compared with offshore, but also exhibit a relationship with local bathymetry (Fig. 4.4b,c). Eddy translation speed and rotational velocity both decrease moving into deeper water and increase in shallower water, meaning that eddies slow down in the trough and speed up over the bar crest.

In addition to slower translation speeds, eddies exhibit strong alongshore translation speeds and weakening offshore translation speeds in the trough (Fig. 4.4d,e). This reduction in offshore translation speed in the trough is consistent with expectations of mutual advection of vortices on a barred beach *Bühler and Jacobson* (2001). From conservation of potential vorticity and vortex pair interactions, mutual advection of a vortex pair is expected to be inversely proportional to water depth, leading to efficient movement of eddies into deeper water and also reducing their separation distance. However, when the eddy pair encounters the bar, the reduction in water depth leads to a separation between the vortex pair in the alongshore direction and a reduction in offshore speed *Bühler and Jacobson* (2001). If eddy strength is also weakened through dissipation from bottom friction or other processes, increased vortex pair separation may lead to no offshore movement out of the trough.

While across all eddy trajectories, potential vorticity is generally conserved, there

is a slight loss of potential vorticity over the track duration (Fig. 4.9c). This decrease in potential vorticity may be due to loss due to bottom friction; however, eddies also encounter other eddies, mean currents, and breaking waves. Further investigation of how individual eddies interact with surrounding conditions is crucial. Additionally, while median normalized potential vorticity over a large number of eddy trajectories shows relative conservation, some individual eddy trajectories exhibit more variability than the median profile. Variability in potential vorticity conservation and interactions with surrounding surf-zone conditions may be related and worth future study.

4.4.4 Cluster 2: offshore trajectories

A defining characteristic of cluster 2 is that most eddy tracks begin near the edge of the surf zone or further offshore (Fig. 4.7c). These eddy tracks tend to be longer lived than the surf-zone trajectories, with median duration of 10.6 s. Compared with the surf zone eddy tracks, these eddies move at slower speeds with smaller variation in translation speed throughout the track duration (Fig. 4.6b,c, 4.8c). Despite lower translation speeds, eddy rotational speed is also lower (Fig. 4.8b) resulting in relatively linear eddies (Fig. 4.6f), suggesting low tracer transport potential. Similar to surf zone trajectories, eddy tracks in cluster 2 change their size and circulation through changing water depth to generally conserve potential vorticity (Fig. 4.9c).

4.4.5 Cluster 3: long lived trajectories

Similar to cluster 2, cluster 3 eddy trajectories tend to start offshore near the surf-zone edge (Fig. 4.7d). Instead the defining characteristic of these eddy tracks is that tracks last significantly longer than both surf zone and offshore clusters (median 56 s, compared with 8.6 and 10.6 s, Fig. 4.6e). Similar to the offshore cluster, eddy trajectories translate at a slower speed and have smaller variation in speed compared with surf zone trajectories. However, these long lives eddy trajectories have larger rotational speed as well (Fig.

4.8b), resulting in more nonlinear eddies (Fig. 4.6f) suggesting greater potential for tracer transport. In contrast to the other clusters, potential vorticity is not conserved over the track duration (Fig. 4.9c). Potential vorticity drops by 20% in the first phase of the eddy life cycle (see yellow line from 0 to 0.4 in Fig. 4.9c), suggesting that more than frictional loss is occurring. The initial phase of many of the trajectories in this cluster begin near the surf zone edge. This region is characterized by a local peak in cross-shore translation speeds (Fig. 4.8d). These increased speeds, which may be associated with ejection events, may translate eddies into deeper water faster than their eddy characteristics can change, leading to a large loss in potential vorticity. In the later phase, potential vorticity decreases at a slower rate suggesting frictional losses may dominate farther offshore. However, characteristics and behavior of these long lived offshore eddy trajectories should be taken cautiously, particularly farther offshore. FUNWAVE-TVD is a depth-averaged model and therefore three-dimensionality of these eddies, offshore stratification, and vertical structure of offshore currents are not simulated. These effects would be better explored through fully three-dimensional simulations (*e.g.*, *Kumar and Feddersen*, 2017a; *Kirby and Derakhti*, 2019; *Baker et al.*, 2021).

4.4.6 Structure of an ejection event

Clustering of eddy trajectories has characterized types of eddy tracks throughout the surf zone and offshore. These clusters are associated with particular characteristics such as cross-shore locations, translation speeds, and track duration. However, it is not clear how these types of trajectories relate to tracer transport in offshore ejection events and increased cross-shore exchange velocities at the surf-zone edge. To explore how trajectory types related to ejection events and cross-shore exchange, we investigate one ejection event. This ejection event is characterized by an increased number of eddies and elevated exchange velocities, computed over 10 m in the alongshore (x = 17.5 - 27.5 m) at the surf-zone edge (x = 26.9 m), for several minutes (Fig. 4.10).

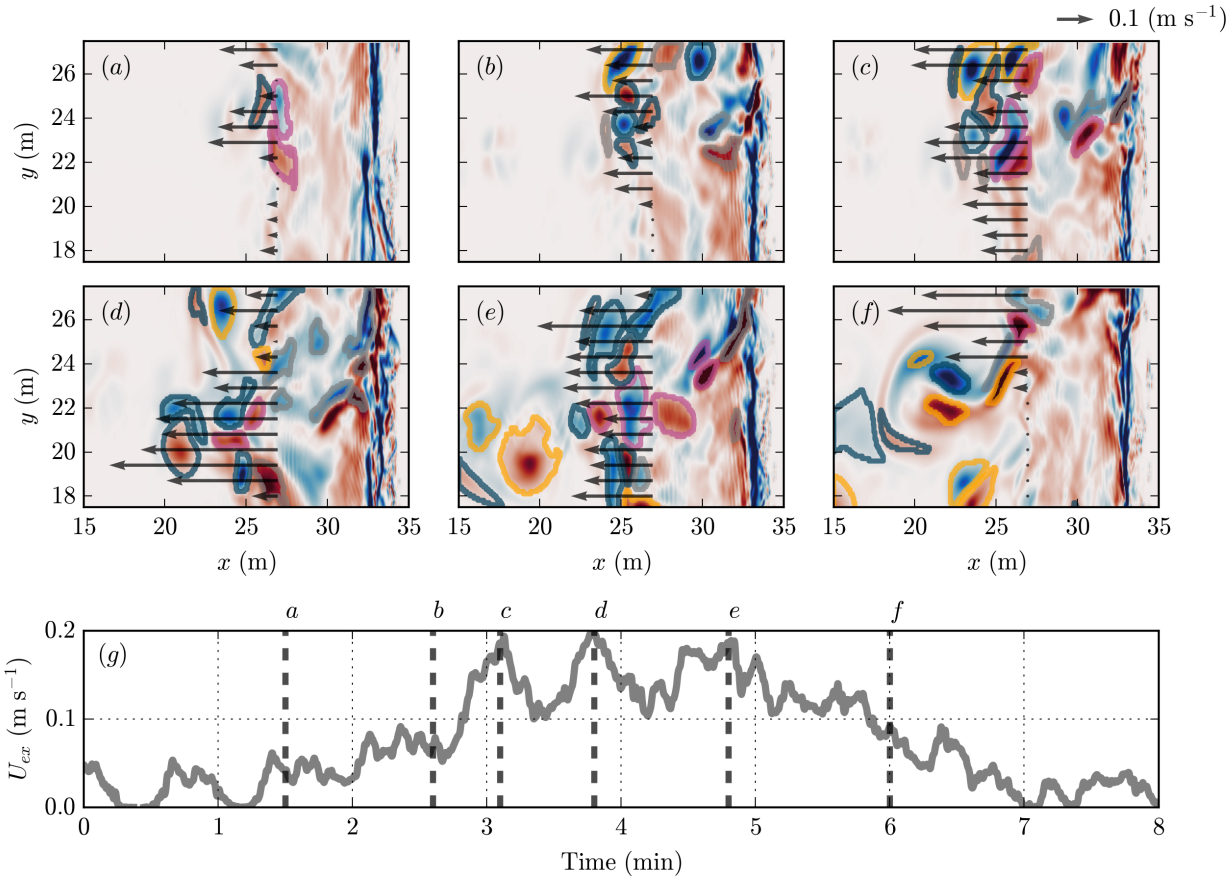

Figure 4.10: (a-f) Planar view of vorticity snapshots, identified eddies, and offshore velocity vectors during an offshore ejection event at six times. Identified eddies are colored by cluster type (cluster 1: blue, cluster 2: pink, cluster 3: yellow). Eddies that are short lived ($T_\epsilon < 5$ s) are colored in grey. Offshore velocity vectors are shown at the edge of the surf zone and are set to zero for any onshore velocity ($u > 0$). (g) Cross-shore exchange velocity (U_{ex}) computed over planar view box (17.5 - 27.5 m) at the surf-zone edge ($x_{sz} = 26.9$ m). Black dashed vertical lines denote the time of the six times shown in (a-f) and are labeled at the top of panel (g).

By focusing on this single ejection event, we begin to observe some notable features. In particular, while we are characterizing this ejection event as a "single" event because exchange velocities start and end near zero at the beginning and end of this time period, exchange velocities exhibit multiple clear peaks throughout this time period (Fig. 4.10g).

This variation in exchange over this ejection event is also associated with varying number of eddies and cluster types (Fig. 4.10a-f). When exchange is locally peaking, there are elevated number of eddies near the surf-zone edge (times c, d, e in Fig. 4.10). Conversely, when exchange is relatively low there are lower number of eddies near the surf-zone edge (times a, b, f in Fig. 4.10). Additionally, while presence of eddies near the surf-zone edge is associated with times of elevated exchange velocities, the locations of strong offshore flow (longer vector arrows in Fig. 4.10a-f) tend to be co-located with the presence of eddies and minimal or no offshore flow where there are no eddies. However, this is not ubiquitously true: offshore flow at time c shows weaker offshore flow between 17.5 - 21 m, where there are few identified eddies, but offshore flow is still $\sim$0.15 m s^{-1} (Fig. 4.10c).

While the presence of eddies near the surf-zone edge is associated with elevated offshore velocities, the type of clusters these eddies are associated with is not restricted to a single cluster type (Fig. 4.10a-f). All eddy trajectory types are present during ejection events, suggesting different types of eddy tracks contribute to the development of an ejection event. In addition to the three cluster types, identified eddies that have trajectories less than 5 s are also present (shown with grey boundary in Fig. 4.10a-f) in the ejection event and may be important for the development of offshore flow. Additionally, background vorticity structure changes throughout the ejection event. During times of stronger offshore flow, background vorticity tends to be stronger than times of lower offshore flow (Fig. 4.10c,d,e).

In addition to strength, the spatial structure of the background vorticity may be important. During the lead up to and duration of strong exchange velocities, the background vorticity tends to have negative vorticity in the north and positive vorticity in the south part of the region (Fig. 4.10b-e). While this structure varies through the ejection event, this larger scale background vorticity may be important to the development of offshore ejection of surf-zone eddies. Coherent eddies may be the visible indication that water has moved offshore, but background currents may also be driving transport that is not associated with coherent structures. Further investigation this eddy trajectory dataset

could help with characterizing what ejection events look like, how they vary between one another and in different wave conditions, and what drives the transport of eddies and tracers offshore.

4.4.7 Eddy tracking limitations and future work

Eddy tracking analysis here is reliant upon accurate tracking of coherent eddies through space and time. While visual inspection of eddy trajectories does suggest that eddies tend to be tracked well throughout the model domain and duration of the model simulation, our eddy tracking method does have limitations and does not perfectly track all eddies. Eddies offshore of the surf zone with low background vorticity are generally easier to track due to the fact that interaction with background currents or breaking waves is minimal and so the eddies are subject to slow changes in eddy size and circulation. In the surf zone, while time filtering of vorticity was completed to remove high frequency changes in the field, particularly from breaking waves propagating through the surf zone, vorticity still tends to be highly dynamic in time and space. The identified boundary of an eddy over time may grow in size or circulation beyond set thresholds with the passage of a breaking waves or interaction with other surf zone vorticity, causing the eddy track to stop.

Our algorithm does allow for small gaps in the eddy track such that large ephemeral changes in size or circulation do not always lead to track cessation if the vorticity signature is of similar character as the last identified eddy. However, a large increase or decrease in eddy size or circulation could be indicative of a fundamental shift in the eddy. Eddy-eddy interactions could lead to merging of multiple eddies into a new larger eddy. Conversely, splitting of a large eddy could result in multiple smaller eddies. Merging and splitting algorithms have been used in mesoscale eddy tracking to account for these dynamics (*Le Vu et al.*, 2018; *Tian et al.*, 2021). It has been found that the presence of nearby eddies as well as the β-effect, variation of Coriolis parameter with latitude, impacts oceanic eddy

merging leading to increased horizontal ocean mixing (*De Marez et al.*, 2020). While the β-effect does not impact surf zone eddies, the beach slope can act as a similar mechanism in the evolution of relative vorticity. Further investigation of surf zone eddy merging and splitting is likely beneficial to better understand the transport of tracers in the surf zone.

Tracer transport in the surf zone is crucial to our understanding and ability to predict processes such as nearshore water quality and larval transport. Variation in eddy nonlinearity through track duration suggests there are times that surf-zone eddies are sufficiently nonlinear to trap tracers and transport them as they translate. However, further investigation of how surf-zone eddy nonlinearity and tracer transport are related is needed to determine thresholds for how nonlinear eddies need to be to result in meaningful tracer transport. Additionally, open questions remain as to what drives tracer transport in the surf zone. The eddy field and structure of offshore currents during times of increased exchange velocities can look markedly different and be made up of a variety of eddy types over a small time period (Fig. 4.10). Relating eddy trajectory types and ejection event structure to tracer transport could contribute to improved understanding of surf-zone tracer transport mechanisms.

4.5 Conclusion

In this study we take an eddy focused perspective of surf-zone eddy dynamics by applying a tracking algorithm to identified coherent eddies in a wave-resolved numerical simulation. Eddy tracking successfully follows individual eddies through the surf zone and offshore as their location and eddy characteristics change. Additionally, we apply a clustering algorithm to classify types of eddy tracks and determine that 3 distinct trajectories are observed: 1) a surf-zone cluster, 2) an offshore cluster, and 3) a long-lived cluster. These clusters have distinct features, such as track duration, translation speed, and starting location, they also exhibit similarities, particularly in the surf zone. All eddy trajectories in the surf zone experience depth changes due to the presence of the bar-trough bathymetry. Analysis suggests that eddy transformation over track duration

tends to be consistent with conservation of potential vorticity. Additionally, in line with expectations of paired vortices subject to conservation of potential vorticity, eddies tend to slow their cross-shore translation speed in the trough. These slower cross-shore speeds in combination with larger alongshore translation speeds suggests that the barred bathymetry impacts cross-shore transport of eddies and tracers. However, a large number of eddies do transport offshore in transient rip current ejection events. These ejection events are made up of an array of eddy trajectory types and complex relationships between eddy number, location, and offshore flow. Further investigation is needed to related eddy locations and characteristics to exchange velocity and offshore flow.

Chapter 5
IMPLICATIONS AND FUTURE WORK

5.1 How is short-crested generated vorticity transferred to larger scales?

In Chapter 2 we quantified vorticity generation of short-crested waves on a barred beach. We found that as the directional spread increases, there is not a monotonic increase in vorticity generation despite presence of a greater number of breaking waves. Instead vorticity generation peaks at intermediate directional spread. Interestingly, instead of a similar peak at intermediate directional spread we observe a plateau in low and very low frequency rotational power at intermediate to high directional spreads. This mismatch between vorticity generation and resulting large-scale surf-zone vorticity highlights an open question about why this mismatch is observed and what it means for small-scale energy transfer.

5.1.1 Surf-zone inverse energy cascades

In the surf zone, energy transfer from small to large scales has been shown to be consistent with a forced two-dimensional turbulence system (*Spydell and Feddersen*, 2009; *Elgar and Raubenheimer*, 2020; *Elgar et al.*, 2023); however, this consistency has not been found for all directional spreads (*Baker et al.*, 2023a). In laboratory experiments on barred bathymetry, *Baker et al.* (2023a) found that energy transfer was consistent at high directional spread but not at intermediate spread. These differences in the rate of energy transfer across scales with directional spread in observations and a mismatch in vorticity forcing and large-scale rotational motions with directional spread, suggests that injected vorticity is not uniformly transformed for all directional spreads. An inverse cascade consistent with a forced two-dimensional turbulence system would transfer energy from small to

large scales at a consistent rate, implying that energy associated with large scale rotation motions should scale proportionally to vorticity injection. As we see a peak in forcing at intermediate directional spread and a plateau in low and very low frequency eddies, this may suggest that other surf zone processes, rather than an inverse energy cascade, are responsible for the transfer of energy between scales. This process may be influenced by alongshore length-scales in the surf zone associated with short-crested wave breaking, wave-current interaction, surf zone geometry, or beach bathymetry which may alter the transfer of energy from small to large scales. Further exploration of how energy is transferred from vorticity injection to larger scale eddies would provide insight into this process.

5.2 *How does barred-bathymetry impact surf-zone vorticity dynamics?*

While the impact of barred bathymetry is not explicitly explored in this dissertation, all model simulations have alongshore-uniform barred bathymetry, while most of the prior modeling work exploring transient rip currents and cross-shore exchange has been on alongshore-uniform planar and terraced beaches (*Spydell and Feddersen*, 2009; *Feddersen et al.*, 2011; *Suanda and Feddersen*, 2015; *Kumar and Feddersen*, 2017a; *O'Dea et al.*, 2021). Findings from Chapter 3 and 4 show that eddy properties transform across the surf zone and are modified by the beach bathymetry, consistent with conservation of potential vorticity. Additionally, findings from Chapter 4 show that along and cross-shore translation of eddies varies over the surf zone leading to decreased cross-shore translation out of the trough. The impact of bathymetry on eddy properties and translation suggests that the presence of barred bathymetry is important to these larger scale vorticity dynamics. A direct exploration of eddy transformation, energy transfer to larger scales, and development of cross-shore exchange and offshore ejection events on varying barred bathymetry is needed to understand the importance of the bar on these dynamics.

5.2.1 *Transformation of eddy properties over a sandbar*

From potential vorticity, we expect that as the water depth decreases, the magnitude of the local vorticity associated with an eddy decreases. This decrease in local vorticity can occur due to weakening of the rotational currents in the eddy or an increase in eddy size. Our results in Chapter 3 and 4 show that we see eddy transformation over the bar consistent with these expectations from potential vorticity. As eddies translate up the slope to the bar crest, they get larger in size and more circular, decreasing their local vorticity, and then as the eddies move offshore into deeper water, they decrease in size, become more elliptic, and increase their local vorticity. Without the presence of barred bathymetry, we expect that eddy size would decrease moving offshore, getting weaker vorticity and more linear. The slope, shape, and cross-shore position of the bar may have important implications for the development of ejection events, strength of cross-shore exchange velocities, and transport potential of individual eddies. Future work could simulate eddy transformation across a variety of barred bathymetry configurations. Sandbars are common on beaches worldwide, but can vary seasonally and inter-annually as the wave conditions vary. Better understanding of how the presence of barred-bathymetry impacts eddy transformation and resulting cross-shore transport is important to predicting changes in transient rip current activity that may be tied to cross-shore bathymetry changes and not wave conditions alone.

5.2.2 *Peak in exchange at intermediate directional spread*

In addition to eddy transformation across the surf, the presence of barred bathymetry may also influence cross-shore exchange and offshore transport of eddies. From exchange velocity parameterizations based on simulations of directionally spread waves on planar beaches, we expect that exchange velocities increase with increasing directional spread *Suanda and Feddersen* (2015). However, findings presented in Chapter 2 show that we do not see this trend, instead observing a peak in exchange at intermediate directional

spread and lower exchange at high directional spread. We see in Chapter 3 that median eddies sizes in the surf zone are approximately equivalent in size at intermediate and high directional spreads and exhibit similar eddy transformation across the bar; however, a larger number of non-linear eddies with strong circulation propagate far offshore at intermediate directional spread compared to high directional spread. Additionally, in Chapter 4 we find that cross-shore translation speeds of individual eddy trajectories slows in the trough, while alongshore translation speeds remain large, suggesting that eddies may get trapped in the trough consistent with expectations of paired vortices on barred bathymetry (*Bühler and Jacobson*, 2001). While this change in along and cross-shore translation speeds was only computed for intermediate spreads, investigation of these dynamics for other wave conditions would provide insight into whether alongshore translation of eddies is similar at high spreads or varies with directional spread. As cross-shore exchange velocities decrease for high directional spread, a reasonable hypothesis is that cross-shore translation of eddies at high spread are slowed in the trough more than intermediate spread leading to lower exchange velocities and offshore transport of eddies. Additionally, investigation of how eddies interact with each other in the trough is relevant. Large alongshore translation of eddies in the trough may increase eddy-eddy interactions and result in non-linear energy exchanges at different rates for varying spreads, consistent with energy cascades observed in laboratory experiments (*Baker et al.*, 2023a). Further work is needed to understand how barred bathymetry modifies offshore transport of eddies for varying wave conditions and to understand the role that eddy-eddy interactions in the trough play on enhancement or limitation of cross-shore eddy transport.

5.3 How does eddy focused perspective relate to Eulerian metrics?

In Chapter 3 we found that a greater number of eddies are found far offshore at intermediate directional spread compared with high directional spread. This cross-shore distribution of eddies is consistent with larger exchange velocities at intermediate directional spread, compared with low and high directional spread found in Chapter 2. While

this larger number of eddies offshore is consistent with larger exchange, the relationship between exchange velocities and eddy counts, locations, and properties is unknown. Better understanding of this relationship could allow for prediction of offshore eddy transport from eddy location, size, and strength in the surf zone. A predictive relationship of offshore transport from surf-zone eddy properties could allow for camera monitoring of beaches to predict offshore exchange by identifying eddies from camera imagery, similar to machine learning rip current detection using webcams (*Dusek et al.*, 2019). However, for these sort of applications to be successful, additional work understanding how eddy properties and transformation relate to our Eulerian understanding of transient rip current dynamics is needed.

5.3.1 Eddy properties and cross-shore exchange

We found in Chapter 3 that the locations of eddies are co-located with inflections in cross-shore rotational velocity and offshore directed flow at the surf-zone edge for both intermediate and high spreads. With eddy locations in the surf zone related to cross-shore rotational velocity, a natural hypothesis follows that the number of eddies in the surf zone may be directly related to cross-shore exchange velocities. However, it is clear from Chapter 3 that there are a larger number of eddies in the surf zone at high directional spread compared with intermediate directional spread. Despite more eddies in the surf zone, exchange velocities are weaker at high directional spread. Preliminary analysis not included in this dissertation, has shown that the relationship between the number of eddies in the surf zone and strength of cross-shore exchange are generally not well correlated across all directional spreads. Additionally, the strength of correlation varies between directional spreads. This preliminary analysis has also shown that scaling the number of eddies in the surf zone by a measure of their strength (i.e. mean circulation) improves the relationship between surf-zone eddy properties and exchange velocity, but this relationship remains weak and not correlated well consistently over the model

simulations. With a variety of surf-zone eddy properties available, additional work is needed to understand how these properties relate to the development of offshore flow. Additionally, while it is reasonable to expect that the identified coherent eddies can be directly related to exchange and transport of eddies offshore, non-coherent background vorticity and surf-zone currents may also play a significant role in determining how offshore flow develops. Relating our eddy focused perspective to Eulerian metrics from prior work is crucial to understanding what role these coherent eddies play compared to other processes.

5.3.2 Eddy life cycles and energy transfers

In Chapter 4, we found that not only do eddy properties vary between wave conditions, they also vary over their own life cycle. In the surf zone, eddies tend to increase in size during their initial phase and then decrease until their track ceases. Additionally, combined changes in size, circulation, and location (depth) tend to relatively conserve potential vorticity. While across many eddy tracks, eddy transformation tends to be consistent with potential vorticity, a range in behavior likely exists between all eddy trajectories in the surf-zone, with some eddies behaving consistently with conservation of potential vorticity and others not.

The framework for conservation of potential vorticity as solely a function of local vorticity and water depth assumes no external forcings, dissipation, and depth-averaged dynamics (*Salmon*, 1998). In the surf zone, these assumptions are not all valid. Waves propagate and break, interacting with individual eddies, the beach slope provides a source of dissipation through bottom friction, and while eddies in the surf have been shown to be relatively two-dimensional in the inner surf, eddies may become more three-dimensional in the outer surf (*Lippmann and Bowen*, 2016; *Henderson et al.*, 2017; *Baker et al.*, 2021). While we see that potential vorticity is generally conserved, these processes may be important in driving variation between individual eddy tracks. Understanding how energy in

individual eddies vary over their track duration and how energy is transferred between breaking waves and other eddies is important for better understanding the surf-zone inverse energy cascade.

From visual inspection of animations of identified eddies overlaid simulated vorticity, it is clear that individual eddies do experience significant eddy-wave interaction. From short-crested wave breaking theory, positive and negatively signed vorticity is generated at the left and right-hand sides of the breaking wave (*Peregrine*, 1999; *Spydell and Feddersen*, 2009; *Clark et al.*, 2012). This would suggest that the proximity of a signed eddy to the similarly signed vorticity generation side of the wave may lead to an increase in local vorticity, if the eddy rotation is in the same sense as the vorticity generated by the breaking wave. The injection of vorticity may be an external source of vorticity that increases the potential vorticity of the eddy. This injection and increase in local vorticity of the eddy may enhance offshore transport of tracers by increasing its nonlinearity (*Chelton et al.*, 2011a). Further investigation of eddy-wave interactions over track duration would aid in better understanding how energy is transferred from wave breaking driven injection to large-scale eddies and how this impacts cross-shore transport and tracer exchange.

In addition to interaction with breaking waves, eddies also interact with other eddies. These interactions with other eddies may provide insight into the surf-zone inverse energy cascade. It has been shown that the transfer of energy from small to large-scales in the surf zone can sometimes be consistent with a forced two-dimensional turbulence system (*Spydell and Feddersen*, 2009; *Elgar and Raubenheimer*, 2020; *Elgar et al.*, 2023), but this consistency is not seen for all wave conditions (*Baker et al.*, 2023a). While it has been shown that energy transfers from small to large scales are consistent with expectations from a forced two-dimensional turbulence system, an inverse energy cascade is expected to transfer energy incrementally and nonlinearly from small to large scales (*Boffetta and Ecke*, 2011). It is unknown if the energy transfers we observe in the surf zone are incremental or through other processes that result in energy at larger scales. Exploration of eddy-eddy interactions for individual tracks and the transfer of energy between breaking waves and

existing eddies would provide an additional perspective on how energy is transferred from small to large scales in the surf zone.

5.4 What drives tracer exchange?

The drive to understand how transient rip currents develop and vary in different wave conditions is motivated by their potential for tracer exchange. Exchange of material from the surf zone to the open ocean, such as pollutants, larvae, and nutrients, can have implications for nearshore water quality and ecosystem health (*Halpern et al.*, 2008; *Boehm et al.*, 2017; *Morgan et al.*, 2017; *Moulton et al.*, 2023). In our work in Chapter 2 and prior work (*Suanda and Feddersen*, 2015; *O'Dea et al.*, 2021), the directional spread of the wave field has been found to be an important driver in the magnitude of exchange velocities, with increased exchange velocities for large directional spreads compared with low directional spreads. However, this relationship is more complicated, with exchange at intermediate spreads of a similar magnitude (*O'Dea et al.*, 2021) or larger (*Nuss, Emma et al.*, b) than at high directional spread. Magnitude of exchange velocities vary with spread, but we have also found in Chapter 3 and 4 that the nonlinearity of eddies also varies with directional spread, cross-shore location, and eddy trajectory type. In the open ocean, eddy nonlinearity is an important driver of mixing and transport of ocean heat, salinity, and biogeochemical tracers (*Chelton et al.*, 2011a; *Travis and Qiu*, 2020; *Wekerle et al.*, 2020). In the surf zone, open questions remain about what tracer transport mechanisms dominate and whether these mechanisms vary with wave conditions and beach type.

5.4.1 Tracer transport mechanisms

Drifter measurements, dyes, and particle tracking have been used to understand transient rip current driven tracer exchange (*Johnson and Pattiaratchi*, 2006; *Spydell and Feddersen*, 2009; *Hally-Rosendahl et al.*, 2014; *Grimes et al.*, 2020). Our eddy focused perspective in Chapter 3 and 4 provides an opportunity to enhance our understanding of tracer transport

by transient rip currents. From mesoscale ocean eddy literature, we know that ocean eddies can transport and mix ocean tracers when eddies merge (*De Marez et al.*, 2020), as well as through tracer trapping in nonlinear eddies (*Chelton et al.*, 2011a; *Wekerle et al.*, 2020). In the surf zone, while eddies tend to be more linear they do exhibit significant variation in nonlinearity and potential for tracers trapping and transportation of material offshore. However, the magnitude of this process is unknown and would be aided by coupling our eddy focused perspective with particle tracking simulations to quantify tracer transport and relate it to eddy properties, such as nonlinearity. Additionally, while not included in our tracking algorithm, eddies do interact with other eddies and have the potential to merge, leading to tracer mixing and transport. In the surf zone, particularly at high directional spreads, eddies are densely distributed throughout the surf zone. Advection of eddies in background currents and self or mutually driven propagation may lead to merging of eddies. Eddy track duration in the surf zone was found to be relatively short, which may indicate that eddy merging occurs and results in cessation of the trajectory. However, explicit exploration and analysis is needed to quantify and understand this process. Better understanding of these eddy driven transport processes would aid in determining if tracer transport is dominated by individual eddy mixing and transport or development of strong offshore directed jets expected in the development of transient rip currents.

5.5 *What is a transient rip current?*

Existing literature has explored transient rip current dynamics by quantifying very low frequency rotational power (*e.g., Spydell and Feddersen*, 2009; *Elgar and Raubenheimer*, 2020; *Baker et al.*, 2021), cross-shore exchange velocities (*e.g., Suanda and Feddersen*, 2015; *O'Dea et al.*, 2021; *Nuss, Emma et al.*, b), and drifter tracks and tracer dispersion (*e.g., Johnson and Pattiaratchi*, 2006; *Hally-Rosendahl et al.*, 2014; *Grimes et al.*, 2020). Our eddy focused perspective in Chapter 3 and 4 provides new insight into how we characterize and understand transient rip current dynamics. Bathymetric rip current characterization of

two large oppositely signed vortices with alongshore feeder currents into an offshore jet between the vortex pair (*e.g., Kennedy*, 2003; *Bühler and Jacobson*, 2001) has provided a helpful frame for understanding expectations of how large scale eddies, generated by short-crested waves on alongshore uniform bathymetry, would generate strong offshore ephemeral flow. Offshore flow due to transient rip currents may be similar to bathymetric rip current structure and exist as two large eddy dipoles, with offshore flow between them, near the surf-zone edge.

Additionally, these expectations of increased offshore flow in the presence of large-scale eddy dipoles can be captured in cross-shore exchange velocities, which quantify offshore directed flow due to rotational velocities at the surf-zone edge (*Suanda and Feddersen*, 2015). The combination of these two perspectives of large eddy pairs and increased exchange provide two ways to quantify and characterize transient rip current activity, suggesting that transient rip currents are the presence of large eddies at the surf-zone edge and corresponding increased exchange velocities. However, in Chapter 4 we examined an ejection event characterized by increased exchange velocities over a finite alongshore region and saw a more complex view of what a transient rip current is.

In this ejection event, while exchange velocity was increased, the ejection event was characterized by a collection of eddies, rather than by a single dipole pair of two large oppositely signed eddies. While this ejection event is made up of a collection of eddies, both positive and negatively signed, there are times that distinct eddy pairs propagate offshore together from the surf-zone edge and travel together far offshore. This variation in ejection event structure and presence of paired and unpaired eddies suggests that eddy driven transient rip current transport can vary in structure and mechanism.

In addition to variation in the number and make up of eddies in an ejection event, large-scale vorticity and background currents also exist in the surf zone. At intermediate directional spread in particular, large scale regions of positive or negative background vorticity setup. Eddies tend to move through the background vorticity and then eject offshore between these oppositely signed regions of vorticity. This process suggests

further mechanisms for eddy transport that are related to large scale feeder currents and an offshore jet of eddies.

The presence of eddy dipoles, feeder currents and offshore jets, and collections of eddy movement together all associated with increased cross-shore exchange velocities suggests that "transient rip currents" may actually a variety of eddy transport mechanisms. Further work to determine why different ejection event structures develop, their relationship to cross-shore exchange and tracer dispersal, and their variation under different wave conditions or beach types is an exciting area for future research.

Chapter 6

SUMMARY AND CONCLUSION

In this dissertation we investigate surf-zone vorticity through the use of phase-resolved numerical model simulations and eddy tracking. In Chapter 2 we simulated wave fields with varying directional spread and peak period and quantified wave field characteristics, vorticity generation, low frequency rotational power, and cross-shore exchange velocities. We found that as directional spread increases, mean crest lengths decrease and the number of crest ends increases. However, we find that despite more breaking waves, the generation of vorticity peaks at intermediate directional spread due to the fact that longer crests tend to generate a larger magnitude of vorticity. Additionally, we found that low frequency rotational power plateaus at intermediate to high spreads, whereas exchange velocities peak at intermediate spread, similar to vorticity generation.

In Chapter 3 we took an eddy focused perspective on surf-zone vorticity for low, intermediate, and high directional spread wave conditions by identifying coherent vorticity features, eddies, from model simulations. We find eddy size, shape, and circulation vary minimally between directional spreads, but exhibit strong cross-shore variation, particularly over the bar-trough bathymetry. Additionally, we find that a larger number of eddies, with increased non-linearity, are observed offshore at intermediate directional spread compared with low and high directional spread, consistent with increased exchange velocities for intermediate directional spread. Lastly, we showed that eddy locations are co-located with inflections in cross-shore flow and offshore directed flow, suggesting Eulerian and eddy focused perspectives can be related.

In Chapter 4 we tracked identified eddies through time and space for intermediate directional spread conditions. Additionally, we classified distinct types of eddy trajectories

using a clustering algorithm and found that there are three eddy track types, a surf-zone cluster, an offshore cluster, and a long-lived cluster. While these clusters exhibit distinct characteristics, such as track duration and eddy translation speed, all clusters exhibit cross-shore variation tied to the bar-trough bathymetry. In particular, eddy tracks in the trough reduce their offshore speed and translate alongshore, suggesting eddies may get trapped in the surf zone due to the presence of the bar. This cross-shore variation in eddy translation is expected due to conservation of potential vorticity and eddy trajectories in the surf zone exhibit relative consistency with conservation of potential vorticity over their track duration. Lastly, we explored how these eddy trajectory types related to ejection events and find that further investigation of what drives offshore ejection events and tracer transport is needed.

BIBLIOGRAPHY

Baker, C. M., Surfzone vorticity dynamics in a directional wave basin, *University of Washington*, 2023.

Baker, C. M., M. Moulton, B. Raubenheimer, S. Elgar, and N. Kumar, Modeled Three-Dimensional Currents and Eddies on an Alongshore-Variable Barred Beach, *Journal of Geophysical Research: Oceans*, *126*(7), doi:10.1029/2020JC016899, publisher: John Wiley and Sons Inc, 2021.

Baker, C. M., M. Moulton, C. C. Chickadel, E. S. Nuss, M. L. Palmsten, and K. L. Brodie, Two-dimensional inverse energy cascade in a laboratory surf zone for varying wave directional spread, *Physics of Fluids*, 2023a.

Baker, C. M., M. Moulton, M. L. Palmsten, K. Brodie, E. Nuss, and C. C. Chickadel, Remotely sensed short-crested breaking waves in a laboratory directional wave basin, *Coastal Engineering*, *183*, 104,327, doi:10.1016/j.coastaleng.2023.104327, 2023b.

Baker, Christine, Moulton, Melissa, Chickadel, Chris, Nuss, Emma, Palmsten, Margaret, and Brodie, Katherine, Vertical vorticity production magnitude and length scales: Dependence on short-crested breaking wave field characteristics in the laboratory, [in prep].

Bishop, C. T., and M. A. Donelan, Measuring waves with pressure transducers, *Coastal Engineering*, *11*(4), 309–328, doi:10.1016/0378-3839(87)90031-7, 1987.

Boehm, A. B., N. S. Ismail, L. M. Sassoubre, and E. A. Andruszkiewicz, Oceans in Peril: Grand Challenges in Applied Water Quality Research for the 21st Century, *Environmental Engineering Science*, *34*(1), 3–15, doi:10.1089/ees.2015.0252, 2017.

Boffetta, G., and R. E. Ecke, Two-dimensional turbulence, *Annual Review of Fluid Mechanics*, *44*, 427–451, doi:10.1146/annurev-fluid-120710-101240, 2011.

Bondehagen, A., et al., Wave-driven current and vortex patterns at an open beach: Insights from phase-resolving numerical computations and Lagrangian measurements, *Coastal Engineering*, *193*, 104,591, doi:10.1016/j.coastaleng.2024.104591, 2024.

Bonneton, P., N. Bruneau, B. Castelle, and F. Marche, Large-scale vorticity generation due to dissipating waves in the surf zone, *Discrete and Continuous Dynamical Systems - Series B*, *13*(4), 729–738, doi:10.3934/dcdsb.2010.13.729, 2010.

Bowen, A. J., and R. A. Holman, Shear instabilities of the mean longshore current: 1. Theory, *Journal of Geophysical Research*, *94*(C12), doi:10.1029/jc094ic12p18023, 1989.

Bruneau, N., P. Bonneton, B. Castelle, and R. Pedreros, Modeling rip current circulations and vorticity in a high-energy mesotidal-macrotidal environment, *Journal of Geophysical Research: Oceans*, *116*(C7), 2010JC006,693, doi:10.1029/2010JC006693, 2011.

Bühler, O., and T. E. Jacobson, Wave-driven currents and vortex dynamics on barred beaches, *Journal of Fluid Mechanics*, *449*, 313–339, doi:10.1017/S0022112001006322, 2001.

Carini, R. J., C. C. Chickadel, A. T. Jessup, and J. Thomson, Estimating wave energy dissipation in the surf zone using thermal infrared imagery, *Journal of Geophysical Research: Oceans*, *120*(6), 3937–3957, doi:10.1002/2014JC010561, 2015.

Castelle, B., T. Scott, R. W. Brander, and R. J. McCarroll, Rip current types, circulation and hazard, *Earth-Science Reviews*, *163*, 1–21, doi:10.1016/j.earscirev.2016.09.008, publisher: The Authors, 2016.

Chelton, D. B., P. Gaube, M. G. Schlax, J. J. Early, and R. M. Samelson, The Influence of Nonlinear Mesoscale Eddies on Near-Surface Oceanic Chlorophyll, *Science*, *334*(6054), 328–332, doi:10.1126/science.1208897, 2011a.

Chelton, D. B., M. G. Schlax, and R. M. Samelson, Global observations of nonlinear mesoscale eddies, *Progress in Oceanography*, *91*(2), 167–216, doi:10.1016/j.pocean.2011.01.002, 2011b.

Chen, Q., J. T. Kirby, R. A. Dalrymple, A. B. Kennedy, and A. Chawla, Boussinesq Modeling of Wave Transformation, Breaking, and Runup. II: 2D, *Journal of Waterway, Port, Coastal, and Ocean Engineering*, *126*(1), 48–56, doi:10.1061/(ASCE)0733-950X(2000)126:1(48), 2000.

Choi, J., and M. Roh, A laboratory experiment of rip currents between the ends of breaking wave crests, *Coastal Engineering*, *164*, doi:10.1016/j.coastaleng.2020.103812, publisher: Elsevier B.V., 2021.

Choi, Y., B. Bouscasse, S. Seng, G. Ducrozet, L. Gentaz, and P. Ferrant, Generation of Regular and Irregular Waves in Navier-Stokes CFD Solvers by Matching With the Nonlinear Potential Wave Solution at the Boundaries, in *Volume 2: CFD and FSI*, p. V002T08A020, American Society of Mechanical Engineers, Madrid, Spain, doi:10.1115/OMAE2018-78077, 2018a.

Choi, Y.-K., F. Shi, M. Malej, and J. M. Smith, Performance of various shock-capturing-type reconstruction schemes in the Boussinesq wave model, FUNWAVE-TVD, *Ocean Modelling*, *131*, 86–100, doi:10.1016/j.ocemod.2018.09.004, 2018b.

Clark, D. B., F. Feddersen, and R. T. Guza, Cross-shore surfzone tracer dispersion in an alongshore current, *Journal of Geophysical Research: Oceans*, *115*(C10), 2009JC005,683, doi:10.1029/2009JC005683, 2010.

Clark, D. B., F. Feddersen, and R. T. Guza, Modeling surf zone tracer plumes: 2. Transport and dispersion, *Journal of Geophysical Research: Oceans*, *116*(C11), 2011JC007,211, doi:10.1029/2011JC007211, 2011.

Clark, D. B., S. Elgar, and B. Raubenheimer, Vorticity generation by short-crested wave breaking, *Geophysical Research Letters*, *39*(24), 1–6, doi:10.1029/2012GL054034, 2012.

Dalrymple, R. A., Directional wavemaker theory with sidewall reflection, *Journal of Hydraulic Research*, *27*(1), 23–34, doi:10.1080/00221688909499241, 1989.

Dalrymple, R. A., and G. A. Lanan, Beach cusps formed by intersecting waves, *Geological Society of America Bulletin*, *87*(1), 57, doi:10.1130/0016-7606(1976)87<57:BCFBIW>2.0.CO;2, 1976.

De Marez, C., X. Carton, P. L'Hégaret, T. Meunier, A. Stegner, B. Le Vu, and M. Morvan, Oceanic vortex mergers are not isolated but influenced by the -effect and surrounding eddies, *Scientific Reports*, *10*(1), 2897, doi:10.1038/s41598-020-59800-y, 2020.

Dooley, C., S. Elgar, and B. Raubenheimer, Field Observations of Surfzone Vorticity, *Geophysical Research Letters*, *51*(20), e2024GL111,402, doi:10.1029/2024GL111402, 2024.

Duncan, J H, An experimental investigation of breaking waves produced by a towed hydrofoil, *Proceedings of the Royal Society of London. A. Mathematical and Physical Sciences*, *377*(1770), 331–348, doi:10.1098/rspa.1981.0127, 1981.

Dusek, G., D. Hernandez, M. Willis, J. A. Brown, J. W. Long, D. E. Porter, and T. C. Vance, WebCAT: Piloting the Development of a Web Camera Coastal Observing Network for Diverse Applications, *Frontiers in Marine Science*, *6*, 353, doi:10.3389/fmars.2019.00353, 2019.

Elgar, S., and B. Raubenheimer, Field evidence of inverse energy cascades in the surfzone, *Journal of Physical Oceanography*, *50*(8), 2315–2321, doi:10.1175/JPO-D-19-0327.1, publisher: American Meteorological Society, 2020.

Elgar, S., B. Raubenheimer, D. B. Clark, and M. Moulton, Extremely Low Frequency (0.1 to 1.0 mHz) Surf Zone Currents, *Geophysical Research Letters*, *46*(3), 1531–1536, doi:10.1029/2018GL081106, 2019.

Elgar, S., C. Dooley, L. Gorrell, and B. Raubenheimer, Observations of two-dimensional turbulence in the surfzone, *Physics of Fluids*, *35*(8), 085,142, doi:10.1063/5.0159170, 2023.

Feddersen, F., The generation of surfzone eddies in a strong alongshore current, *Journal of Physical Oceanography*, *44*(2), 600–617, doi:10.1175/JPO-D-13-051.1, 2014.

Feddersen, F., R. T. Guza, S. Elgar, and T. H. Herbers, Alongshore momentum balances in the nearshore, *Journal of Geophysical Research: Solid Earth*, *103*(C8), 15,667–15,676, doi:10.1029/98jc01270, publisher: Blackwell Publishing Ltd, 1998.

Feddersen, F., D. B. Clark, and R. T. Guza, Modeling surf zone tracer plumes: 1. Waves, mean currents, and low-frequency eddies, *Journal of Geophysical Research: Oceans*, *116*(11), doi:10.1029/2011JC007210, 2011.

Flierl, Glenn R, Particle motions in large-amplitude wave fields, *Geophysical and Astrophysical Fluid Dynamics*, *18*, 39–74, 1981.

Gaffney, S., and P. Smyth, Trajectory clustering with mixtures of regression models, in *Proceedings of the fifth ACM SIGKDD international conference on Knowledge discovery and data mining*, pp. 63–72, ACM, San Diego California USA, doi:10.1145/312129.312198, 1999.

Gariel, M., A. N. Srivastava, and E. Feron, Trajectory Clustering and an Application to Airspace Monitoring, *IEEE Transactions on Intelligent Transportation Systems*, *12*(4), 1511–1524, doi:10.1109/TITS.2011.2160628, 2011.

Geiman, J. D., and J. T. Kirby, Unforced Oscillation of Rip-Current Vortex Cells, *Journal of Physical Oceanography*, *43*(3), 477–497, doi:10.1175/JPO-D-11-0164.1, 2013.

Grimes, D. J., and F. Feddersen, The self-similar stratified inner-shelf response to transient rip-current-induced mixing, *Journal of Fluid Mechanics*, *915*, doi:10.1017/jfm.2021.140, publisher: Cambridge University Press (CUP), 2021.

Grimes, D. J., F. Feddersen, S. N. Giddings, and G. Pawlak, Cross-shore deformation of a surfzone released dye plume by an internal tide on the inner-shelf, *Journal of Physical*

Oceanography, *49*(10), doi:10.1175/JPO-D-19-0046.1, publisher: American Meteorological Society, 2019.

Grimes, D. J., F. Feddersen, and N. Kumar, Tracer Exchange Across the Stratified Inner-Shelf Driven by Transient Rip-Currents and Diurnal Surface Heat Fluxes, *Geophysical Research Letters*, *47*(10), doi:10.1029/2019GL086501, publisher: Blackwell Publishing Ltd, 2020.

Grossi, M. D., M. Kubat, and T. M. Özgökmen, Predicting particle trajectories in oceanic flows using artificial neural networks, *Ocean Modelling*, *156*, doi:10.1016/j.ocemod.2020.101707, publisher: Elsevier Ltd, 2020.

Guza, R. T., and E. B. Thornton, Local and shoaled comparisons of sea surface elevations, pressures, and velocities, *Journal of Geophysical Research*, *85*(C3), 1524, doi:10.1029/jc085ic03p01524, 1980.

Haller, M. C., U. Putrevu, J. Oltman-Shay, and R. A. Dalrymple, Wave Group Forcing of Low Frequency Surf Zone Motion, *Coastal Engineering Journal*, *41*(2), 121–136, doi:10.1142/S0578563499000085, 1999.

Hally-Rosendahl, K., and F. Feddersen, Modeling surfzone to inner-shelf tracer exchange: MODELING SURFZONE/INNER-SHELF EXCHANGE, *Journal of Geophysical Research: Oceans*, *121*(6), 4007–4025, doi:10.1002/2015JC011530, 2016.

Hally-Rosendahl, K., F. Feddersen, and R. T. Guza, Cross-shore tracer exchange between the surfzone and inner-shelf, *Journal of Geophysical Research: Oceans*, *119*(7), 4367–4388, doi:10.1002/2013JC009722, publisher: Blackwell Publishing Ltd, 2014.

Halpern, B. S., et al., A Global Map of Human Impact on Marine Ecosystems, *Science*, *319*(5865), 948–952, doi:10.1126/science.1149345, 2008.

Henderson, S. M., J. Arnold, H. T. Özkan-Haller, and S. A. Solovitz, Depth Dependence of Nearshore Currents and Eddies, *Journal of Geophysical Research: Oceans*, *122*(11), 9004–9031, doi:10.1002/2016JC012349, 2017.

Intergovernmental Panel on Climate Change (IPCC), *The Ocean and Cryosphere in a Changing Climate: Special Report of the Intergovernmental Panel on Climate Change*, Cambridge University Press, Cambridge, 2022.

Jain, A. K., M. N. Murty, and P. J. Flynn, Data clustering: a review, *ACM Computing Surveys*, *31*(3), 264–323, doi:10.1145/331499.331504, 1999.

Johnson, D., and C. Pattiaratchi, Boussinesq modelling of transient rip currents, *Coastal Engineering*, *53*(5-6), 419–439, doi:10.1016/j.coastaleng.2005.11.005, 2006.

Kennedy, A. B., A circulation description of a rip current neck, *Journal of Fluid Mechanics*, (497), 225–234, doi:10.1017/S0022112003006827, 2003.

Kennedy, A. B., Fluctuating circulation forced by unsteady multidirectional breaking waves, *Journal of Fluid Mechanics*, *538*(-1), 189, doi:10.1017/S0022112005005549, 2005.

Kennedy, A. B., Q. Chen, J. T. Kirby, and R. A. Dalrymple, Boussinesq Modeling of Wave Transformation, Breaking, and Runup. I: 1D, *Journal of Waterway, Port, Coastal, and Ocean Engineering*, *126*(1), 39–47, doi:10.1061/(ASCE)0733-950X(2000)126:1(39), 2000.

Kirby, J. T., Boussinesq models and their application to coastal processes across a wide range of scales, *Journal of Waterway, Port, Coastal and Ocean Engineering*, *142*(6), doi:10.1061/(ASCE)WW.1943-5460.0000350, publisher: American Society of Civil Engineers (ASCE), 2016.

Kirby, J. T., and M. Derakhti, Short-crested wave breaking, *European Journal of Mechanics, B/Fluids*, *73*, 100–111, doi:10.1016/j.euromechflu.2017.11.001, publisher: Elsevier Ltd, 2019.

Kontopoulos, I., A. Makris, and K. Tserpes, A Deep Learning Streaming Methodology for Trajectory Classification, *ISPRS International Journal of Geo-Information*, *10*(4), 250, doi:10.3390/ijgi10040250, 2021.

Kuik, A. J., G. P. Van Vledder, and L. Holthuijsen, [15200485 - Journal of Physical Oceanography] A Method for the Routine Analysis of Pitch-and-Roll Buoy Wave Data, *Journal of Physical Oceanography*, *18*, 1988.

Kumar, N., and F. Feddersen, The effect of stokes drift and transient rip currents on the inner shelf. Part I: No stratification, *Journal of Physical Oceanography*, *47*(1), 227–241, doi:10.1175/JPO-D-16-0076.1, 2017a.

Kumar, N., and F. Feddersen, The effect of stokes drift and transient rip currents on the inner shelf. Part II: With stratification, *Journal of Physical Oceanography*, *47*(1), 243–260, doi:10.1175/JPO-D-16-0077.1, publisher: American Meteorological Society, 2017b.

Kumar, N., and F. Feddersen, A new offshore transport mechanism for shoreline-released tracer induced by transient rip currents and stratification, *Geophysical Research Letters*, *44*(6), 2843–2851, doi:10.1002/2017GL072611, 2017c.

Kumar, N., et al., The Inner-Shelf Dynamics Experiment, *Bulletin of the American Meteorological Society*, *102*(5), E1033–E1063, doi:10.1175/BAMS-D-19-0281.1, 2021.

Le Vu, B., A. Stegner, and T. Arsouze, Angular Momentum Eddy Detection and Tracking Algorithm (AMEDA) and Its Application to Coastal Eddy Formation, *Journal of Atmospheric and Oceanic Technology*, *35*(4), 739–762, doi:10.1175/JTECH-D-17-0010.1, 2018.

Lippmann, T. C., and A. J. Bowen, The vertical structure of low-frequency motions in the nearshore. Part II: Theory, *Journal of Physical Oceanography*, *46*(12), 3713–3727, doi:10.1175/JPO-D-16-0015.1, 2016.

Lippmann, T. C., T. H. C. Herbers, and E. B. Thornton, Gravity and Shear Wave Contributions to Nearshore Infragravity Motions, *Journal of Physical Oceanography*, *29*(2), 231–239, doi:10.1175/1520-0485(1999)029<0231:GASWCT>2.0.CO;2, 1999.

Long, J. W., and H. T. Özkan Haller, Low-frequency characteristics of wave group–forced vortices, *Journal of Geophysical Research*, *114*(C8), 1–21, doi:10.1029/2008jc004894, 2009.

Longuet-Higgins, M. S., The refraction of sea waves in shallow water, *Journal of Fluid Mechanics*, *1*(2), 163–176, doi:10.1017/S0022112056000111, 1956.

Longuet-Higgins, M. S., Longshore currents generated by obliquely incident sea waves: 2, *Journal of Geophysical Research*, *75*(33), 6790–6801, doi:10.1029/JC075i033p06790, 1970.

Lynett, P. J., Nearshore Wave Modeling with High-Order Boussinesq-Type Equations, *Journal of Waterway, Port, Coastal, and Ocean Engineering*, *132*(5), 348–357, doi:10.1061/(ASCE)0733-950X(2006)132:5(348), 2006.

MacMahan, J., et al., Mean Lagrangian flow behavior on an open coast rip-channeled beach: A new perspective, *Marine Geology*, *268*(1-4), 1–15, doi:10.1016/j.margeo.2009.09.011, 2010a.

MacMahan, J. H., E. B. Thornton, and A. J. Reniers, Rip current review, *Coastal Engineering*, *53*(2-3), 191–208, doi:10.1016/j.coastaleng.2005.10.009, 2006.

MacMahan, J. H., A. J. H. M. Reniers, and E. B. Thornton, Vortical surf zone velocity fluctuations with o(10) min period, *Journal of Geophysical Research: Oceans*, *115*(C6), 2009JC005,383, doi:10.1029/2009JC005383, 2010b.

Marchesiello, P., F. Auclair, L. Debreu, J. McWilliams, R. Almar, R. Benshila, and F. Dumas, Tridimensional nonhydrostatic transient rip currents in a wave-resolving model, *Ocean Modelling*, *163*, doi:10.1016/j.ocemod.2021.101816, publisher: Elsevier Ltd, 2021.

Mason, E., A. Pascual, and J. C. McWilliams, A New Sea Surface Height–Based Code for Oceanic Mesoscale Eddy Tracking, *Journal of Atmospheric and Oceanic Technology*, *31*(5), 1181–1188, doi:10.1175/JTECH-D-14-00019.1, 2014.

Mason, E., A. Pascual, P. Gaube, S. Ruiz, J. L. Pelegrí, and A. Delepoulle, Subregional characterization of mesoscale eddies across the brazil-malvinas confluence, *Journal of Geophysical Research: Oceans*, *122*(4), 3329–3357, doi:10.1002/2016JC012611, 2017.

McWilliams, J. C., J. B. Weiss, and I. Yavneh, The vortices of homogeneous geostrophic turbulence, *Journal of Fluid Mechanics*, *401*, 1–26, doi:10.1017/S0022112099006382, 1999.

Miche, Le pouvoir reflechissant des ouvrages maritimes exposes a l'action de la houle, *Annales de Ponts et Chaussees*, 1944.

Mitsuyasu, Hisashi, Tasai, Fukuzo, Suhara, Toshiko, Mizuno, Shinjiro, Ohkusu, Makoto, and Rikiishi, Kunio, Observations of the directional spectrum of ocean WavesUsing a cloverleaf buoy, *Journal of Physical Oceanography*, 1975.

Morgan, S. G., A. L. Shanks, J. H. Macmahan, A. J. H. M. Reniers, and F. Feddersen, Planktonic Subsidies to Surf-Zone and Intertidal Communities, doi:10.1146/annurev-marine-010816, 2017.

Moulton, M., S. H. Suanda, J. C. Garwood, N. Kumar, M. R. Fewings, and J. M. Pringle, Exchange of Plankton, Pollutants, and Particles Across the Nearshore Region, *Annual Review of Marine Science*, *15*(1), annurev–marine–032,122–115,057, doi:10.1146/annurev-marine-032122-115057, 2023.

Newberger, P. A., and J. S. Allen, Forcing a three-dimensional, hydrostatic, primitive-equation model for application in the surf zone: 1. Formulation, *Journal of Geophysical Research*, *112*(C8), C08,018, doi:10.1029/2006JC003472, 2007.

Nuss, Emma, Moulton, Melissa, Suanda, Sutara, and Baker, Christine, An eddy perspective of the surf zone, [in prep], a.

Nuss, Emma, Moulton, Melissa, Suanda, Sutara, and Baker, Christine, Modeled surf-zone eddies on a laboratory scale barred beach with varying wave conditions, [in review], b.

Nwogu, O. G., Numerical Prediction of Breaking Waves and Currents with a Boussinesq Model, in *Coastal Engineering 1996*, pp. 4807–4820, American Society of Civil Engineers, Orlando, Florida, United States, doi:10.1061/9780784402429.374, 1997.

O'Dea, A., N. Kumar, and M. C. Haller, Simulations of the Surf Zone Eddy Field and Cross-Shore Exchange on a Nonidealized Bathymetry, *Journal of Geophysical Research: Oceans*, *126*(5), doi:10.1029/2020jc016619, publisher: American Geophysical Union (AGU), 2021.

Oltman-Shay, J., P. A. Howd, and W. A. Birkemeier, Shear instabilities of the mean longshore current: 2. Field observations, *Journal of Geophysical Research*, *94*(C12), 18,031, doi:10.1029/JC094iC12p18031, 1989.

Pauletic, I., L. N. Prskalo, and M. B. Bakaric, An Overview of Clustering Models with an Application to Document Clustering, in *2019 42nd International Convention on Information and Communication Technology, Electronics and Microelectronics (MIPRO)*, pp. 1659–1664, IEEE, Opatija, Croatia, doi:10.23919/MIPRO.2019.8756868, 2019.

Pegliasco, C., A. Chaigneau, and R. Morrow, Main eddy vertical structures observed in the four major Eastern Boundary Upwelling Systems, *Journal of Geophysical Research: Oceans*, *120*(9), 6008–6033, doi:10.1002/2015JC010950, 2015.

Pegliasco, C., A. Chaigneau, R. Morrow, and F. Dumas, Detection and tracking of mesoscale eddies in the Mediterranean Sea: A comparison between the Sea Level Anomaly and the Absolute Dynamic Topography fields, *Advances in Space Research*, *68*(2), 401–419, doi:10.1016/j.asr.2020.03.039, 2021.

Peregrine, D., Large-scale vorticity generation by breakers in shallow and deep water,

European Journal of Mechanics - B/Fluids, *18*(3), 403–408, doi:10.1016/S0997-7546(99)80037-5, 1999.

Peregrine, D. H., Theoretical and Computational Surf Zone Currents 1, *Theoret. Comput. Fluid Dynamics*, *10*(November 1996), 295–309, 1998.

Postacchini, M., M. Brocchini, and L. Soldini, Vorticity generation due to cross-sea, *Journal of Fluid Mechanics*, *744*, 286–309, doi:10.1017/jfm.2014.44, 2014.

Qiao, D., X. Yang, Y. Liang, and X. Hao, Rapid trajectory clustering based on neighbor spatial analysis, *Pattern Recognition Letters*, *156*, 167–173, doi:10.1016/j.patrec.2022.03.010, 2022.

Raubenheimer, B., R. T. Guza, and S. Elgar, Wave transformation across the inner surf zone, *Journal of Geophysical Research: Oceans*, *101*(C11), 25,589–25,597, doi:10.1029/96JC02433, 1996.

Reniers, A. J. H. M., J. H. MacMahan, E. B. Thornton, T. P. Stanton, M. Henriquez, J. W. Brown, J. A. Brown, and E. Gallagher, Surf zone surface retention on a rip-channeled beach, *Journal of Geophysical Research*, *114*(C10), C10,010, doi:10.1029/2008JC005153, 2009.

Ris, R., L. Holthuijsen, and N. Booij, A Spectral Model for Waves in the Near Shore Zone, in *Coastal Engineering 1994*, pp. 68–78, American Society of Civil Engineers, Kobe, Japan, doi:10.1061/9780784400890.006, 1995.

Salatin, R., Q. Chen, A. S. Bak, F. Shi, and S. R. Brandt, Effects of Wave Coherence on Longshore Variability of Nearshore Wave Processes, *Journal of Geophysical Research: Oceans*, *126*(11), doi:10.1029/2021JC017641, 2021.

Salmon, R., *Lectures on Geophysical Fluid Dynamics*, Oxford University Press, 1998.

Schlax, Michael G, and Chelton, Dudley B, The "Growing Method" of Eddy Identification and Tracking in Two and Three Dimensions, *College of Earth, Ocean and Atmospheric Sciences, Oregon State Univeristy*, *8*(23), 2016.

Schäffer, H., and C. Steenberg, Second-order wavemaker theory for multidirectional waves, *Ocean Engineering*, *30*(10), 1203–1231, doi:10.1016/S0029-8018(02)00100-2, 2003.

Shi, F., J. T. Kirby, J. C. Harris, J. D. Geiman, and S. T. Grilli, A high-order adaptive time-stepping TVD solver for Boussinesq modeling of breaking waves and coastal inundation, *Ocean Modelling*, *43-44*, 36–51, doi:10.1016/j.ocemod.2011.12.004, publisher: Elsevier Ltd, 2012.

Shi, F., J. T. Kirby, B. Tehranirad, and J. C. Harris, FUNWAVE-TVD Fully Nonlinear Boussinesq Wave Model with TVD Solver-Documentation and User's Manual (Version 3.0), *Tech. rep.*, 2016.

Smit, P., M. Zijlema, and G. Stelling, Depth-induced wave breaking in a non-hydrostatic, near-shore wave model, *Coastal Engineering*, *76*, 1–16, doi:10.1016/j.coastaleng.2013.01.008, 2013.

Smyth, P., K. Ide, and M. Ghil, Multiple Regimes in Northern Hemisphere Height Fields via MixtureModel Clustering*, *Journal of the Atmospheric Sciences*, *56*(21), 3704–3723, doi:10.1175/1520-0469(1999)056<3704:MRINHH>2.0.CO;2, 1999.

Spydell, M., The suppression of surfzone cross-shore mixing by alongshore currents, *Geophysical Research Letters*, *43*(18), 9781–9790, doi:10.1002/2016GL070626, 2016.

Spydell, M., and F. Feddersen, Lagrangian drifter dispersion in the surf zone: Directionally spread, normally incident waves, *Journal of Physical Oceanography*, *39*(4), 809–830, doi:10.1175/2008JPO3892.1, 2009.

Spydell, M., F. Feddersen, and R. T. Guza, Observations of drifter dispersion in the surfzone: The effect of sheared alongshore currents, *Journal of Geophysical Research*, *114*(C7), C07,028, doi:10.1029/2009JC005328, 2009.

Suanda, S. H., and F. Feddersen, A self-similar scaling for cross-shelf exchange driven by transient rip currents, *Geophysical Research Letters*, *42*(13), 5427–5434, doi:10.1002/2015GL063944, 2015.

Suanda, S. H., S. Perez, and F. Feddersen, Evaluation of a source-function wavemaker for generating random directionally spread waves in the sea-swell band, *Coastal Engineering*, *114*, 220–232, doi:10.1016/j.coastaleng.2016.04.006, publisher: Elsevier B.V., 2016.

Sullivan, P. P., J. C. McWILLIAMS, and W. K. Melville, Surface gravity wave effects in the oceanic boundary layer: large-eddy simulation with vortex force and stochastic breakers, *Journal of Fluid Mechanics*, *593*, 405–452, doi:10.1017/S002211200700897X, 2007.

Tian, F., Z. Li, Z. Yuan, and G. Chen, EddyGraph: The Tracking of Mesoscale Eddy Splitting and Merging Events in the Northwest Pacific Ocean, *Remote Sensing*, *13*(17), 3435, doi:10.3390/rs13173435, 2021.

Travis, S., and B. Qiu, Seasonal Reversal of the Near-Surface Chlorophyll Response to the Presence of Mesoscale Eddies in the South Pacific Subtropical Countercurrent, *Journal of Geophysical Research: Oceans*, *125*(3), e2019JC015,752, doi:10.1029/2019JC015752, 2020.

Treillou, S., P. Marchesiello, and C. M. Baker, Correction of Coherent Interference in Wave-Resolving Nearshore Models and Validation with Experimental Data, *Ocean Modelling*, *189*, 2024.

Wei, G., J. T. Kirby, and A. Sinha, Generation of waves in Boussinesq models using a source function method, *Coastal Engineering*, *36*(4), 271–299, doi:10.1016/S0378-3839(99)00009-5, 1999.

Wei, Z., R. A. Dalrymple, M. Xu, R. Garnier, and M. Derakhti, Short-crested waves in the surf zone, *Journal of Geophysical Research: Oceans*, *122*(5), 4143–4162, doi:10.1002/2016JC012485, publisher: Blackwell Publishing Ltd, 2017.

Wekerle, C., T. Hattermann, Q. Wang, L. Crews, W.-J. Von Appen, and S. Danilov, Properties and dynamics of mesoscale eddies in Fram Strait from a comparison between two high-resolution ocean–sea ice models, *Ocean Science*, *16*(5), 1225–1246, doi:10.5194/os-16-1225-2020, 2020.

Wu, G. P. K., and K. C. C. Chan, Clustering driving trip trajectory data based on pattern discovery techniques, in *2018 IEEE 3rd International Conference on Big Data Analysis (ICBDA)*, pp. 453–457, IEEE, Shanghai, doi:10.1109/ICBDA.2018.8367726, 2018.

Zheng, Y., Trajectory Data Mining: An Overview, *ACM Transactions on Intelligent Systems and Technology*, *6*(3), 1–41, doi:10.1145/2743025, 2015.

Özkan Haller, H. T., and J. T. Kirby, Nonlinear evolution of shear instabilities of the longshore current: A comparison of observations and computations, *Journal of Geophysical Research: Oceans*, *104*(C11), 25,953–25,984, doi:10.1029/1999JC900104, 1999.